Instituut voor
Kern- en Stralingsfysica
Departement Natuurkunde
en Sterrenkunde
Faculteit Wetenschappen

β-decay study of the halo nuclei ^{6}He, ^{11}Be and ^{11}Li

Jeroen BÜSCHER

Examination committee:
Prof. Dr. Christoffel Waelkens[1], president
Prof. Dr. Piet Van Duppen[2], promotor
Prof. Dr. Mark Huyse[2], promotor
Prof. Dr. Gerda Neyens[2]
Prof. Dr. Riccardo Raabe[2]
Prof. Dr. Karsten Riisager[3]
Prof. Dr. Nathal Severijns[2]

Dissertation presented in partial fulfillment of the requirements for the degree of Doctor in Science

[1] Instituut voor Sterrenkunde, K.U. Leuven, Celestijnenlaan 200D, B-3001 Leuven, Belgium
[2] Instituut voor Kern- en Stralingsfysica, K.U. Leuven, Celestijnenlaan 200D, B-3001 Leuven, Belgium
[3] Institut for Fysik og Astronomi, Århus University, Ny Munkegade 120, Bygning 1520, DK-8000 Århus C

September 2010

ISBN number 978-90-8649-357-9
D/2010/10.705/50

Nature uses only the longest threads to weave her patterns, so each small piece of her fabric reveals the organization of the entire tapestry.

Richard P. Feynman

Acknowledgements

Het is een beetje vreemd. Deze eerste pagina van 'het boekje' werd laatst geschreven, nagelezen en toegevoegd. Maar het klopt, want de mensen die ik hier wil bedanken, stonden steeds met helpende hand op mijn doctoraatspad of moedigden mij vanaf de zijlijn enthousiast aan. Zonder hen was de eindstreep enkel een witte meet, geen beschreven en gekoesterd avontuur.

Mijn eerste woorden van dank en waardering zijn gericht aan mijn promotoren, Piet en Mark. Bedankt om mij de mogelijkheid te geven mezelf te verdiepen in de rijke, fascinerende wereld die kernfysica onmiskenbaar is. Jullie 'open deur' weerspiegelde de voortdurende bereidheid om mij te gidsen onderweg, met jullie kennis en brede interesse als inspirerende stafkaart.

Riccardo, was je nu fysiek aan- of afwezig, steeds kon ik rekenen op jouw deskundige bijstand. Niets was je ooit teveel. Je hebt het pad en de obstakels daarop verlicht, zowel letterlijk als figuurlijk. Bedankt voor de vrijheid om mezelf te ontwikkelen en alle toffe gesprekken over de meest uiteenlopende onderwerpen.

I would also like to thank the members of the jury, Prof. Dr. Gerda Neyens, Prof. Dr. Karsten Riisager, Prof. Dr. Nathal Severijns and Prof. Dr. Christoffel Waelkens, for carefully reading the first version of the manuscript and the enlightening discussion during the preliminary thesis defense.

For more than four years I had the privilege of being a member of the fantastic and lively Nuclear Spectroscopy group. Many thanks to all its former and present members: Deyan, Iain, Irina, Jan (Ponsaers and Diriken), Jytte, Maria, Nick, Nikolas, Oleg, Rafael, Shelly, Tetsu, Thomas (TEC and Roger), Yuri and the two faithful lieutenants Paul and Johnny. Especially, I would like to mention Dieter and Jarno with who I enjoyed a lot of unforgettable moments, and the two special ladies, Beyan and Hilde, who I shared the office with.

Thanks to all people of different international institutes for the assistance before, during and after all experimental runs. In particular I would like to express my gratitude to the Danish group at Aarhus University under the supervision of Karsten Riisager and Hans Fynbo who, together with Oliver Kirsebom and Solveig Hyldegaard, were always very kind to answer all my mails full of questions. Performing the R-matrix analysis would have been even more tough without the skillful help of Solveig. Mange tak!

It is impossible to thank all people of our dynamic IKS group personally. This big THANK YOU is for all of you at the institute who made my life as a PhD student very pleasant and satisfactory. I carry a lot of beautiful moments with me: IKS-trips, lunches at De Moete, sandwich lunches, ping-pong battles, many heroic soccer victories , even more heroic 'Bike & Run' editions (thanks to crazy Nikie) and lovely runs during lunchtime. IKS, keep up the good spirit!

Een doctoraat in experimentele kernfysica gaat duidelijk gepaard met een intensieve training in experimentele administratieve procedure-afhandeling (het zou nog een interessante studierichting zijn). Bedankt aan de heersers over de chaos: Sally, Martine, Isabelle, Josée en Katia. Ook een dikke merci aan Luc en Bert voor alle IT-support. Graag wil ik ook een woordje van dank richten aan Willy, Dries en alle mensen van de electronica en mechanica werkplaatsen voor het realiseren van allerhande klusjes. Ook Nancy, een niet te overschatten kracht op het schip, mag zeker niet ontbreken in dit lijstje. Bedankt voor je toffe babbels, je eeuwige glimlach en mijn propere werkplek!

Ook over de provinciegrenzen in dit belgenlandje heen, in het bijzonder in Gent en Diepenbeek, zijn er een aantal toffe bendes die ik wel een dankvolle hand over de zijlijn wil toereiken. Gasten, merci!

De laatste dankbetuigingen gaan uit naar de hele (schoon)familie. Voor alle ondersteuning, belangstelling en aanmoediging. Bedankt grote broer en lieve schoonzus voor het leuke thuiskomen iedere keer.

Moederke, voor jou een dikke knuffel, en vader, voor jou een stevige aai over je bol: altijd staan jullie voor me klaar, mijn rugzak zit vol met mooie dingen die ik van jullie leer(de). En die zak is nooit te zwaar, want ik heb hem altijd bij mij.

Joke, bedankt voor je warme hart en onvoorwaardelijke steun, ... voor alles!

Jeroen
Leuven, september 2010

Abstract (English)

Nuclear structure studies allow us to get a better understanding of nature's fundamental interactions and the way matter is constructed. This PhD work focusses on the β decay of light exotic nuclei close to the neutron dripline that have a so-called halo structure.

The implantation technique, used in the present work, was especially designed for the measurement of β-delayed charged-particle emission channels. Radioactive beams are directly implanted in a very thin highly segmented silicon detector and the subsequent decay is observed in the same small detector volume. The advantages of this method over conventional detection setup systems are extensively described in this thesis. GEANT4 simulations were used in order to better understand the experimental results and extract the relevant information. The presented measurements were all performed with post-accelerated radioactive ISOL beams at different experimental facilities.

As a first physics case, the β-delayed $\alpha + d$ emission in the ^{6}He decay has been studied in a series of experiments at the CRC-UCL facility in Louvain-la-Neuve, Belgium. The absolute branching ratio $\bar{B} = (1.65 \pm 0.10) \times 10^{-6}$ for a deuteron energy $E_d \geq 350$ keV was measured with a greatly reduced uncertainty. This result requires a cancellation effect between two separate regions of the spatial integral in the Gamow-Teller matrix element. A complete theoretical description of the ^{6}He ground state wave function with a correct three-body asymptotic behavior is needed in order to reproduce the very weak transition probability and its observed energy dependence.

After implantation of a post-accelerated ^{11}Li beam the β feeding of bound ^{11}Be states as well as the ^{7}Li + α emission channels in the ^{11}Be decay were investigated during an experimental campaign at the TRIUMF facility in Vancouver, Canada. In a complementary experiment at ISOLDE-CERN in Geneva, Switzerland, ^{11}Be ions were directly implanted in the detector and the branching ratio of the β-delayed α-emission channel could be measured, $I^{abs}_{^7\mathrm{Li}+\alpha} = (3.47 \pm 0.12)\%$. This results agrees with the present literature value. A new $\frac{3}{2}^+$ state at 11.56 MeV in the ^{11}B daughter nucleus is suggested from an R-matrix analysis. In the β-delayed α emission, this states interferes with the known

state at 9.876 MeV. In the ^{11}Be decay, the relative feedings of the ^{7}Li(g.s.) + α and ^{7}Li(478 keV) + α channels were measured to be 92.0(4)% and 8.0(4)%, respectively. These results do not confirm the literature values.

The only bound excited state at 320 keV in ^{11}Be is found to be fed in the β decay of ^{11}Li with a branching ratio I_{γ}^{abs}(320 keV) = (10.6 ± 0.4)%. This value is in disagreement with the average literature value by a factor 1.4 and corresponds to a pure *p*-shell configuration of the ^{11}Li neutron halo based on shell-model calculations. However, other observations suggest a strong signature of *sd*-shell contribution. Our measurement might have suffered from a slight contamination of the ^{11}Li beam with directly produced ^{11}Be. In future experiments special attention has to be paid to this problem.

In the TRIUMF experimental campaign the branching ratio for the ^{8}Li + t channel in the ^{11}Li β decay was measured to be $2.59(27)\times10^{-4}$ and found to be stronger than the ^{9}Li + d emission channel.

The implantation technique with a thin highly pixilated detector was proven to be perfectly adequate for the measurements of weak β-delayed charged-particle emission channels that give valuable structure information. This PhD thesis adds to the knowledge of well studied halo nuclei and hands open questions that can be addressed in future experimental and theoretical work.

Abstract (Nederlands)

Kernstructuurstudies stellen ons in staat een beter begrip te krijgen van de fundamentele krachten die spelen in de natuur en van de manier waarop de materie is opgebouwd. Dit doctoraatswerk legt de klemtoon op het β verval van lichte exotische kernen, gelegen op de kernkaart vlakbij de druppellijn en gekenmerkt door een zogenaamde halo structuur.

De implantatiemethode die werd toegepast in dit werk, werd speciaal ontworpen voor de meting van vervalkanalen waarbij geladen deeltjes worden uitgezonden nadat er een β verval heeft plaatsgevonden. Radioactieve ionenbundels worden rechtstreeks geïmplanteerd in een zeer dunne, sterk gesegmenteerde silicium detector en het daaropvolgende verval wordt geobserveerd in hetzelfde kleine detectievolume. De voordelen van deze techniek ten opzichte van meer traditionele detectoropstellingen worden uitvoerig besproken in deze thesis. GEANT4 simulaties werden gebruikt om de experimentele resultaten beter te kunnen begrijpen en relevante informatie hieruit te extraheren. De metingen die worden behandeld in dit werk, werden allemaal uitgevoerd met behulp van naversnelde radioactieve ISOL bundels aan verschillende experimentele faciliteiten.

In een eerste reeks van experimenten aan het CRC-UCL in Louvain-la-Neuve, België, werd het β-vertraagde $\alpha + d$ emissiekanaal in het verval van ^{6}He bestudeerd. De absolute overgangswaarschijnlijkheid $\bar{B} = (1.65 \pm 0.10) \times 10^{-6}$ voor een deuteron energie $E_d \geq 350$ keV werd gemeten met een sterk gereduceerde onzekerheid. Theoretische berekeningen tonen aan dat teneinde dit resultaat te verklaren een uitdovingseffect tussen twee gebieden van de ruimte-integraal van het Gamow-Teller matrix element vereist is. Een volledige theoretische beschrijving van de ^{6}He grondtoestand met het correcte asymptotische drie-deeltjes gedrag is nodig om de zeer kleine overgangswaarschijnlijkheid en diens energieafhankelijkheid te reproduceren.

Tijdens een experimentele campagne aan de TRIUMF faciliteit in Vancouver, Canada, werden na de implantatie van een naversnelde ^{11}Li bundel zowel de β voeding van gebonden toestanden in ^{11}Be als het ^{7}Li + α emissiekanaal in het verval van dit laatste isotoop onderzocht. In een complementaire meting

in het ISOLDE-CERN complex in Genève, Zwitserland, werden er rechtstreeks ^{11}Be ionen in de detector geïmplanteerd en de overgangswaarschijnlijkheid voor het β-vertraagde α-emissiekanaal kon zo worden opgemeten, $I^{abs}_{^7Li+\alpha} = (3.47 \pm 0.12)\%$. Deze waarde is in overeenstemming met de huidige literatuurwaarde. Uit een R-matrix analyse van de data blijkt er een tot op heden ongekende extra $\frac{3}{2}^+$ kerntoestand in de ^{11}B dochterkern met een energie van 11.56 MeV te bestaan. Deze nieuwe toestand interfereert met de gekende toestand op 9.876 MeV bij het uitzenden van α deeltjes na het ^{11}Be β verval. De relatieve voedingen van de twee kanalen corresponderend met de emissie van ^{7}Li in zijn grondtoestand of eerste aangeslagen toestand, gelegen op 478 keV, werden gemeten op respectievelijk 92.0(4)% en 8.0(4)%. Deze resultaten komen niet overeen met de waarden in de literatuur.

De overgangswaarschijnlijkheid in het β verval van ^{11}Li naar de enige gebonden toestand met een energie van 320 keV in ^{11}Be werd eveneens bepaald, $I^{abs}_{\gamma}(320\text{ keV}) = (10.6 \pm 0.4)\%$. Deze waarde wijkt met een factor 1.4 af van een gemiddelde literatuurwaarde en komt, volgens schillenmodelberekeningen, overeen met een pure p-schil configuratie. Anderzijds wijzen andere experimentele observaties op een belangrijke contributie van de sd-schil. Onze meting kan mogelijk beïnvloed zijn door een kleine contaminatie van de ^{11}Li bundel door de rechtstreekse productie van ^{11}Be. In toekomstige metingen moet zeker aandacht worden besteed aan dit probleem.

Het ^{8}Li + t emissiekanaal in het β verval van ^{11}Li werd gemeten tijdens de hierboven vermelde experimentele campagne in TRIUMF en een waarde van $2.59(27)\times10^{-4}$ werd bepaald voor de absolute overgangswaarschijnlijkheid. Er werd vastgesteld dat dit verval sterker is dan het ^{9}Li + d emissiekanaal.

Er werd duidelijk aangetoond dat de implantatietechniek met een zeer sterk gesegmenteerde silicium detector uiterst adekwaat is voor de meting van zwakke β-vertraagde vervalkanalen waarbij geladen deeltjes worden uitgezonden en die waardevolle kernstructuur opleveren. Dit onderzoekswerk vult de kennis van goed bestudeerde halo kernen aan maar opent van de andere kant ook vragen die in de toekomst kunnen worden behandeld in experimenteel en theoretisch onderzoek.

Contents

List of Tables

List of Figures

Introduction

The different elements of the periodic table of Mendeleev, also called atoms, are the building blocks of the world we experience everyday. Essentially all mass is carried by the atomic nucleus, the tiny core of the atom, which consists of two kind of fermions: protons and neutrons. All elements are characterized by the number of protons (Z) they possess and for each element different isotopes are defined by the number of neutrons (N).

Atomic nuclei are thus quantum systems with a finite number of interacting nucleons. The most important interaction keeping the protons and neutrons together is the strong interaction but also the weak and electromagnetic interaction are at work in the nucleus. Because of this complexity the exact solution of the many-body problem is not easy to be found and only for nuclei up to mass $A = 12$ level structures and nuclear properties can be reproduced with "ab-initio" calculations. For the description of heavier nuclei various models have been developed, of which the nuclear shell model and the liquid drop model are the most famous. Most of the present-day knowledge of the structure of the atomic nucleus is based on the properties of nuclei close to the line of β stability, where the proton-to-neutron ratio is not so different to that of stable nuclei. But the extrapolation to regions with extreme proton to neutron ratios is a challenging quest and it has already been shown that in these exotic regions some changes in the conventional structure models have to be established. The study of nuclei far from β stability is therefore very interesting since new aspects of the nuclear interaction might be highlighted that will guide the evolution of the existing theoretical models and introduce exciting phenomena. In the light mass region close to the lines of particle stability large matter radii were observed about 25 years ago. These observations opened up the exciting field of nuclear halo studies.

Most of the nuclei with extreme N/Z ratios are radioactive and short lived and for many years they could only be studied in the decay of natural radioactive nuclei. The advent of radioactive ion beam facilities that can produce these exotic nuclei gave an enormous boost to the exploration of the nuclear chart. Using different experimental techniques the atomic nucleus can be studied in

various ways each focussing on specific properties that come as signatures of the underlying interactions. In this PhD work the atomic nucleus is investigated via its β decay which is a well-understood process governed by the weak interaction. Particle emission following this decay mode is an interesting channel often observed in the decay of halo nuclei and contains valuable information on their structure. The experimental setup that was used in the experiments described in this thesis is very sensitive to the often very weak β-delayed emission of charged particles. This is important in order to obtain precise values for the absolute branching ratios of these decay channels and to observe an accurate energy spectrum of the emitted particles.

This work covers the experimental aspects of the used implantation technique as well as the physical discussions on the charged-particle emission in the β decay of the famous halo nuclei ^{6}He, ^{11}Be and ^{11}Li, divided over four chapters.

- Chapter 1 introduces the region of light exotic nuclei with the emphasis on the halo feature.

- Chapter 2 presents a detailed description of the experimental technique where the radioactive nuclei are implanted in a thin segmented silicon detector and their decay is observed in the same active detection volume. It also reports on GEANT4 simulations that were performed to come to a full understanding of this detection setup. The main properties of the implantation technique are published in the international journal Nuclear Instruments and Methods, an article that is integrally included in the text.

  Paper I: β-decay studies with an implantation technique,
  J. Büscher, J. Ponsaers, R. Raabe, M Huyse, P. Van Duppen, F. Aksouh, D. Smirnov, H. O. U. Fynbo, S. Hyldegaard and C. Aa. Diget
  *Nuclear Instruments and Methods in Physics Research B **266**, 4652 (2008)*

- Chapter 3 deals with the charged-particle emission in the β decay of ^{6}He and includes a paper that was published in Physical Review C and describes the physical conclusions that were obtained in a series of experiments on this decay channel.

  Paper II: Measurement of the branching ratio of the ^{6}He β-decay channel into the $\alpha + d$ continuum,
  R. Raabe, J. Büscher, J. Ponsaers, F. Aksouh, M Huyse, O. Ivanov, S. R. Lesher, I. Mukha, D. Pauwels, M. Sawicka, D. Smirnov, I. Stefanescu, J. Van de Walle, P. Van Duppen, C. Angulo, J. Cabrera, N. de Séréville, I. Martel, A. M. Sánchez-Benítez and C. Aa. Diget
  *Physical Review C **80**, 054307 (2009)*

- Chapter 4 focusses on the ^{7}Li + α emission channels in the β decay of the one-neutron halo nucleus ^{11}Be measured in two experiments. By performing an R-matrix analysis on the decay energy spectra, states in the ^{11}B daughter nucleus can be identified and discussed. Thanks to the production and observation method applied in one of the two experiments, the feeding of bound ^{11}Be states as well as the ^{8}Li + t emission channel in the β decay of ^{11}Li can be measured. These feedings contain useful structure information on the ^{11}Li halo.

Conclusions on this scientific work can be found in the last chapter together with an outlook on future possibilities that can be explored.

Chapter 1

Light exotic nuclei

1.1 Nuclei close to the driplines

In modern nuclear physics the study of nuclear matter far off stability has received much attention with respect to the nuclear structure in a large mass range. The limits of the nuclear landscape are set by the driplines that define the regions where protons or neutrons can no longer be kept in the nucleus but literally drip out of it. Close to the driplines, in exotic nuclei with extreme proton to neutron ratios, some interesting features might set in compared to nuclei closer to the line of β stability. New magic numbers replacing the normal shell closures near the valley of stability have been observed together with other phenomena as strong configuration mixing, nuclear deformation, shape coexistence, β-delayed particle emission and even particle radioactivity. This was only possible thanks to the availability of exotic beams at highly evolved radioactive ion beam (RIB) facilities and the progress that has been made on specific experimental detection systems. These exciting experimental results have triggered theory groups, a process that resulted finally in a lively symbiosis of experiment and theory in the field of nuclear physics. In the next sections, firstly a short overview is given on the production of exotic nuclei, followed by the introduction of a remarkable feature that is encountered in the region of light exotic nuclei: the nuclear halo.

1.2 Production mechanisms for light exotic nuclei

There are two major problems to overcome when producing exotic nuclei at the driplines. First, they are normally produced in very small quantities together

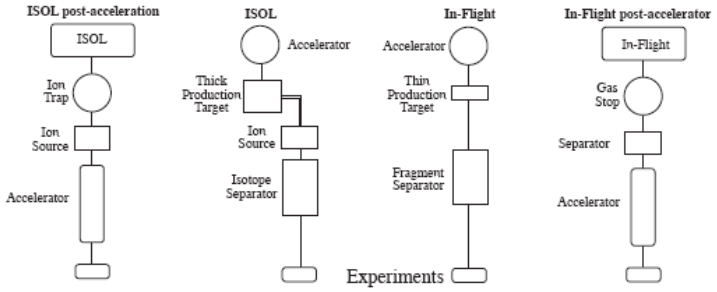

Figure 1.1: Presentation of the ISOL and IF methods used for the production of radioactive ion beams. Figure taken from [1].

with a vast amount of other, less exotic nuclei. In addition, the half lives are typically very short, in the order of ms, so any delay between production and experiment should be kept minimal. The two main production techniques of nuclei far off the line of β stability are the 'In-Flight' (IF) and the Isotope Separation On Line (ISOL) method, both schematically presented in Figure 1.1.

The IF production technique [2] makes use of an intermediate energy to relativistic heavy ion beam which impinges on a thin primary production target. The reaction products are transported to the experimental setup after mass, charge and momentum selection in a fragment separator. The ISOL technique relies on the availability of the radioactive species produced in a thick target with primary beams of protons or heavy ions from a primary accelerator or by neutrons from a reactor or a neutron converter. The reaction products are thermalized in a catcher and ionized in an ion source. After being extracted from the ion source the isotopes are mass analyzed by the isotope separator.

In both production methods, the exotic beam can be fed into a post-accelerator. This was pioneered for ISOL beams at the Centre de Recherches du Cyclotron (CRC, Louvain-la-Neuve, Belgium) [3]. The β-decay studies on ^{6}He, ^{11}Li and ^{11}Be, presented in separate chapters in this work, were performed with post-accelerated ISOL beams at the CRC (^{6}He), TRIUMF (^{11}Li, Vancouver, Canada) and ISOLDE (^{11}Be, CERN, Geneva, Switzerland). The energetic primary beams of protons were delivered by a cyclotron (CRC, TRIUMF) and a synchrotron (ISOLDE).

1.3 Halo nuclei

When approaching the driplines, the separation energy of the last nucleon or pair of nucleons decreases gradually and the bound nuclear states come close to the continuum. The combination of the short range of the nuclear force and the low separation energy of the valence nucleons results, in some cases, in considerable tunnelling into the classically forbidden region and a more or less pronounced halo may be formed. As a result the spatial structure of the valence nucleons is very different from the rest of the system and the valence and the core subsystems are to a large extent separable. Therefore, halo nuclei may be viewed as an inert core surrounded by a low-density halo of one or more valence nucleons and are hence often described in few-body or cluster models [4, 5]. Most established halo states are situated at or around the neutron dripline. On the neutron-deficient side of the nuclear chart the Coulomb barrier sets a limit on proton halos. This can be seen in the overview of the light nuclei presented in Figure 1.2.

There is no fixed definition for a halo state but generally the term is used when the so-called halo nucleon(s) spend(s) about 50% of the time outside the range of the core potential and thus in the classically forbidden region. The necessary conditions for the formation of a halo have been investigated [6–8] and it was found that besides the small binding energy of the valence particle(s), only states with small relative angular momentum may form halo states. If only one valence nucleon is surrounding the core, the two-body halo can only occur with the nucleon in s- or p-states. In three body halo systems the relative motion of the core and the two surrounding neutrons is often defined in terms of hyperspherical coordinates where the role of the classical two-body orbital angular momentum, l, is replaced by the hypermomentum, K [4]. These halo systems are then restricted to states with hypermomentum $K = 0$ or 1. The same restrictions apply for proton-halo states with the addition that the Coulomb barrier suppresses halo formation in elements with $Z > 10$.

The first direct evidence of the spatial extension of halo states was found in a series of experiments performed by Tanihata et al. [9, 10] where they extracted rms radii for He and Li isotopes from the interaction cross-section in transmission-type experiments. The radii of the heaviest, bound He isotopes, ^{6}He and ^{8}He, were found to have a larger increase than the normal $A^{1/3}$ trend while the matter radius of ^{11}Li showed an increase of about 30% compared to its closest particle-stable neighbour ^{9}Li. These kind of experiments were continued resulting in a large database of measured interaction and reaction cross-sections for isotopes ranging from ^{3}He to ^{32}Mg [11]. Proton elastic scattering experiments in inverse kinematics, measurements of total reaction cross-sections and elastic scattering cross-sections are also performed to gain information on the size of halo nuclei. In the former type of experiments the shape of the nuclear matter distribution can also be obtained from differential

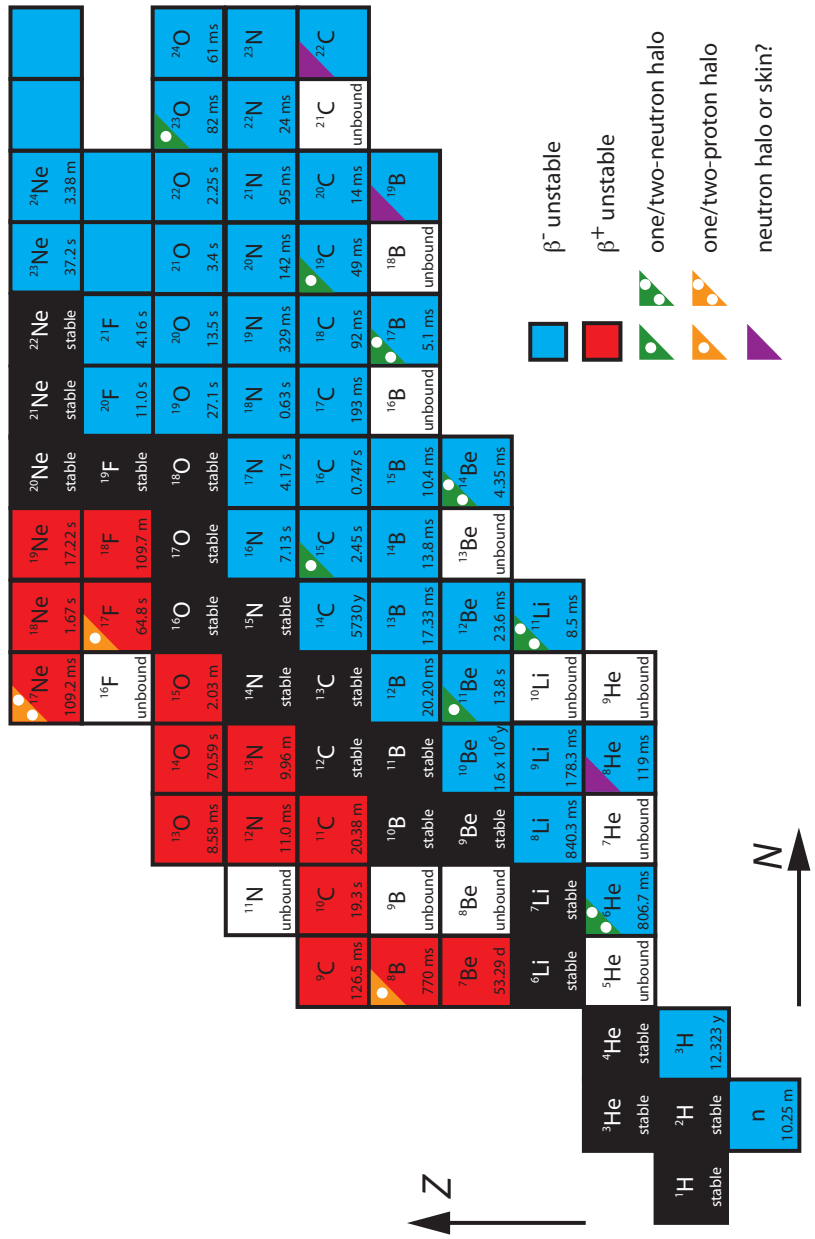

Figure 1.2: The region of light nuclei is presented in this figure with special interest for the halo feature observed at both the neutron and proton driplines.

scattering cross-sections at small momentum transfer [12]. In recent years experiments based on the technique of laser spectroscopy were dedicated to the measurements of the nuclear charge radii of ^{6,8}He [13], ^{11}Li [14] and ^{7,9,10,11}Be [15].

Other properties of halo nuclei besides their size and shape can be studied in a rich variety of experiments with radioactive beams. In the following sections 1.3.1 and 1.3.2 a short overview is given about reaction and β-decay studies, focussing on some important results for three well known halo nuclei, ^{11}Be, ^{11}Li and ^{6}He.

1.3.1 Reaction studies of halo nuclei

In the first breakup experiments narrow momentum distributions for the fragments were observed which were interpreted as a signature for the large spatial size of the halo state. This is what qualitatively can be expected from Heisenberg's uncertainty principle relating space and momentum. The quantitative relationship is however more complicated. In order to make a meaningful comparison with theoretical models the reaction mechanism, final state interactions as well as experimental conditions have to be taken into account.

In recent years, many different reaction experiments have been performed to study halo nuclei and only a glimpse is presented here for two- and three-body systems.

Two-body halos

A ^{11}Be nucleus can be described as a two-body system with one valence neutron outside the ^{10}Be core. The ground state has a spin-parity assignment $J^\pi = \frac{1}{2}^+$ and is mainly built up by a neutron in the $2s_{1/2}$ shell-model single-particle orbital coupled to the 0^+ ground state of ^{10}Be. The neutron separation energy is $S_n = 501$ keV and only one bound state is observed at 320 keV excitation energy with spin-parity $J^\pi = \frac{1}{2}^-$, corresponding to the halo neutron being in the $1p_{1/2}$ orbital. The radius of the ^{10}Be core is 2.30 fm while the rms distances between the ^{10}Be core and the valence neutrons are 6.64 fm and 5.41 fm for the ground state and the first excited state, respectively (Figure 1.3). The unnormalized external part of the s-state wave function is asymptotically $\chi(r) = \exp(-\kappa r)$, with a decay length given by $\kappa = \sqrt{2\mu S_n}/\hbar$ in terms of the reduced mass μ and the neutron separation energy S_n. The core-neutron distance is of the order of $1/\kappa$ and due to the low neutron separation energy this means that it is so large that many of the properties of ^{11}Be are determined by the tail of the wave function. The large spatial extension of the wave functions results in very large cross-sections for Coulomb and nuclear dissociation reactions and in particular in the narrow widths of the resulting breakup fragments.

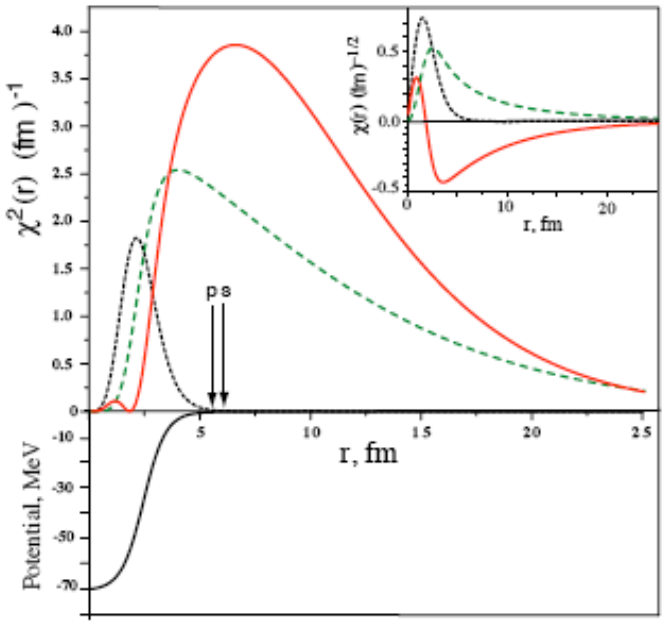

Figure 1.3: The square of the radial wave function ($\chi(r) = r\psi(r)$) single-particle components of the $2s_{1/2}$(full) and $1p_{1/2}$(dashed) levels in ^{11}Be show the halo properties of the ground state ($J^\pi = \frac{1}{2}^+$) and first excited state ($J^\pi = \frac{1}{2}^-$) at 320 keV in ^{11}Be. The dotted line presents the same quantity for the deep bound $1s_{1/2}$ orbit as comparison. The normalized wave function for the $1s_{1/2}$(dotted), $1p_{1/2}$(dashed) and $2s_{1/2}$(full) are shown in the inset. The arrows point to the rms distances between the ^{10}Be and the neutron in the ground state (s) and first excited state (p). The potential for the s waves is shown in the lower part of the figure. Figure taken from [1].

The first observed effect at the dripline that is presently understood as due to a halo structure, was the large $E1$ transition between the two only bound states of ^{11}Be, as measured in the ^{3}H(^{9}Be,pγ)^{11}Be and ^{9}Be(t,pγ)^{11}Be reactions [16]. The large $E1$ strength could be obtained on the basis of shell-model calculations when integrations in the single-particle matrix elements were made up to very large radii.

The theoretical understanding of the parity inversion of the ^{11}Be ground state required a contribution from a coupling to the first excited state 2^+ at 3.34 MeV in the ^{10}Be core. The relative weights of the components $[^{10}\mathrm{Be}(0^+) \otimes 2\mathrm{s}_{1/2}]_{1/2^+}$ and $[^{10}\mathrm{Be}(2^+) \otimes 1\mathrm{d}_{5/2}]_{1/2^+}$ were studied in a series of experiments. The ^{10}Be nuclei were studied in the reaction p(^{11}Be,^{10}Be)d in [17, 18] and in the reaction ^{9}Be(^{11}Be,^{10}Be+γ)X [19] together with γ-transitions in ^{10}Be. These measurements gave a contribution of 16-18% for the core excitation component in the ^{11}Be ground state wave function. This result was later confirmed by the measurement of the magnetic moment $\mu(^{11}\mathrm{Be})$ = -1.6816(8) μ_N [20].

From the observation of large interaction [11] and one-neutron removal cross-sections and narrow widths of the momentum distributions of the breakup fragments ^{14}C, ^{18}C and ^{22}O the isotopes ^{15}C (e.g. [21]), ^{19}C (e.g. [22]) and ^{23}O (e.g. [23]), respectively, were all identified as two-body halo systems.

Three-body halos

Two-neutron halo systems have received a lot of attention in the past due to their Borromean character [4] where the three-body system is bound but all two-body subsystems are unbound. The most studied nuclei of this type are ^{6}He, ^{11}Li and ^{14}Be. The ^{6}He nucleus has a very simple structure from the theoretical point of view. The ground state wave function has been described either as a di-neutron coupled to the α core or two neutrons on either side of the α in a cigar-like configuration [4].

The ground state structure of ^{11}Li has been the subject of much discussion. Early theoretical calculations [25] showed that an admixture of approximately equal contributions of $(2\mathrm{s}_{1/2})^2$ and $(0\mathrm{p}_{1/2})^2$ components gave the best fit to the experimentally measured narrow momentum distribution of ^{9}Li recoils after breakup of ^{11}Li [26, 27]. The relative contributions of s- and p-components were determined in a one-neutron knockout experiment where the recoil momentum $\mathbf{p}(^{10}\mathrm{Li}) = \mathbf{p}(^{9}\mathrm{Li} + \mathrm{n})$ was measured in a complete kinematics experiment [24]. The transverse component p_x is presented in Figure 1.4 from which was concluded that the ^{11}Li ground state contains a 45±10% $(2\mathrm{s}_{1/2})^2$ component.

The heaviest bound beryllium isotope ^{14}Be was identified as a halo nucleus based on radii deduced in measurements of interaction and reaction cross-sections (e.g. [28]) and the rms radius has been deduced as 3.20(30) fm [29].

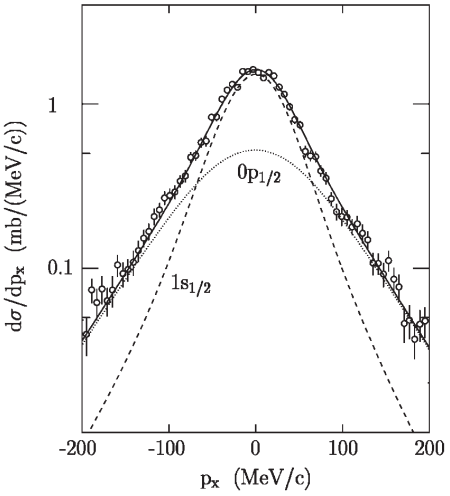

Figure 1.4: Transverse momentum distribution of the ^{10}Li fragment as observed in a ^{11}Li one-neutron knockout experiment [24].

1.3.2 β-decay studies of halo nuclei

Many properties of halo nuclei have been collected in reaction studies as explained in the previous section. The results of these experiments however often depend on the model that is used to describe the reaction process. The β decay on the other hand is a well-understood and very specific process where the measured quantities are model-independent. The energy that is available in a β-decay transition is equal to the energy difference between the initial and final states. For β^- ($Z \rightarrow Z+1$, $N \rightarrow N-1$) and β^+ ($Z \rightarrow Z-1$, $N \rightarrow N+1$) decay the maximum energy release in the process is defined as the $Q_{\beta^{-/+}}$-value and given by the following equations:

$$\begin{aligned} Q_{\beta^-} &= [m_N(^AZ) - m_N(^A(Z+1)) - m_e]c^2 \\ &= [m(^AZ) - m(^A(Z+1))]c^2 \qquad (1.1) \\ Q_{\beta^+} &= [m(^AZ) - m(^A(Z-1)) - 2m_e]c^2, \qquad (1.2) \end{aligned}$$

where $m_N(^AZ)$ indicate nuclear masses and $m(^AZ)$ neutral atomic masses and m_e corresponds to the mass of the electron/positron that is emitted in the β^-/β^+ decay together with an antineutrino/neutrino. At the driplines β decays will typically involve large Q_β-values and low particle separation energies in the daughter nuclei, see Figure 1.5. This will give rise to a rich variety of different β-delayed particle emission processes. For instance one or more neutrons can

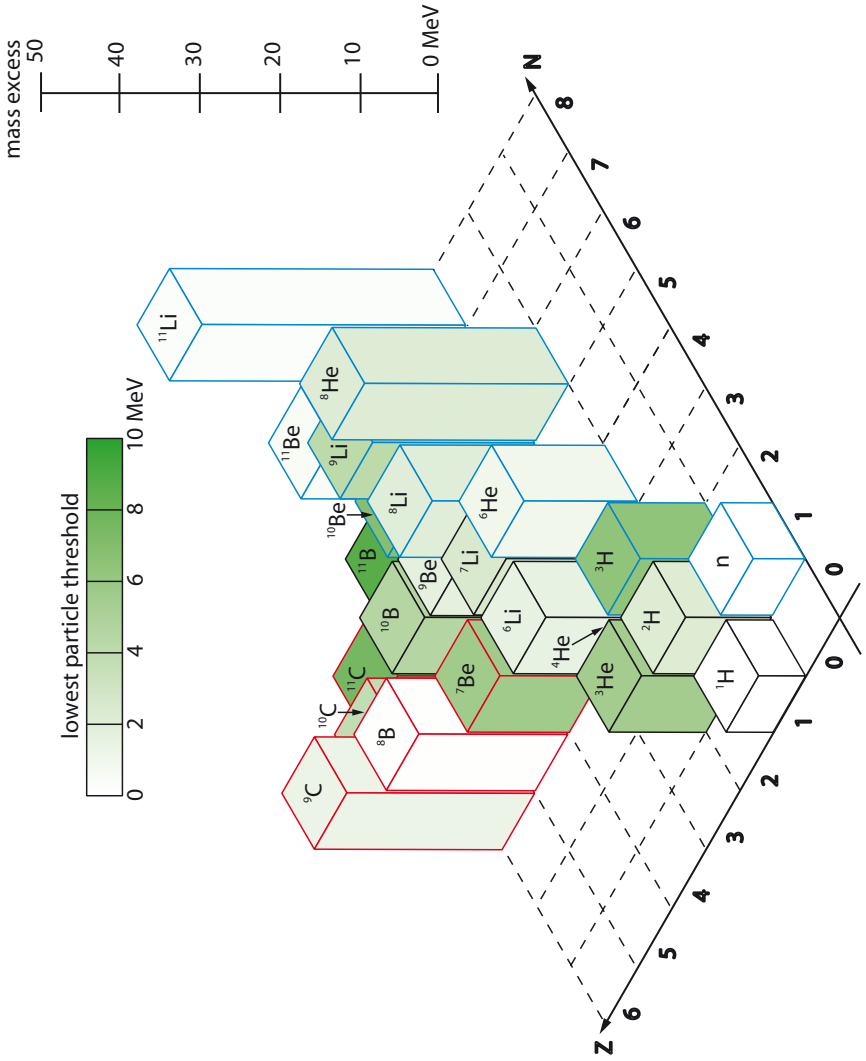

Figure 1.5: Region of bound light nuclei with mass $A < 11$. The height of the bars corresponds to the mass excess expressed in MeV whereas the color code represents the lowest particle (n,p,2n,d,α) threshold also expressed in MeV.

Table 1.1: Parameters of equation 1.3 for the nucleus ${}^{A}Z$ in β^--delayed particle emission

X	c(keV)	S
β^-p	782	S_n
β^-d	3007	S_{2n}
β^-t	9264	S_{3n}
$\beta^-\alpha$	29860	S_{4n} + $Q_\beta({}^{A-4}(Z\text{-}1))$

be emitted by the daughter nucleus if the state that is β fed is lying above the corresponding neutron(s) separation energy threshold. These decay channels have been observed extensively in the past, e.g. [30]. More exotic decay modes are the β-delayed charged-particle emission channels. The Q-value for such processes has been generalized in [31] in the following form:

$$Q_X = c - S, \tag{1.3}$$

where the constants c (equal to the mass difference between the multiple neutron system and the corresponding charged particle) and separation energies S are given in Table 1.1 for the different particle emission channels (X) following β^- decay. In this table all separation energies refer to the mother nucleus ${}^{A}Z$ and for delayed α emission a Q-value for the final nucleus enters. Since S_{2n} exceeds in most nuclei the c-parameter of 3007 keV for β-delayed deuteron emission, this decay mode only occurs in specific nuclei with low two-neutron separation energies. The Borromean nuclei mentioned above, ^{6}He, ^{11}Li and ^{14}Be all give a positive Q-value for this decay channel. This specific decay channel contains rather direct information on the halo structure of these nuclei because the decay might proceed directly into continuum states where the decay matrix element will contain a spatial integral of the initial state. This subject will be discussed for the β decay of ^{6}He in Chapter 3 and Paper II therein.

The nuclear halo structure can have a direct influence on the β decay since its large spatial extension reduces the overlap with the final state in the daughter nucleus. This can be seen in specific well-understood transitions or as a general reduction of β strength. A second effect of the halo structure is that due to its spatial configuration, the halo particle(s) and the core might β decay more or less independently from each other. This is expressed in the following equation [32], with O_β the β-decay operator, and in Figure 1.6 :

$$\begin{aligned} O_\beta|\text{halo state}\rangle &= O_\beta(|\text{core}\rangle|\text{halo}\rangle) \\ &= (O_\beta|\text{core}\rangle)|\text{halo}\rangle + |\text{core}\rangle(O_\beta|\text{halo}\rangle). \end{aligned} \tag{1.4}$$

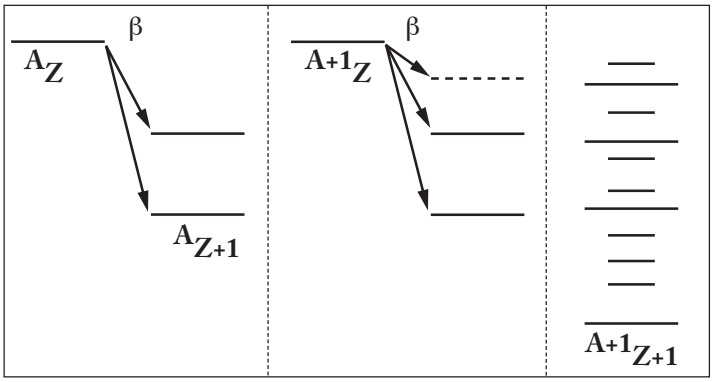

Figure 1.6: Schematic model of the β decay of a one-neutron halo according to equation 1.4. Ideally the decay of the core (left pane) and the halo contribute separately (solid and dashed lines, respectively, in the middle pane). The true eigenstates in the daughter nucleus might differ somewhat (right pane). The shorter lines in the right pane represent excited states that are not populated in the β decay.

Both terms in equation 1.4 are needed to have the correct isospin in the final state. This splitting into two parts is not strictly true because in most cases some mixing with other states in the final nucleus is very likely (see Figure 1.6), but it is possible to find transitions where this equation is a good approximation. The similar decay patterns of ^{11}Li and its core ^{9}Li, with large reduced transition probabilities to high-lying daughter states, and the ones from ^{14}Be and ^{12}Be fit well into the factorization assumption of equation 1.4 [32]. In Chapter 4 this hypothesis will be tested in the β decay of the one-neutron halo nucleus ^{11}Be.

Chapter 2

Experimental method: A calorimetric measurement after implantation

The charged-particle emission in the β decay of exotic nuclei can be studied using different methods. A technique should be applied that is properly chosen to tackle the physical questions related to the decay itself as well as the present experimental conditions. The large Q_β-values that characterise the exotic nuclei allow for many decay modes to occur. For example in the complex β decay of ^{11}Li the large mass difference between ^{11}Li and its daughter nucleus after β decay ^{11}Be (Q_β = 20.551(1) MeV [33, 34]) implies that many decay channels to bound and unbound states in ^{11}Be are open. Emission of β-delayed one [35], two [36], and three neutrons [30], α particles and ^{6}He [37], tritons [38], and deuterons [39] has been observed. These channels are often very weak and in order to obtain their precise β-decay branching ratios, the experimental setup has to be designed in a way such that the different decay modes can be clearly distinguished from each other. Moreover the presence of signals from β feeding to bound and unbound daughter states has to be dealt with. The β-decay channels towards bound states are usually orders of magnitude more intense and are characterised by large endpoint energies of the β spectrum. These contributions completely overwhelm the particle break-up channel events in the measured experimental spectra if not properly dealt with.

In most past measurements of β-delayed particle emission low-energy (typically 60 keV) beams produced with the isotope separator on-line (ISOL) method were implanted in a C-foil that was surrounded by silicon detectors and/or gas counters [40–42]. Several experimental difficulties are inherent to this method. First of all, the emitted charged particles have to leave the implantation foil

hereby losing part of their energy which remains undetected. Before entering the active volume of the detectors a dead layer has to be passed which gives an additional energy loss. This fact complicates the energy calibration of the detectors when external sources are used, distorts the energy spectra of the emitted ions and affects the minimum threshold energy for the detection of the charged particles. An accurate normalization of the different decay modes is also required to derive absolute branching ratios. This is related to the possibility to precisely determine the number of implanted radioactive ions and emitted particles. The detection efficiency for these mother nuclei and the charged particles emitted in their β decay is a crucial factor in this calculation. When using the implantation foil with surrounding detectors these factors are difficult to calculate with reasonable accuracy primarily because of geometrical effects or poorly known alternative decay branches that can be used for normalization. The main advantages of this activity-deposition method are the possibility to identify the emitted particles and apply angular correlations.

In Paper I, attached at the end of this Chapter, a method is presented for the detection of charged particles emitted in the β decay of exotic nuclei. Energetic and pure beams, produced with the in-flight method or ISOL method followed by post-acceleration, can be directly implanted in a very thin double-sided silicon strip detector (DSSSD). The number of implanted ions can be precisely counted which enables a good normalization of the possible decay channels. Time and position correlations between the implantation and the subsequent decay can be used in a small detection volume of the highly pixelated detector to identify different decay channels [43–45]. The method is based on earlier experiments dealing with α decay [46] or nuclear properties near the proton dripline [47], where reaction products are implanted in DSSSDs. The high degree of segmentation of the detector ensured an efficient correlation between the implantation and the subsequent decay occuring in the same pixel. This characteristic decay could be used to tag in-beam γ-ray transitions detected around the target (recoil decay tagging, RDT). This method was shown to be highly insensitive to β particles [47, 48].

The high degree of pixelation, and consequently the small active volume of the detector, and the precise energy of the radioactive ion beam are the key features of the method. This is illustrated in Figure 2.1 where two radioactive ions are implanted (I) around the middle plane of the detector by appropiate tuning of the beam energy. In one pixel (PIXEL 1), defined by two strips on opposite sides of the detector, a first β decay (D1) occurs at the position of implantation. In this decay two stable particles are emitted (indicated by the green and red arrows) which are confined in the same pixel. In the other pixel (PIXEL 2) one of the particles emitted (orange and purple arrows) in the first β decay (D1) is β unstable. The particles are again confined in the same pixel of the original implantation (I) and thus the second decay (D2) also takes place in

this small volume. The particles emitted in this last decay (magenta and brown arrows) are in this figures assumed to be stable. All the β particles emitted in the decays can easily be scattered in different directions. Therefore they are usually not confined in the same pixel where the decay occured and they can either travel long distances in the detector or escape from it. In general the β particles lose too little energy to give a signal above the detection threshold; however this energy is added up to the energy of the charged particle emitted after the β decay. Taking all these things into account the main advantages of the method are a good precision of the overall normalization and a reduction of the background due to β radiation.

The general properties of the implantation technique that was applied in the experiments described in this work are explained in [43]. In the following section 2.1 detailed information is given on the specific DSSSD and the electronic setups including the data acquistions systems that were used. Paper I reports about developments that have been made regarding the measurement of very weak β-delayed charged-particle emission channels. The suppression of pure β signals, one of the main characteristics of the implantation technique, is further discussed in section 2.3. In order to come to a full understanding of the detection technique simulations were performed of which the results are presented in section 2.4.

2.1 The double-sided silicon strip detector (DSSSD)

The double-sided silicon strip detector that was used for the measurements of β-delayed charged-particle emission channels discussed in Chapters 3 and 4 was designed and manufactured by Micron Semiconductor Ltd. [49] to specifications given by the Nuclear Physics Group from the University of Edinburgh [48]. The active area of the detector is 16×16 mm^2 and the thickness of the silicon wafer is 78 μm. The thickness was kept as low as possible to minimize the detector's efficiency for β particles. The front side contains 48 $p+n$ junction strips while the back side has 48 $n+n$ ohmic strips perpendicular to the ones on the other face. The strip pitch is 335 μm while the strip width is 300 μm. A bias voltage of 30 V is applied for full depletion of the silicon. The total leakage current has typical values of 0.7-0.8 μA and attention is being paid during experiments that this current is not increasing too much. To make the system more stable, a cooling system was designed recently to keep the detector at a constant temperature. A closed circuit containing a Low Odor Base Solvent (LOBS) makes thermal contact with the detector holder. The system has only been tested at a temperature of 5°C keeping the fluctuations in the leakage current within 10%.

The detector is mounted in a vacuum chamber on an insulating frame, see Figure 2.2. A 5 mm thick copper collimator with a square that has the same

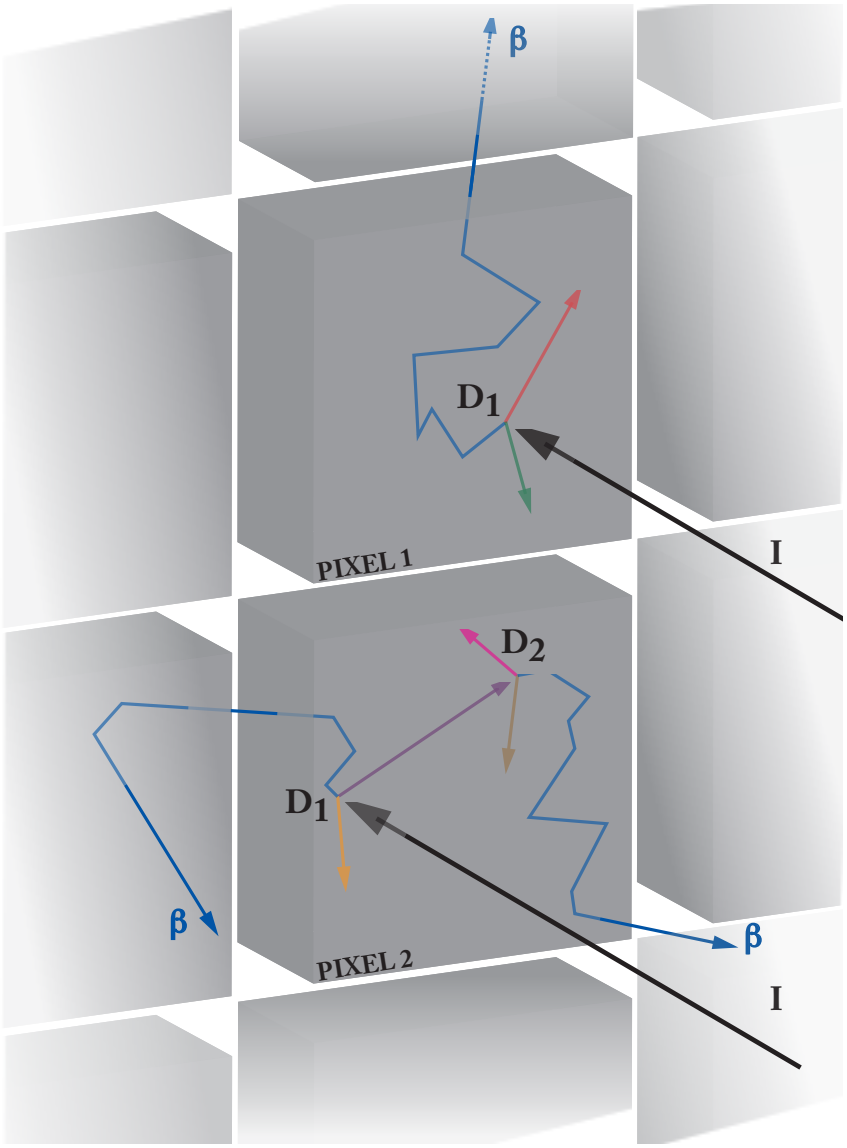

Figure 2.1: Illustration of implantation and subsequent decays in the DSSSD. The pixels, intersections of two strips lying on opposite sides of the detector, are separated by empty regions corresponding to the interstrip regions. The width of these latter regions is exaggerated in the figure to give a better overview. More info is given in the text.

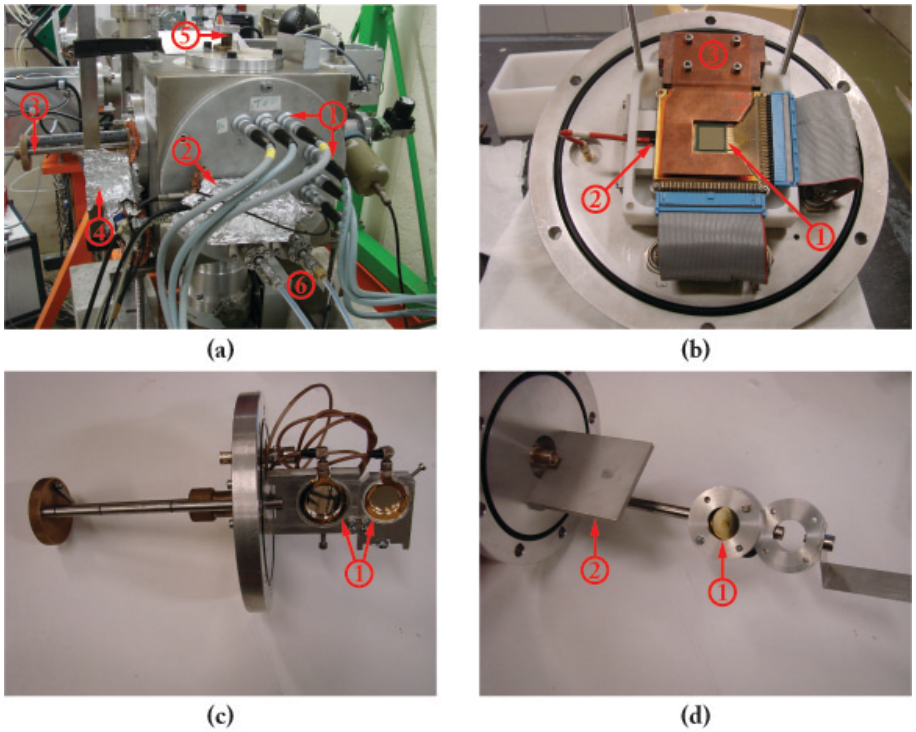

Figure 2.2: (a)Vacuum chamber ① DSSSD-preamplifier cables ② back detector ('veto') preamplifier ③ Auxiliary detectors ladder + ④ preamplifier ⑤ Calibration source ladder ⑥ Cooling circuit (b)① DSSSD ② back detector ('veto', not visible) ③ Cooling system (c) Auxiliary detector ladder ① Auxiliary detectors (d) Calibration source ladder ① Calibration source ② Metal plate behind which the sources can be hidden.

size of the DSSSD is installed in front of it. 5 mm behind the DSSSD there is place to install another small detector. Usually a circular Si surface barrier detector is placed here to 'veto' events in the DSSSD that are in coincidence with events recorded in this auxiliary detector. This is done because such events correspond to either beam particles that are not stopped in the DSSSD or decay events that escape from it, not leaving the full decay energy in the active volume. Since this extra back detector was not used in the experiments described in this work, it will not be further discussed.

Calibration sources can be mounted in the vacuum chamber on a ladder attached to one of the flanges, see Figure 2.2. Several positions on this ladder can be placed in front of the detector in order to use more than one source. The main advantage of this system is that the whole system can stay fully operational during calibration runs which are thus performed in the same conditions as the actual β-decay measurement. By making several calibration runs during the experimental campaign, the stability of the detection system can be checked. The sources are hidden behind a thick metal plate in the chamber when the radioactive ion beam is implanted and its decay is measured.

Other auxiliary detectors can also be mounted on the ladder and be placed in the beam path (Figure 2.2). Energy loss and/or time information from these detectors can be used in combination with corresponding signals from the DSSSD in order to identify the beam and possible contaminants. In the experiments described in Chapters 3 and 4 no extra detectors were used for such a beam diagnostics.

2.1.1 Electronics for data-taking and -readout

In order to make full advantage of the high segmentation of the DSSSD, the strip signals of this detector are read out separately. All strip channels are connected to the Mesytec MPR-64 preamplifier module [50]. This charge sensitive multichannel preamplifier is specially designed for single or double-sided multi-strip silicon detectors. The output signals are fed in different Mesytec STM-16 amplifiers [51]. These modules amplify and shape the signals for further information processing. The amplification factor has to be chosen in a reasonable way in order to cover the full energy range for decay and implantation events. If this is not feasible without any significant loss of resolution, i.e. if the energy range is too large, one can opt for two amplification chains, one with a lower and one with a higher gain setting. The thresholds for input signals on these modules are usually set just above the noise level. The shaper output is coupled to an Analogue-to-Digital Converter (ADC) that will digitize the energy information of the strip signal. This is done when the different ADC modules are triggered by a signal that is the logic OR of all triggers from the amplifiers, brought in phase with the Radio Frequency (RF) of the cyclotron that is used to deliver the primary beam. The logic ECL signals from the STM-16 module

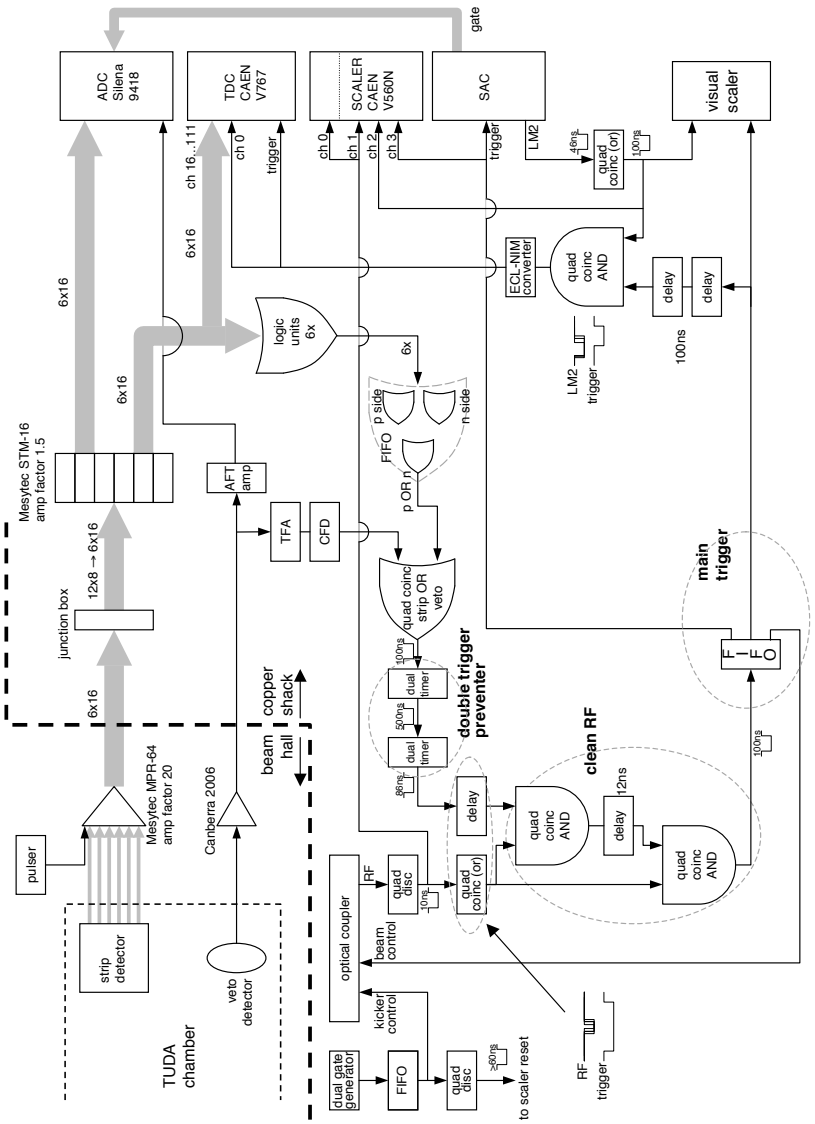

Figure 2.3: Electronics scheme that was used for the β-decay measurements of ^{8,9,11}Li and ^{11}Be.

are fed in a Time-to-Digital Converter (TDC). A detailed electronics scheme that was used for the experiment described in Chapter 4 is shown in Figure 2.3. The most important parameters for this type of β-decay experiments are the energy signals and an absolute time reference (timestamp, in Figure 2.3 generated by the cyclotron RF). If the beam is tuned in on- and off-periods (see section 2.2) we also need a channel in the scaler module that serves as a flag to indicate the position of the event in the implantation-decay cycle. Several data acquisition systems can be used for the read out of the data. For example the Multi-Branch System (MBS), introduced in 1994 at GSI [52], and the Multi Instance Data Acquisition System (MIDAS) [53] were used in the different experiments. The obtained raw data files are converted to files that can be handled in the conventional off-line analysis programs. The analysis of the measurements presented in this work are performed with the PAW++ (Physics Analysis Workstation) CERN-package [54].

2.2 Time profile of the radioactive ion beam

In general, the β decay of the radioactive ions that are implanted in the DSSSD can have many break-up channels, with both stable and unstable daughter nuclei. If we consider the case where there is only one charged-particle emission channel, with only stable end products, the ion beam is modulated in on- and off-periods. A clean decay energy spectrum is then obtained by recording the events in the beam off period. This is illustrated in Figure 2.4 that shows the count rate of decay signals in the DSSSD as a function of time. The beam is implanted in intervals of length t_0. In between these periods the β decay can be measured in intervals of the same length t_0. In order to ensure that a pure decay spectrum is measured, a safe interval between times t_1 and t_2, indicated by the green dot-dashed lines in Figure 2.4, is usually chosen. Given the implantation rate, R, the half life of the implanted ion and the corresponding decay constant, $\lambda = \frac{ln2}{T_{1/2}}$, and the time information of the on- and off-periods, one can calculate the percentage of the total decay events that is actually measured during the beam-off intervals. This is done here for the first cycle, shown in Figure 2.4, starting at t = 0 s. The total number of decays for this cycle is easily defined as the product of the implantation rate and the length of the beam on interval (all implanted ions will decay eventually):

$$\mathrm{D_T} = Rt_0 \tag{2.1}$$

The number of observed decay events can be found by adding the contributions indicated by the green-shaded intervals in Figure 2.4. The events in the red-shaded regions, belonging to the decay of the first implantation cycle, fall in the implantation intervals of the following cycles and are thus not contributing

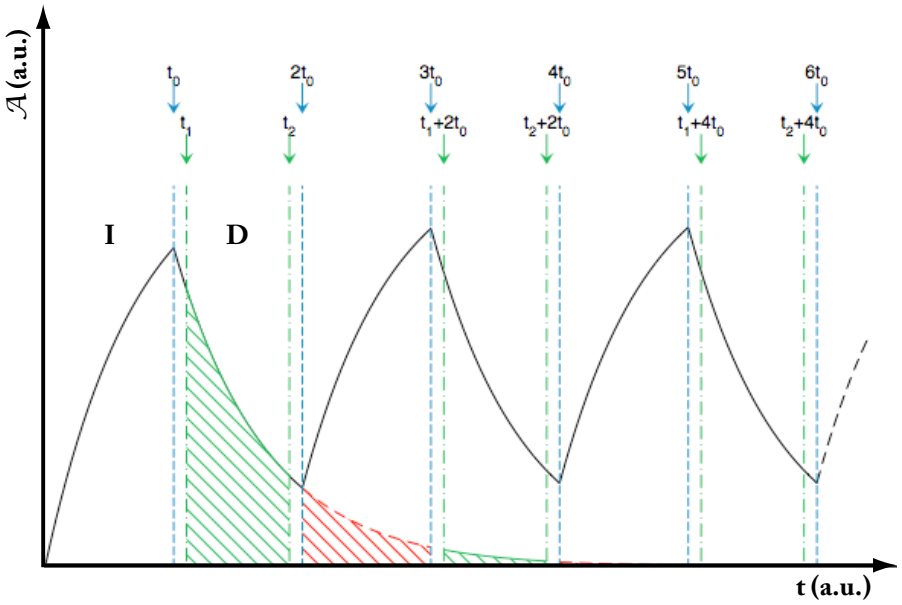

Figure 2.4: The figure shows the count rate of decay signals in the DSSSD as a function of time in a sequence of implantation (I, beam on) and decay (D, beam off) intervals. In this figure the beam-on/off periods have the same length t_0 and the decay spectrum is measured between two green dot-dashed lines. More information is given in the text.

to the measured decay spectrum. The count rate of decay signals at time t_0 is equal to $\lambda \times N(t_0) = R(1 - e^{-\lambda t_0})$. Hence, for the observed decays we get:

$$
\begin{aligned}
\mathrm{D_O} &= R(1-e^{-\lambda t_0})\Big(\int_{t_1}^{t_2} e^{-\lambda(t-t_0)}dt + \int_{t_1+2t_0}^{t_2+2t_0} e^{-\lambda(t-t_0)}dt \\
&\quad + \int_{t_1+4t_0}^{t_2+4t_0} e^{-\lambda(t-t_0)}dt + \ldots + \int_{t_1+2Nt_0}^{t_2+2Nt_0} e^{-\lambda(t-t_0}dt\Big) \qquad |N \in \mathbb{N} \\
&\cong R(e^{\lambda t_0}-1)\int_{t_1}^{t_2} e^{-\lambda t}dt \qquad\qquad |1^{st}\text{ approximation} \\
&\cong \frac{R}{\lambda}(e^{\lambda t_0}-1)(e^{-\lambda t_1}-e^{-\lambda t_2}). \qquad\qquad (2.2)
\end{aligned}
$$

The ratio of (2.2) over (2.1) is thus dependent on the decay constant of the implanted isotope and the time structure of the chosen beam-on/off intervals. When calculating absolute branching ratios of decay channels we have to correct for the fact that we do not observe all decay events using this ratio. This has been done for example in the experiments described in Chapters 3 and 4. The length of the beam-on/off period is typically about 2 or 3 times the decay half life of the implanted isotope.

If more decay channels are open, they can be identified by applying time and position correlations. In this case continuous beam implantation can be used. For example, the energy spectra and the absolute branching ratios of the weak ^{9}Li + d and ^{8}Li + t channels in the β decay of ^{11}Li could be obtained using this technique [45]. The probability density distributions as a function of time for implantations (I), mother (D_M) and daughter (D_D) decays are given by the following equations

$$P(I) = \lambda_I e^{-\lambda_I t} \tag{2.3}$$

$$P(D_M) = \lambda_M e^{-\lambda_M t} \tag{2.4}$$

$$P(D_D) = \lambda_D e^{-\lambda_D (t-t_1)} \tag{2.5}$$

when the mother nucleus is implanted at time $t = 0$ s and the first decay takes place at time $t = t_1$. λ_I is the implantation rate in a pixel. Equation 2.3 is obtained from the fact that the implantation is regarded as a Poisson process. λ_M and λ_D correspond to the decay constants of the mother and daughter nuclei, respectively. With these functions one can calculate the probability of observing the mother decay before another ion is implantated in the same pixel, $P_M = \frac{\lambda_M}{\lambda_M+\lambda_I}$ (see Paper I). The probability of observing the second decay after the first one before another implantation is also defined, $P_D = \frac{\lambda_M}{\lambda_M+\lambda_I}\frac{\lambda_D}{\lambda_D+\lambda_I}$ (see Paper I). Again, when calculating absolute branching ratios one has to correct for these probabilities. It is obvious from the formulae given above that the rate of implantation in one pixel should not be too high in order to keep these probabilities as close as possible to 1.

2.3 β-suppression factor

For the measurements of β-delayed particle emission different constraints can be placed on the events to select them for the off-line analysis. Different experimental conditions imply different noise conditions and hence different electronic threshold settings. The aim is to keep the detection threshold as low as possible because the charged-particle spectrum might contain important information at low energies. Apart from the electronic noise settings, the presence of a huge background from β particles complicates the extraction of this information. As

explained in [43] and Paper I the influence of the β particles can be largely reduced, making use of the segmentation of the DSSSD. The strips in an event that give a signal above a certain threshold defined in the off-line analysis are counted for the front and back side of the detector. If there are only two strips firing in the event, one on each side, the event is selected for further analysis. This is the so-called requirement for multiplicity one-one (*M11*) events. Since the β particles generally lose very little energy in one detector pixel, most of the time under the detection threshold, this already suppresses this β contribution a lot. By setting a maximum limit for the energy difference between the strip signals this β background is further reduced. In Paper I the β-suppression factor $\mathcal{F}(E)$ is defined as the ratio between the total emitted β particles and those detected above the energy E. It was shown that this factor is essentially independent from the end-point energy of the decay, reaching about 10^7 for signals recorded above 500 keV.

In this section more detailed information is given about the influence of the constraints that were applied to suppress the β signals. In the first place the *M11* condition that was explained above is further investigated together with the choice of the energy threshold in the off-line analysis. In order to be able to observe in the off-line analysis practically all events that occur inside the detector a very low threshold can be chosen. In the experiment where we studied the charged-particle emission in the β decay of ^{11}Be, described in Chapter 4, the noise levels in all channels (except for one) corresponding to the strips of the detector were very low and a threshold of 40 keV could be applied in the off-line analysis. For every event, all the strips which gave a signal above this value were counted and their energies were summed up for the front and the back side of the detector. The multiplicities on both sides were also stored. This is the so called open multiplicity selection *Mab*. If in the first place one is interested in the events corresponding to the emission of charged particles and a reduction of the β background, a higher threshold for the off-line analysis is more appropiate and the *M11* condition should be applied. In the study of the β decay of ^{11}Be all strips were then counted with signals above the noise level of the strip with the highest noise level. This level was situated around 80 keV. If the multiplicities on both sides of the detector were equal to 1 and both the energies were higher than an off-line analysis threshold of 200 keV, the event was accepted for further analysis. For both conditions the energy spectrum of the events can be plotted. Those spectra are presented in Figure 2.5 where the number of events are given as a function of the average value of the collected energies on both sides of the detector. The different contributions in the spectra will be explained in the next section as well as in Chapter 4. It is clear that when applying the *M11* condition the exponentially decreasing contribution at low energies corresponding to β particles ([43] and Paper I) is strongly suppressed in comparison with the open

multiplicity selection. At higher energies where the signals from the emitted charged particles are expected, the two spectra almost coincide with each other.

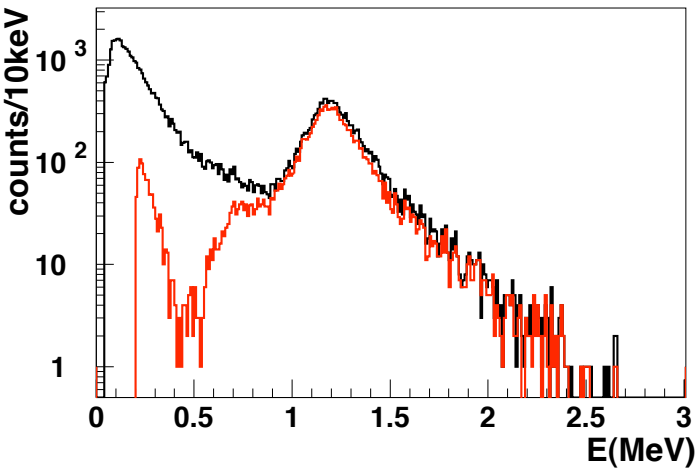

Figure 2.5: The β-decay energy spectrum of ^{11}Be is presented for different multiplicities and energy thresholds chosen for the off-line analysis. For the black spectrum the open multiplicity selection *Mab* was used with a low threshold value of 40 keV. The grey curve represents the *M11* events when a threshold of 200 keV was applied. More info is given in the text.

The different conditions for the off-line analysis threshold and the strip multiplicities were also applied in the study of the very weak (of the order of 10^{-6}) β-delayed deuteron emission channel in the decay of ^{6}He. In this experiment, described in detail in Chapter 3, the electronic thresholds were placed at a higher level than in the study of the β decay of ^{11}Be because of noise considerations. The influence of the different multiplicity conditions was checked with the same off-line analysis threshold setting at 200 keV. If the open multiplicity selection *Mab* was applied with this setting, events with different multiplicities on both detector sides were accepted for further analysis. Those events could be categorized in different groups. First of all there were the *M11* events having only one strip on each side with an energy higher than 200 keV. The *M12* and *M21* events had 2 strips on one side that fulfilled this condition and only one at the opposite side. The higher multiplicity events were put in groups called *M1n*, *Mn1* ($n > 2$) and *Mnn* ($n > 1$) following the definition for the other groups. All β-decay events are shown in an energy scatter plot in Figure 2.6. Each axis refers to the total energy signals collected on one side of the detector,

either the front or the back side. Thus if the multiplicity on one or both sides of the detector is higher than 1, the energy signals of all strips belonging to one side are added to obtain the total energy for the corresponding side. If both total energies are below 800 keV different multiplicity events are observed. The events with *M1n* or *Mn1* ($n > 1$) are however more concentrated in off-diagonal regions corresponding to a substantial energy difference between the energies collected on both sides of the detector. At higher energies mainly *M11* events are detected and they lie around the diagonal. From this observations it is clear that the β-particle contribution in the energy spectra can be further reduced by requiring a maximum energy difference between the energy of the front and the back side. In Figure 2.6 the dashed lines correspond to a maximum energy difference of 50 keV.

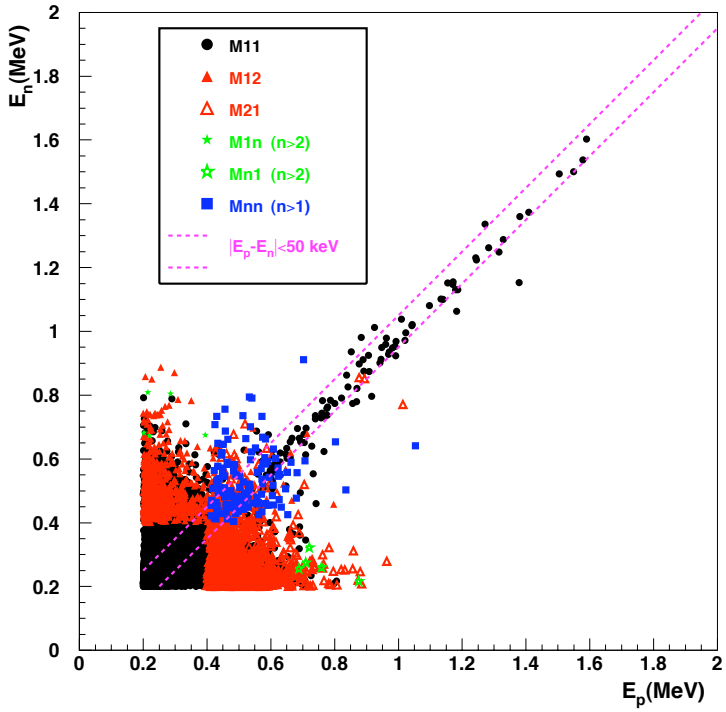

Figure 2.6: A scatter plot of the ^{6}He β-decay events with different strip multiplicities is presented for an off-line analysis threshold of 200 keV. The region between the dashed lines corresponds to a maximum energy difference of 50 keV between both sides of the detector.

To quantify the β suppression of the experimental technique the same procedure as in Paper I could be followed. The definition of the β-suppression factor $\mathcal{F}(E)$ is given above. One can also define the factor $\mathcal{F}(E, \Delta E)$ as the ratio between the total emitted β particles and those detected between E and $E + \Delta E$. Here ΔE was chosen as 50 keV. The decay energy spectra of ^{6}He and ^{11}Be were created using the different settings for the off-line analysis threshold and allowed multiplicities. For the threshold of 40 keV the events were counted in energy intervals of 50 keV in the energy range [150 keV, 500 keV]. The upper limit of 500 keV was chosen since above this energy the contribution of charged-particle emission in the β decay of ^{11}Be was not negligible whereas below this value mainly β-particle events are expected. We assumed a branch of 100% to the ^{6}Li ground state in the β decay of ^{6}He. Hence, $\mathcal{F}(E, \Delta E)$ could be calculated from the number of detected events, knowing the total number of implantated ions and the fraction of expected decays due to the observation window. Since the β branching to particle stable states in the ^{11}Be decay is not precisely known (Chapter 4) the β-suppression factor for this experiment was scaled to the factor for the ^{6}He experiment at an energy of 150 keV for this off-line analysis threshold of 40 keV. The energy range of [250 keV, 500 keV] was chosen for the threshold value of 200 keV and the scaling of the suppression factor was performed at the lower limit of 250 keV. The results for the β-suppression factor $\mathcal{F}(E, \Delta E)$ are presented in Figure 2.7 as a function of the average energy . The β-suppression factors for both experiments follow the same trend however the slope in the case of the ^{11}Be decay experiment is smaller and the suppression factor in that measurement reaches a maximum at energies around 400 keV. This can be explained by signals from emitted charged particles that are hidden under the β background. Those charged particles are counted as β particles in the last energy intervals and hence the resulting suppression factor is smaller than expected. Figure 2.7 proves that the reduction of the β background in the decay spectra is very strong when requiring a higher energy threshold for the strip energy, the *M11* condition and a maximum energy difference between the energies measured on both sides of the detector. When this last energy difference is chosen to be 50 keV together with a threshold of 200 keV, the β-suppression factor $\mathcal{F}(E, \Delta E)$ for *M11* events in the measurement of the ^{6}He β decay reaches a value of $1.8{\times}10^6$ at 500 keV.

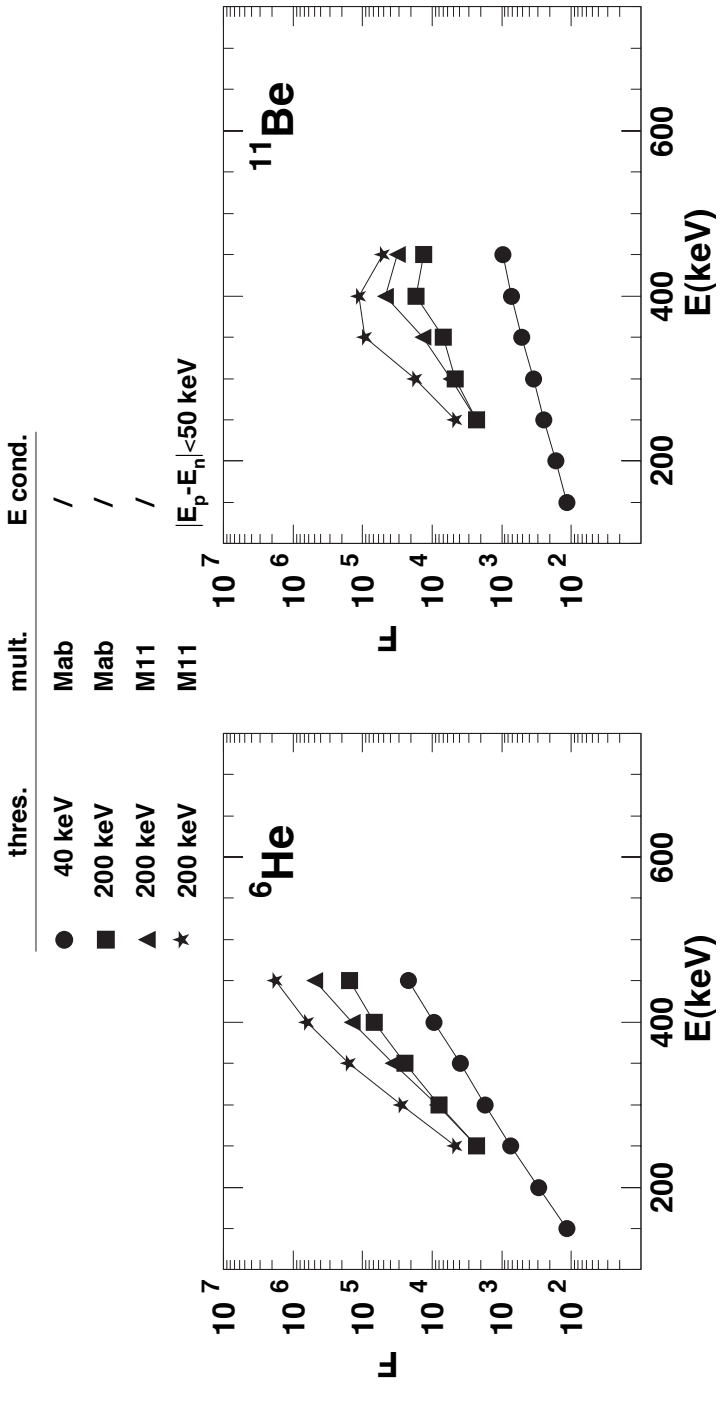

Figure 2.7: The β-suppression factors $\mathcal{F}(E, \Delta E)$ for the decay experiment of ^{6}He and ^{11}Be are presented in this figure for different off-line analysis thresholds and for different multiplicity and energy conditions.

2.4 β-summing effects - GEANT4 Monte Carlo simulation

The implantation technique was proven in the previous section to be almost insensitive to β signals if appropriate choices are made for strip multiplicities, the off-line analysis energy threshold and energy differences between the front and back side of the DSSSD. However, when heavier charged particles are detected, there is always an energy contribution of the β particle that is associated with the feeding of the unbound state that is emitting the ions. The energy loss of the β particle in a pixel is hence summed with the energy signals of the heavy ions and their total energy is recorded. This effect, the so called 'β summing', can distort the spectral shape of the β-delayed charged-particle emission channels and makes it therefore difficult to extract precise physics results related to these channels.

One generally would expect a shift towards higher energies due to this β summing. But it is important to know how large this effect actually is and if it is the same at any position in the energy spectrum. The energy loss of charged particles in materials, taking into account inelasic scattering with atomic electrons and elastic nuclear scattering, can be calculated using the Bethe-Bloch Formula [55]. This formula gives the energy loss per unit length as a function of the energy of the particle passing through the material. For electrons in silicon, this energy loss, usually given in keV/μm, is larger for lower energies than for higher ones presenting a minimum around 1.5 MeV [56]. Table 2.1 presents the energy loss [57] for β particles in silicon as a function of energy and the energy lost in the first 39 μm of the path, corresponding to half of the detector's thickness, is calculated in the last column. Regarding this properties it is very useful to investigate whether the β summing can cause an asymmetry effect on the energy spectra of the emitted charged particles.

Table 2.1: Approximate energy losses for electrons in silicon as a function of energy. In the last column the energy loss for the electron passing through 39 μm, i.e. half the detector's thickness, is calculated.

β energy (keV)	energy loss (keV/μm)	energy loss in first 39 μm (keV)
100	0.75	29.25
500	0.38	14.82
1000	0.35	13.65
1500	0.34	13.26
2000	0.35	13.65

To simulate the passage of a wide range of particles through matter the GEANT4 ([58]) toolkit was designed at CERN. It was developed in such a

way that, using the C++ object oriented programming language, the user can implement his own specific geometry and select different physical processes and particles. The physical processes rely on a wide set of physics models and cross section data and are updated and implemented by the GEANT4 team on a regular basis. For electrons the Low Energy Electromagnetic Package (LEP) was chosen in the simulation program. This includes the following physical processes:

- Multiple Scattering : average of different scattering events after a certain step size in the tracking of the electron
- Low Energy Ionization : the energy loss due to discrete ionization processes
- Low Energy Bremsstrahlung : Continuous energy losses due to Bremsstrahlung arising from scattering in the electric field of a nucleus.

The detector construction is one of the main parts in building the GEANT4 simulation program. Since we were looking for the effect of β summing in one pixel of the DSSSD, a box with dimensions 300 μm $\times$ 300 μm $\times$ 78 μm was taken as the active volume wherein the β-particle energy loss had to be calculated. A complete simulation run consists of several *events* defined by the primary particles with initial momentum and energy. The particles are *tracked* until they leave the active detector volume or its energy becomes less than a user defined threshold. This threshold is expressed in a length unit and a value of 1μm was chosen. Each particle is moved *step* by *step*, the size of which is determined by the user, by the geometry and by the physics processes. For every step, GEANT4 Monte Carlo selects a process and its effect on the particle is calculated. In our simulation code a ROOT file was created at the beginning of a run and the output data could be stored in a ROOT Tree for further analysis.

The effect of β summing was investigated in the light of the delayed particle emission in the β decay of ^{11}Be ($J^\pi = \frac{1}{2}^+$). This physics case is discussed in Chapter 4 where the measurement of ^{7}Li and α particles that are emitted from unbound states of ^{11}B, fed in the ^{11}Be decay, is highlighted. The main contribution in the charged-particle energy spectrum originates from a level around 9.88 MeV ($J^\pi = \frac{3}{2}^+$) which is known to be populated via an allowed Gamow-Teller transition. The ^{7}Li + α threshold in ^{11}B lies at 8.665 MeV whereas the Q_{β^-}-value is 11.506 MeV. More details are given in Chapter 4. From these values and conservation of momentum it is easily calculated that the maximum α and ^{7}Li energies are about 1.8 MeV and 1.0 MeV, respectively. The range for these particles in silicon are less than 6.45 μm and 2.80 μm, respectively, calculated using SRIM [59]. Those ranges are substantially smaller than the dimensions of one detector pixel. The emission of those particles was therefore

not simulated and it was hence assumed that those particles deposit all their energy in the pixel. In the first paper describing the implantation technique a similar simulation for the β-delayed deuterons and α particles emitted in the ^{6}He decay was described [43]. There it was shown that virtually all (99.94%) of the emitted charged particles were confined within one pixel. For the simulation it was also assumed that the state around 9.88 MeV only breaks up into an α particle and ^{7}Li in its ground state ($J^{\pi} = \frac{3}{2}^{-}$), so the emission of ^{7}Li in its first excited state at 478 keV was not considered. The ^{11}Be isotopes in the simulation are assumed to be uniformly implanted at a depth of 39 μm, corresponding to the middle plane of the detector.

In the simulation, the ^{11}B level at 9.88 MeV is assumed to have a Lorentzian profile which was believed to be a good first approximation for the real experimental shape. For the investigation of the β summing the width of the state was not a crucial factor but in order to reproduce more or less the experimental data, a full width at half maximum (FWHM) of 160 keV was chosen. The simulation was performed for 12000 events, approximately the statistics that was collected in the real measurement of the ^{11}Be β decay. Those events were spread in an energy range of 12 times the chosen FWHM centered around 9.88 MeV. The feeding of this state was Monte Carlo simulated taking into account the phase space factor for allowed β-decay transitions. For the latter the parametrization of [60], which is also described in Appendix A, was used. In Figure 2.8 the profile of the state is shown as a function of the summed energies for the ^{7}Li and α particle when no β-particle energy is included. One can clearly see that this spectrum peaks around 1.2 MeV, the difference between the center of the state and the ^{7}Li + α threshold in ^{11}B. Due to the energy dependence of the β-decay phase space factor the high-energy tail of the state, corresponding to low β-particle energies, is quenched in comparison with the low-energy tail.

The summed energies for the ^{7}Li and α particle (presented in Figure 2.8) immediately set the endpoint energy for the β particle (electron) and the neutrino present in the decay process. This endpoint energy together with the atomic number of the daughter nucleus, $Z = 5$ for B, defines the energy spectrum for the β particle as described in [61–63]. Thus with every event there was an associated endpoint energy resulting in such a β-energy spectrum out of which the actual β-particle energy was Monte Carlo simulated. Figure 2.9(a) shows the β-particle energy as a function of the total ^{7}Li + α energy whereas Figure 2.9(b) shows the spectrum of the selected β particles as a function of their energy. For the actual simulation the electron was given the selected β energy and it was placed on the middle plane of the detector, using a uniform distribution. This reflects one of the goals that is generally aimed for in the real experiment where the energy of the radioactive beams is tuned in such a way that it is stopped around the middle plane of the detector. The momenta

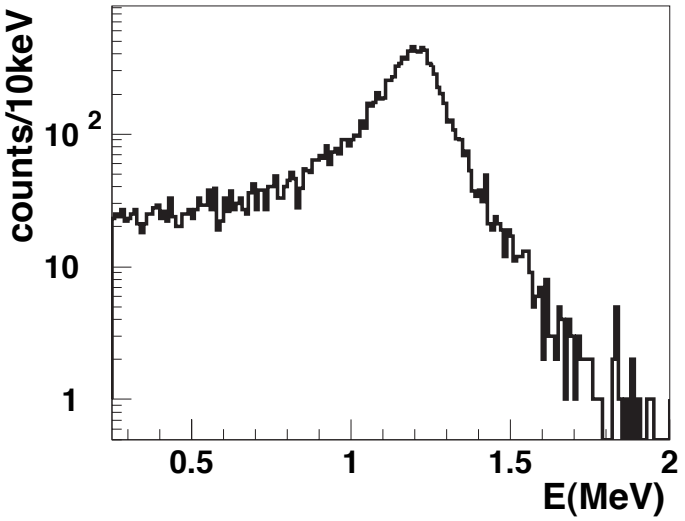

Figure 2.8: The feeding of the ^{11}B state at 9.88 MeV in the β decay of ^{11}Be is simulated and shown as a function of the emitted α and ^{7}Li energies. More info is given in the text.

of the β particles were distributed isotropically. The particle could be tracked and the energy losses in the steps along its path were sent to the data collection as long as the particle did not escape the pixel.

The β-particle energy loss spectrum is shown in Figure 2.10. This spectrum shows a clear peak around 12 keV and has an exponential tail towards higher energy losses. The presence of the peak can be explained by the fact that a uniform distribution at the middle plane of the detector was assumed for the initial β particle. Therefore, most electrons have to pass through a minimum amount of material before they can leave the pixel. Contributions of β particles originating at the edges of the active volume can be associated with the events in Figure 2.10 in the range from 0 to 5 keV. In Figure 2.11 the energy loss of the β particles is plotted as a function of the initial energy. For all the energy values the deposition of an energy around 12 keV is the main contribution. However, at low energy values, from 0 to about 200 keV, the diagonal contribution in the spectrum indicates the non-negligible probability of full energy deposition in the pixel. This effect is only present at low β-particle energies and one can expect that this might create an asymmetry effect on the spectral shape of the 9.88 MeV level since generally large energy values for the

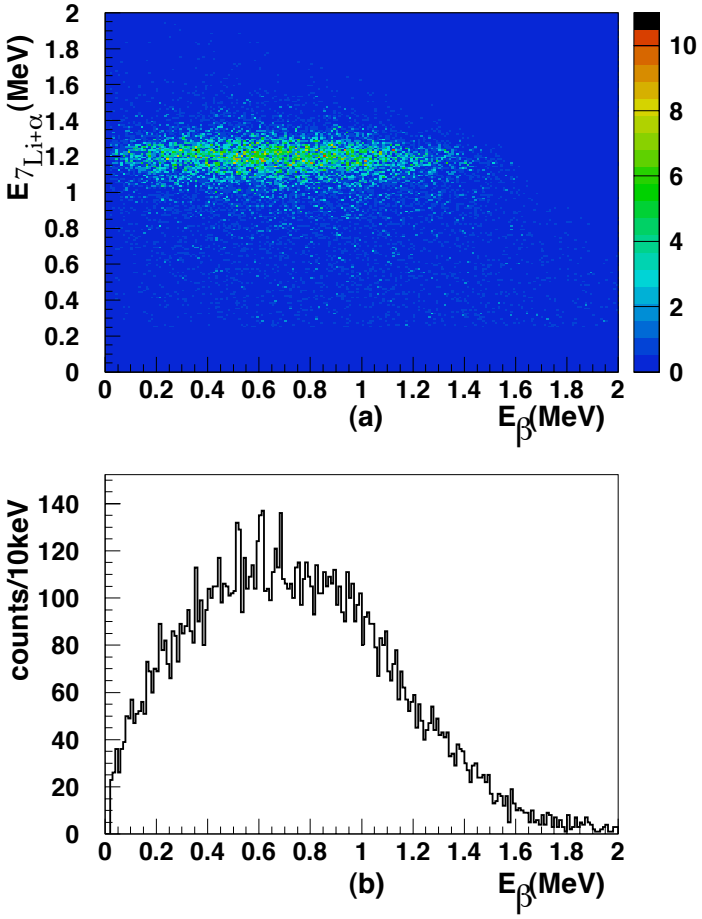

Figure 2.9: (a) This figure shows the summed energy of the emitted α and ^{7}Li particles versus the β-particle energy. (b) The number of simulated β particles are given as a function of their energy.

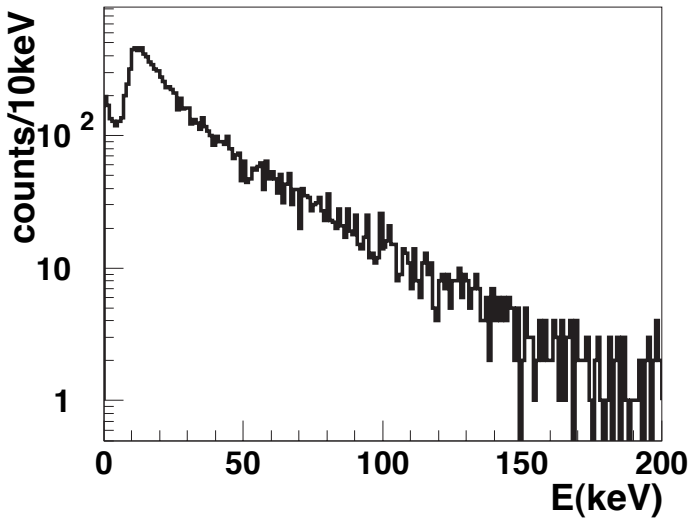

Figure 2.10: The figure shows the simulated energy deposition spectrum of the β particles in one pixel of the DSSSD.

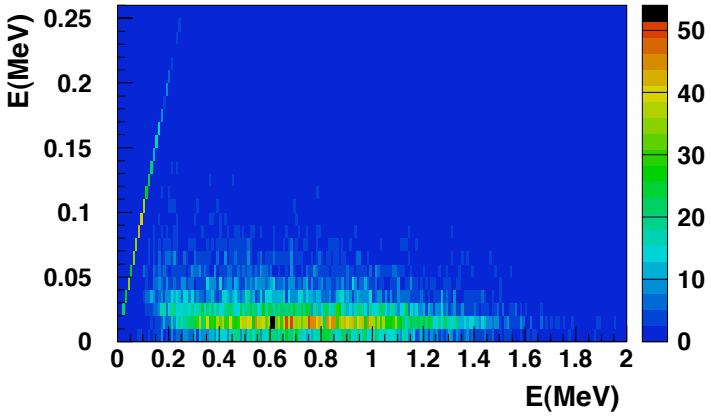

Figure 2.11: The scatter plot gives the simulated energy deposition in one pixel of the DSSSD versus the initial energy of the β particle.

emitted heavy ions correspond to low-energy β particles and vice versa. To investigate this, the energy loss was added to the initial energies of the ^{7}Li and α particles. The resulting spectrum can then be compared with the original spectrum without the β-summing effect presented in Figure 2.8. In Figure 2.12 one indeed observes a slight depletion of the height of the spectrum indicating the asymmetry effect. Still, one can conclude that the main influence of the β summing on the measurement of the emitted charged-particle energy spectrum is an overall shift with 12 keV.

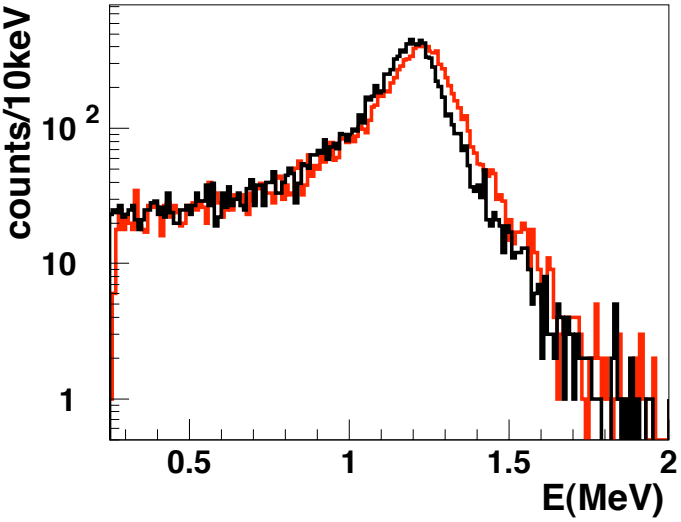

Figure 2.12: The black energy spectrum is the same as in Figure 2.8 and represent the energy of the emitted α and ^{7}Li particles. If the simulated energy deposition of the β particle is added to this spectrum, the red spectrum is obtained which corresponds to the total energy detected in one pixel of the detector.

Paper I: β-decay studies with an implantation technique

This section contains the integral text of the article that was published in *Nuclear Instruments and Methods in Physics Research B 266, 4652 (2008).* It reports on recent developments in the experimental technique of implanting radioactive nuclei directly in a highly segmented detector and the measurement of the subsequent decay in the same detector volume. Some of the characteristics in the article are explained in greater detail in the sections above.

β-decay studies with an implantation technique

J. Büscher,[1] J. Ponsaers,[1] R. Raabe,[1] M. Huyse,[1] P. Van Duppen,[1] F. Aksouh,[1,*] D. Smirnov,[1] H. O. U. Fynbo,[2] S. Hyldegaard,[2] and C. Aa. Diget[3]

[1] *Instituut voor Kern- en Stralingsfysica, K.U. Leuven, Celestijnenlaan 200D, B-3001 Leuven, Belgium*
[2] *Institut for Fysik og Astronomi, Århus Universitet, DK-8000 Århus, Denmark*
[3] *Department of Physics, University of York, Heslington, YO10 5DD, UK*

A method is presented for the detection of charged particles emitted in the β decay of exotic nuclei. Direct implantation of radioactive nuclei in a very thin double-sided silicon strip detector is now feasible thanks to the advances in the production and post-acceleration of ISOL beams. The high degree of pixilazation, and consequently the small active volume of the detector, and the precise energy of the radioactive ion beam are the key features of the method. Among the advantages of the method are a good precision of the overall normalization and a reduction of the background due to β radiation. Several developments are described in the present paper. The detection threshold at low energies is determined using pulsed signals. An alternative energy calibration for the decay events, free from any dead-layer effects can be performed by implanting radioactive ions decaying to known narrow resonances, e.g. ^{20}Na. Time and position correlations in a small detection volume can be used to identify possible different decay channels. An overview of precision measurements using this technique is given to prove the strength of the method.

PACS:23.40.-s, 29.40.Wk

*present address: CEA/Saclay, Gif-sur-Yvette Cedex, France

I. INTRODUCTION

The β decay of nuclei close to the driplines is in many cases characterised by a large Q_β-value, opening up a variety of decay modes such as β-delayed particle emission. Some of these decay branches, which often have a small branching ratio ($10^{-4} - 10^{-6}$), are very sensitive to particular nuclear structure properties. Their study can therefore reveal unique information.

Most measurements so far have employed low-energy (typically 60 keV) beams produced with the Isotope Separation On-Line (ISOL) method, stopped on a thin foil or a tape surrounded by silicon detectors and/or gas counters [1, 2]. In these set-ups the β-delayed ions undergo an energy loss in the implantation foil, and the dead layers of the detectors. This can complicate the energy calibration and distort the spectra of the emitted ions, and will affect the minimum threshold energy at which ions can be detected. Furthermore, the low-energy part of the β-delayed particle spectrum can be overwhelmed by the β background. Finally, a correct normalization is difficult as the number of implanted atoms and the detection efficiency are difficult to determine with high accuracy.

Implantation of reaction products in double-sided silicon strip detectors (DSSSDs) has been used in a series of experiments dealing with α decay [3], or to investigate properties of nuclei close to the proton dripline [4]. Specific states of the neutron-deficient nuclei are populated in nuclear reactions. Their characteristic charged-particle radioactivity (α decay, ground-state proton decay, and β-delayed proton emission), measured with the DSSSD, is used to tag γ-ray transitions (recoil decay tagging, RDT). The method was shown to be highly insensitive to β particles [4, 5].

Some features of the RDT-method can now be used in β-decay studies when the radioactive beam is directly implanted in the DSSSD. Energetic radioactive ion beams from post-accelerated ISOL facilities or from in-flight facilities have the advantage over conventional ISOL systems in that, using this method, individual decays can be followed.

The general properties of the implantation technique were described in a previous publication [6]; in this paper we report about recent developments made regarding the measurement of very weak β-delayed charged-particle emission channels.

II. METHOD

In order to extract absolute branching ratios, the implantation technique is designed to use the same detector for counting the number of implanted radioactive nuclei and detecting the emitted charged particles. This provides a reliable normalization and a high detection efficiency of the charged-particle channels compared to the use of an external source.

Post-accelerated ISOL beams have the advantage to be in many cases pure, intense and well defined in energy. This makes it possible to perform direct measurements of the desired decay channels without any unwanted beam contaminants. For the implantation technique the energy of the beam is tuned in such a way that the ions are stopped around the middle plane of the detector. The beam can be de-focused in order to obtain a rather uniform distribution on the detector surface.

In our experiments we used a DSSSD, manufactured by Micron Semiconductor Ltd.,

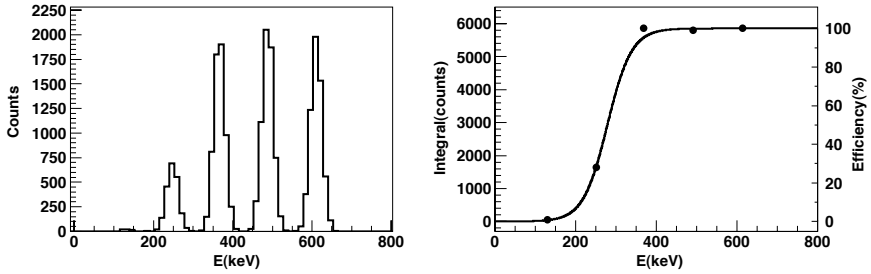

Figure 1: Left: pulsed signal counts in one strip as a function of energy. Right: integrated peak areas as a function of energy fit by a Fermi function, defining the detection efficiency at low energies.

having an active area of 16 × 16 mm^2 and a thickness of 78 μm. The front face consisted of 48 $p + n$ junction strips while the back face had 48 $n + n$ ohmic strips perpendicular to the first ones, defining a total of 2304 pixels. The strip pitch was 335 μm while the strip width was 300 μm. The energy signals and logic signals for each strip were collected using conventional electronics – charge-integrating preamplifiers and shaping amplifiers.
The following beams have already been implanted using this method: ^{6}He, and ^{18}Ne at the Cyclotron Research Centre (CRC) in Louvain-la-Neuve, ^{8}Li, ^{9}Li, and ^{11}Li at TRIUMF in Vancouver, ^{12}B, ^{12}N, and ^{20}Na at the Kernfysisch Versneller Instituut (KVI) in Groningen.

A. Detection efficiency at low energy

Since the shape of the energy spectrum of the charged particles emitted in the decay contains valuable structure information, it is important to extend the detection to the lowest possible energies. As the radiation is emitted inside the detector's active volume, dead layers do not play a role and the detection threshold is essentially determined by the electronic noise. The cutoff is not sharp and is determined by the electronic channel; it is thus different for each detector element.
A pulse generator can be employed to measure the detection efficiency at low energy: we sent a known number of signals, at 5 different amplitudes around the limit of detection, to the preamplifiers. The signals generating a trigger were recorded, producing peaks in the energy spectra corresponding to the pulser amplitudes, see Fig. 1(left) for an example. For each strip the detection efficiency was calculated by fitting the peak areas as a function of energy using a Fermi function with 2 parameters (Fig. 1 right): the slope of the function and the energy at 50% efficiency. The total efficiency curve of the detector was constructed as a weighted mean of all the fits on the strips, where the weight was given by the number of ions implanted in the strip during an actual measurement. We applied this procedure during our experiments,

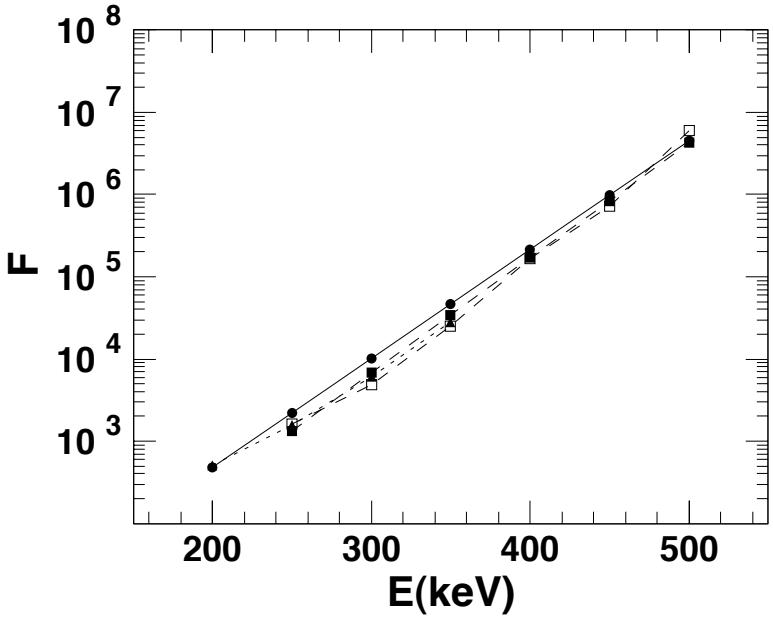

Figure 2: β-suppression factor $\mathcal{F}$ as a function of energy. Dots: ^{6}He-experiment; Squares: ^{18}Ne-experiment, filled squares corresponding to the full statistics and empty squares to beam-off events; Triangles: ^{11}Li-experiment, β particles emitted in the decay of ^{11}Be.

obtaining thresholds ranging from 200 keV to 400 keV, mainly due to the different amplification settings used in each case.

B. β suppression

At low energies, apart from any electronic noise considerations, one has to deal with the huge background arising from β particles. By segmenting the detector into pixels (requiring only one signal in a strip on each face) the influence of the β particles can be strongly reduced, since the maximum energy deposited in a pixel can be very small. Further reduction of the β background can be achieved by setting a maximum limit for the energy difference between the strip signals from the two sides of the detector [6]. This way it is possible to eliminate those β particles, which diffuse mainly along one strip on one side depositing a large fraction of their energy, at the same time generating only a small signal above the threshold in one of the strips on the other side.
The β-suppression factor $\mathcal{F}(E)$ is defined as the ratio between the total emitted β

particles and those detected above the energy E. We measured $\mathcal{F}(E)$ in a series of cases, presented in Fig. 2. The ^{18}Ne nucleus is a pure β^+ emitter, with particles up to $Q = 3.4$ MeV; we implanted it in our DSSSD with a short (1.5 s - 1.5 s) on/off beam modulation, in order to obtain a pure decay spectrum during the beam-off periods. The spectrum is presented in Fig. 3, and contains signals originating from the decays of ^{18}Ne and its daughter ^{18}F ($Q_{\beta^+} = 0.6$ MeV). The factor $\mathcal{F}(E)$ was calculated from the number of detected events, knowing the total number of implanted ions and the fraction of expected decays due to the observation window. The calculation was also performed for the full statistics, which served to check the contribution of ^{18}F (different in the two cases because of its half life, much longer than that of ^{18}Ne); in this case, the spectrum of the β particles was fitted with an exponential decay in order to subtract the contribution due to low-energy events from scattered beam particles. The same procedure was adopted with the data collected from the decay of the ^{6}He nuclei ($Q_{\beta^-} = 3.5$ MeV), and those from the decay of ^{11}Be ($Q_{\beta^-} = 11.5$ MeV); the latter were obtained by implanting ^{11}Li nuclei with a long beam on/off modulation (20 s - 20 s), which produced, after a few seconds in the beam-off periods, a pure ^{11}Be-decay spectrum.
As shown in Fig. 2, the measurements gave similar results. The data were collected from very different amounts of the total activity (from 4.61×10^8 implanted ions for ^{6}He to 1.16×10^7 for ^{11}Be) and electronic amplifications, which induced different detection thresholds. Since no corrective factors were introduced, we conclude that the β-suppression factor in our DSSSD is substantially independent from the end-point energy of the decay, reaching about 10^7 for signals recorded beyond 500 keV.

C. Reconstruction of ion emission events

By considering only single-pixel events and a limited strip energy difference, β particles events are strongly suppressed. For the emitted ions, the generation of a signal in one single pixel depends on the energy and type of the ions and the dimensions of the DSSSD. The properties of the DSSSD should be chosen in such a way that the ranges of emitted ions are substantially smaller than the dimensions of one pixel. Simulations can be performed to evaluate the actual response of the detector. In our case, the simulation of $\alpha + d$ events emitted in the β decay of ^{6}He [6] showed that virtually all (99.94%) events above the detection threshold are confined within one pixel, assuming a homogeneous implantation distribution. The efficiency for the detection of the decay events was therefore only limited by the possible dead time of the acquisition system and could be determined accurately.
Another effect influences the identification of events in the detector. When the implantation takes place in the inter-strip area, its large energy deposition may generate signals in two neighboring strips on the same side, both above the detection threshold. The weaker signal from the decay would be split in the same way, but it may happen that only one part is above the threshold. In these cases, a reconstruction of the implantation event was made by adding the two energy signals and assigning the summed energy to one strip (the one with the higher signal) to recover the correct normalization. This method becomes important when one makes use of the correlation between the implantation and subsequent decay events in the same pixel (see below Section II E).

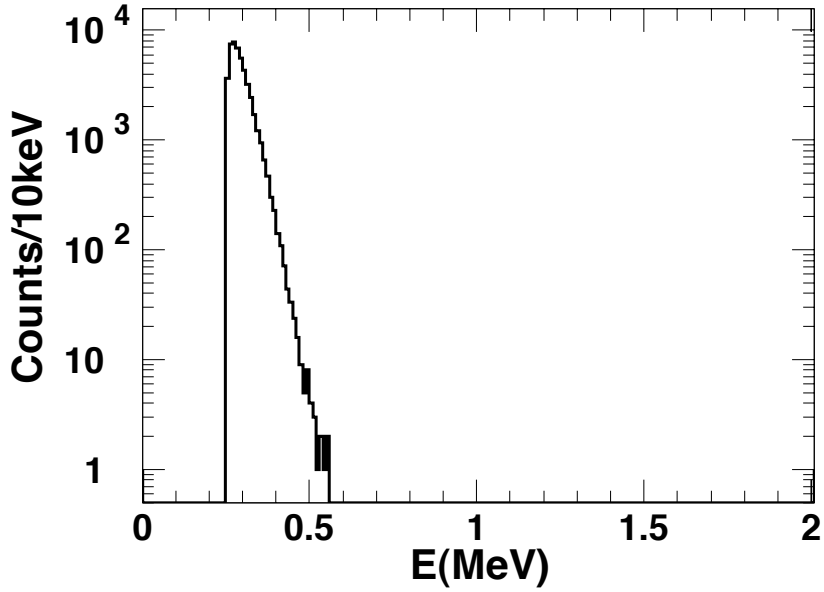

Figure 3: Spectrum of detected events following the implantation of ^{18}Ne, and during the 1.5 s beam-off period when only β^+ particles are expected.

D. Energy calibration

Usually the energy calibration of silicon detectors is performed using an external source emitting α particles of known energies. Sources are available commercially in the energy range between 3 MeV and 6 MeV; in this region the calibration will have the best precision, usually better than 0.1% for a detector with a resolution around 30 keV. However, if an accurate measurement is needed, a correction for the dead layer present on the surface of silicon detectors has to be added: for example, in a typical aluminium layer of 0.5 μm, α particles of 5 MeV energy lose about 80 keV [7]. The energy loss depends on the type and energy of particles, and becomes especially important at low energies.
The energy of particles before they penetrate into the detector has to be calculated using energy-loss tables, once the incident angle of the particle and the thickness of the dead layer are known. The latter can be determined, by placing a source at different angles relative to the detector plane and measuring the shift in the position of the energy peaks. We adopted such a procedure, recording the spectra produced by an α source placed at 90 and 22 degrees with respect to the plane of our DSSSD. From the difference in the position of the energy peaks, an energy loss of 45(1) keV was found, corresponding to a thickness of 0.340(3) μm of silicon equivalent.

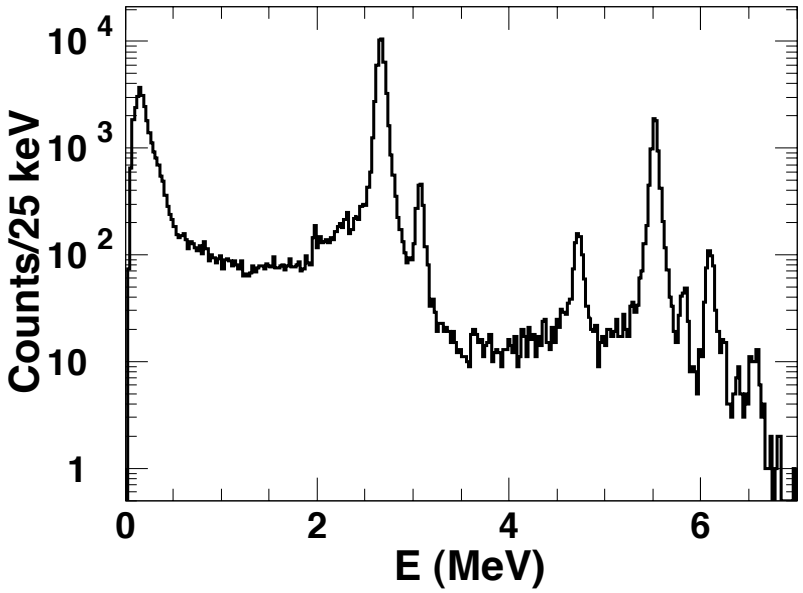

Figure 4: Spectrum of the charged particles emitted in the β decay of ^{20}Na nuclei implanted in the DSSSD. The peaks correspond to unbound states in ^{20}Ne above the α-emission threshold.

Such a method suffers from the uncertainties propagating from the two calibration measurements, and of course relies on the accuracy of energy loss tables. Another possibility is present, offered by the availability of radioactive ion beams, if the aim of an experiment is to measure the energy of events originating in the detector itself. An internal calibration can be performed by directly implanting unstable ions, which decay emitting charged particles at sharp energies. The ^{20}Na nucleus (with a half life of 448(2) ms) undergoes β^+ decay towards ^{20}Ne, with about a 20% branching ratio towards narrow unbound states, that in turn decay emitting an α particle. The method has been used in [8], and we adopted it in the occasion of the measurements at the KVI facility in Groningen, obtaining the spectrum shown in Fig. 4. The peaks range between 2.5 MeV and 6.5 MeV and have widths essentially determined by the detector's intrinsic resolution. This method relies on a single calibration and avoids the correction for the dead layer; however, the effect of β summing has to be taken into account, since the total energy deposited in a pixel is measured. This information is provided by simulations of the energy loss of β particles in the DSSSD.

E. Time and position correlation

If the implanted ion has only one decay channel, the beam is tuned in on- and off-periods to obtain a clean energy spectrum. Fig. 3 shows the pure β-decay spectrum of ^{18}Ne, recorded during the beam-off periods: this demonstrates that no other events are recorded above the β-particle signals, making it possible to measure ion-emission spectra from very weak decay channels as in the case of ^{6}He. When more decay channels are open, the identification is based on the spectrum of the emitted particles, on the timing behavior of the radiation, and on correlations between the implantation signal, the decay signature, and possible further signals from daughter-decay. Both time and position correlations can be applied: the latter is based on the segmentation of the detector, as the daughter nuclei remain well-localized in the detection element where the mother nucleus was implanted. Time correlations are made acquiring a time stamp for each event. In this case continuous beam implantation can be used.
If the beam rate is high, a second ion can be implanted after a first implantation before all decays take place. To avoid this, a first rule of thumb for the choice of the beam rate is having the beam rate per pixel lower than the decay rate of the longest living daughter nucleus.
Specific precise corrections can be calculated if the implantation rate in one single pixel, λ_I, and the decay rates are known. When an ion is implanted at time $t_0 = 0$ s:

1. the probability density function, $p_M(t_1)$, to observe the mother decay at time t_1 before a second implantation occurs, can be written in the following form:

$$p_M(t_1) = \lambda_M e^{-\lambda_M t_1} \times e^{-\lambda_I t_1}, \tag{1}$$

   where λ_M is the decay rate of the mother nuclei. The corresponding total probability is found integrating over t_1 from 0 to $+\infty$:

$$P_M = \frac{\lambda_M}{\lambda_M + \lambda_I}. \tag{2}$$

2. If also the daughter nucleus is unstable, the probability density function, $p_D(t_1, t_2)$, to have a daughter decay at time t_2 after the mother decay at time t_1 without a second implantation event is:

$$p_D(t_1, t_2) = \lambda_M \lambda_D e^{-(\lambda_M - \lambda_D)t_1} e^{-(\lambda_D + \lambda_I)t_2}, \tag{3}$$

   with λ_D the decay rate of the daughter nuclei. In this case the probability, P_D, is found after integration over t_2 from t_1 to $+\infty$, followed by the integration over t_1 from 0 to $+\infty$:

$$P_D = \frac{\lambda_D}{\lambda_D + \lambda_I} \times \frac{\lambda_M}{\lambda_M + \lambda_I} \tag{4}$$

The correlation technique has been used to identify the ^{9}Li+d and ^{8}Li+t channels in the β decay of ^{11}Li ($T_{1/2}$ = 8.5(2) ms), which was done for the first time during a measurement at TRIUMF. A correction for the branching ratio could be estimated using equation (4).

III. RESULTS

Using the implantation technique we have performed the measurement of the β decay of several unstable nuclei, among which the halo nuclei ^{6}He and ^{11}Li. Future plans include the measurement of the decay of ^{8}B to obtain information about its neutrino spectrum.
The branching ratio (BR) of the β-delayed $\alpha + d$ emission in the ^{6}He decay was measured at the CRC in Louvain-la-Neuve, Belgium [6] with high precision; $BR = (1.65 \pm 0.1) \times 10^{-6}$ above the energy threshold $E_{\mathrm{c.m.}} = 525$ keV. The summed energy spectrum of the $\alpha + d$ particles has also been obtained [9].
The identification of the ^{9}Li+d and ^{8}Li+t channels in the ^{11}Li decay was achieved and the branching ratio and energy spectrum of both channels were measured. We also obtained the energy spectra for both ^{8}Li and ^{9}Li nuclei.
Excited states in the ^{12}C nucleus above the triple α threshold were investigated by implanting both ^{12}B and ^{12}N beams at the KVI facility in Groningen, The Netherlands. The 0^{+} Hoyle state at 7.65 MeV in ^{12}C, just 0.3 MeV above the break-up threshold, has been observed and the branching ratios for β^{+} and β^{-} decay to the states in the 3α continuum were revised, with a precision improved by a factor 10 [10].

IV. CONCLUSIONS AND OUTLOOK

The implantation technique using a segmented silicon detector is discussed with respect to its use in measurements of β-delayed charged-particle emission.
Due to the β suppression and the high detection efficiency for ions, precise branching ratios and energy spectra down to low energies can be obtained. The possibility of an internal energy calibration, and the use of time and position correlation to identify different decay channels are described.
Further aspects can be considered for the improvement of the method. Auxiliary β and γ detectors as well as ΔE detectors can be added to the set-up to further distinguish between different signals. The possibility of cooling the DSSSD can result in a better resolution and reduction of the leakage current together with more stable conditions.

---

[1] K. Riisager, M. J. G. Borge, H. Gabelmann, P. G. Hansen, L. Johannsen, B. Jonson, W. Kurcewicz, G. Nyman, A. Richter, O. Tengblad , et al., Phys. Lett. B **235**, 30 (1990).
[2] M. J. G. Borge, L. Johannsen, B. Jonson, T. Nilsson, G. Nyman, K. Riisager, O. Tengblad, K. Wilhelmsen Rolander , and the ISOLDE Collaboration, Nucl. Phys. A **560**, 664 (1993).
[3] R. D. Page, P. J. Woods, R. A. Cunningham, T. Davinson, N. J. Davis, A. N. James, K. Livingston, P. J. Sellin , and A. C. Shotter, Phys. Rev. C **49 (6)**, 3312 (1994).

[4] E. S. Paul et al., Phys. Rev. C **51 (1)**, 78 (1995).
[5] P. J. Sellin et al., Nucl. Instr. and Meth. A **311**, 217 (1992).
[6] D. Smirnov, F. Aksouh, S. Dean, H. De Witte, M. Huyse, O. Ivanov, P. Mayet, I. Mukha R. Raabe J. C. Thomas , et al, Nucl. INstrum. Methods Phys. Res. A **547**, 480 (2005).
[7] J. F. Ziegler, J. P. Biersack , and U. Littmark, *The Stopping and Range of Ions in Solids* (Pergamon Press, New York, 1985).
[8] W. T. Winter, S. J. Freedman, K. E. Rehm, J. P. Schiffer, Phys. Rev. C **73**, 025503 (2006).
[9] R. Raabe, J. Büscher, J. Ponsaers , et al, Phys. Rev. C **80**, 054307 (2009).
[10] S. Gadegaard Pedersen et al., Proceedings of Science **NIC-IX**, 244 (2006).

Chapter 3

Charged-particle emission in the ^{6}He β decay

Paper II: ^{6}He : β-decay channel into the $\alpha + d$ continuum

The β-delayed deuteron emission is a peculiar decay mode that for the moment only has been observed close the neutron dripline in the β decay of the two halo nuclei ^{6}He and ^{11}Li [39]. This decay channel of ^{6}He was studied for the first time in a measurement at ISOLDE [40] from which a branching ratio of $\bar{B} = (2.8 \pm 0.5) \times 10^{-6}$ was obtained for deuteron energies above 350 keV. Following experiments [41, 42] confirmed the order of magnitude of the transition probability but differed in its absolute value. Alongside the experimental work, progress has been made in the theoretical description of the decay channel with special interest in the description of the ^{6}He ground state wave function. At first, all theoretical studies [40, 64, 65] predicted a value for the branching ratio that was one or even two orders of magnitude larger than the experimental results. A cancellation in the Gamow-Teller matrix element between halo and core decay contributions afterwards explained this discrepancy. This cancellation effect was first shown in a semi-microscopic study [66], this property was later confirmed in various theoretical works [67–70]. In the analogue deuteron emission channel in the β decay of ^{11}Li, on the other hand, theoretical [71–73] and experimental [45] studies confirm the dominant contribution of the halo decay in the matrix element, due to the even more extended wave function of the ^{11}Li ground state. To obtain the large quenching in the ^{6}He Gamow-Teller matrix element and in order to reproduce the correct energy dependence of the transition probability, the initial ^{6}He and final $\alpha + d$ wave functions have to be

described precisely. Hence, it is important that the branching ratio and the $\alpha + d$ energy spectrum are experimentally measured with good accuracy to put valuable constraints on the theoretical models.

This chapter contains the article that was published in *Physical Review C 80, 054307 (2009)* and describes three experimental runs to study the deuteron-emission channel in the β decay of ^{6}He. The measurements were performed at the Cyclotron Research Centre at Louvain-la-Neuve (Belgium) [74] where for the first time ^{6}He nuclei were directly implanted in a highly segmented silicon detector. The transition probability as a function of the energy of the emitted α and deuteron was obtained with a low-energy threshold at a deuteron energy of 350 keV. This result agrees with the large statistics data from Anthony et al. [42], both in shape and magnitude. The weigthed average of the three successive experiments gave a branching ratio $\bar{B} = (1.65 \pm 0.10) \times 10^{-6}$, corresponding to a transition probability $W = (1.42 \pm 0.09) \times 10^{-6}$ s^{-1} for a deuteron energy $E_d \geq 350$ keV. The uncertainty on the branching ratio is hereby drastically reduced from 50% to 6%. The results are discussed with respect to the most recent theoretical work dealing with the $\alpha + d$ emission channel in the ^{6}He β decay [70].

Measurement of the branching ratio of the ^{6}He β-decay channel into the $\alpha + d$ continuum

R. Raabe,[1] J. Büscher,[1] J. Ponsaers,[1] F. Aksouh,[1] M. Huyse,[1] O. Ivanov,[1] S. R. Lesher,[1,*] I. Mukha,[1,†] D. Pauwels,[1] M. Sawicka,[1] D. Smirnov,[1] I. Stefanescu,[1] J. Van de Walle,[1,‡] P. Van Duppen,[1] C. Angulo,[2] J. Cabrera,[2,§] N. de Séréville,[2,¶] I. Martel,[3] A. M. Sánchez-Benítez,[3] and C. Aa. Diget[4]

[1]*Instituut voor Kern- en Stralingsfysica, K.U.Leuven, B-3001 Leuven, Belgium*
[2]*Centre de Recherches du Cyclotron, UCL, Chemin du Cyclotron 2, B-1348 Louvain-la-Neuve, Belgium*
[3]*Departamento de Física Aplicada, Facultad de Ciencias Experimentales, Campus de El Carmen, Av. de las Fuerzas Armadas s/n., Univ. de Huelva, 21071 Huelva, Spain*
[4]*Department of Physics and Astronomy, University of Aarhus, Ny Munkegade, Building 1520, DK-8000 Aarhus C, Denmark*[**]

We measured the deuteron-emission branch of the β decay of the halo nucleus ^{6}He using the technique of implantation in a highly segmented silicon detector. The method, used here for the first time with a beam of ^{6}He ions, ensured a precise normalization; the value obtained for the branching ratio is $\bar{B} = (1.65 \pm 0.10) \times 10^{-6}$ (6% error). The summed energy spectrum of the emitted α and d particles has also been measured. The results allow a comparison between calculations from various models, potentially setting strong constraints on the precision required for the description of the ^{6}He ground-state wave function.

PACS:23.40.Hc; 27.20.+n

---

[*]present address: Department of Physics, University of Richmond, Richmond, Virginia 23173, USA
[†]present address: University of Seville, 41012 Sevilla, Spain
[‡]present address: ISOLDE, CERN, Geneva, Switzerland
[§]present address: Centre for Space Radiations (CSR), UCL, Louvain-la-Neuve, Belgium
[¶]present address: IPN, IN2P3/CNRS and Université Paris Sud, F-91406 Orsay Campus, France
[**]present address: Department of Physics, University of York, York YO10 5DD, UK

I. INTRODUCTION

To date, most experimental investigations performed on halo nuclei [1] have involved the measurement of nuclear reactions. In such cases, knowledge of the halo structure relies on model-dependent reaction mechanisms. However, the theory describing β decay is well-established, offering an alternative and reliable probe to study halo properties. In addition, at large distances β decay is sensitive to the details of the wave function.

Peculiarities in the β decay of halo nuclei were identified from measurements at the ISOLDE facility in CERN [2]. The decay of these systems is characterized by large available energies (Q-values) and by low breakup thresholds in the daughter nuclei, so that the feeding to continuum states and the subsequent emission of nucleons or ions becomes possible. The decay of the ^{6}He nucleus mainly proceeds to the ground state of ^{6}Li ($Q = 3.508$ MeV), but the $\alpha + d$ channel is also energetically allowed ($Q = 2.033$ MeV). This is also referred to as the β-delayed deuteron-emission channel, a peculiar decay mode heretofore observed only in the halo nuclei ^{6}He and ^{11}Li [3]. The corresponding branching ratio and the spectrum of the emitted particles depend on the ^{6}He ground-state wave function and the $\alpha + d$ interaction potential.

The first observation of deuteron emission in the decay of ^{6}He was made at ISOLDE [4]. The authors measured a branching ratio of $(2.8\pm0.5)\times10^{-6}$ for a deuteron energy threshold of 350 keV. After a new experiment, the value was corrected to $(7.6\pm0.6)\times 10^{-6}$ [5]. More recently, another measurement performed at the TRIUMF facility [6] obtained the result $(1.8\pm0.9)\times10^{-6}$ (for the same deuteron energy threshold), which is lower than the values obtained at ISOLDE. The large overall uncertainty associated with the TRIUMF result is related to the determination of the detection efficiency (geometrical factors and electronic threshold). However, large statistics allowed a precise measurement of the shape of the energy spectrum of the emitted α and d particles.

At the time of the first measurements, all theoretical calculations predicted a much larger value for the $\alpha + d$ branching ratio: about 10^{-4} for an R-matrix model [4], 2×10^{-4} for a two-body model [7] and (3–4) $\times$ 10^{-5} for a three-body model [8]. The disagreement with experimental results was afterward explained in terms of a cancellation between two parts of the Gamow-Teller matrix element, related to the "internal" and "external" regions of the ^{6}He ground-state and $\alpha + d$ scattering wave functions, respectively, and in terms of overlaps in the two regions that have similar magnitudes but opposite signs. This property was first detected in a semi-microscopic study [9], and then confirmed in successive works with an improved model for ^{6}He [10] and a fully microscopic description of its decay [11]. A study within the R-matrix framework [12] reached the same conclusions by including a contribution to the β-decay matrix element coming from the external region, using an $\alpha + {}^2n$ wave function with a two-body asymptotic form for the ground state of ^{6}He. The latter description is analogous to a decay route proceeding first to the breakup of ^{6}He into ^{4}He + ^2n, followed by the β decay of the di-neutron into a deuteron, as already suggested in the work of Borge *et al.* [5] as a possibility to reproduce the experimental data. All these studies point to the high sensitivity of the branching ratio to the external part of the ^{6}He wave function, thus confirming that the β decay is a precise probe of the halo structure.

A more recent study [13] has reexamined the decay process by employing $\alpha + n + n$

three-body wave functions in hyperspherical coordinates for ^{6}He [14] and a potential model for the $\alpha + d$ scattering states. While confirming the cancellation effect, the authors point out that the agreement with experimental data is very sensitive to the node structure of the initial and final states (i.e., to the ^{6}He wave function and the $\alpha + d$ states as determined by the $\alpha + d$ potential). Small modifications of the latter potential may significantly vary the deuteron-emission branching ratio, and this can be used to obtain a good agreement with the data (as done in Ref. [13]). Conversely, one can argue that a potential should be used that consistently reproduces the ^{6}Li ground-state binding energy and the $\alpha + d$ phase shifts (with a "fair" agreement being provided by the potential used in Ref. [13]), thus using the deuteron-emission branching ratio as a test of the ^{6}He wave function. More precise experimental data would make this test more stringent and would also put stronger constraints on the parameters of the calculations.

Here we report on new experimental results obtained using an implantation technique that allowed for a precise normalization. This is the first time that ^{6}He nuclei are directly implanted in a highly segmented silicon detector. The technique has been described in a previous publication [15], along with preliminary results for the ^{6}He decay. In the new experiments discussed herein, we measured the branching ratio of the $\alpha + d$ channel with a precision of 6%, which is a significant improvement over earlier results. The transition probability as a function of the energy of the emitted particles was also obtained with a low-energy threshold at 350 keV (deuteron energy), as was done in previous measurements.

II. EXPERIMENTAL DETAILS AND RESULTS

The measurements were done at the Cyclotron Research Centre of Louvain-la-Neuve (Belgium) [16]. The experimental technique (implantation of the radioactive nuclei in a silicon detector) requires a beam of ions at an energy sufficiently high to perform the implantation. A beam of ^{6}He ions at an energy $E = 7.9$ MeV was obtained using two coupled cyclotrons and the on-line isotope-separation method. The radioactive ^{6}He nuclei (half life $T_{1/2} = 0.807$ s [17]) were produced through the ^{7}Li(p,2p)^{6}He reaction by impinging on a LiF target with a 200-μA, 30-MeV proton beam provided by the CYCLONE30 cyclotron. After diffusion out of the target and ionization in an Electron Cyclotron Resonance (ECR) source, the nuclei were injected into the CYCLONE110 cyclotron and postaccelerated to the required energy. The second cyclotron was tuned to act as a powerful mass separator, eliminating isobaric impurities to levels better than 10^{-3} [18]. At the detection station, the beam was directly implanted in a thin double-sided silicon strip detector (DSSSD), 78 μm thick. The energy of the beam was chosen in order to stop the ions around the middle plane of the detector. According to calculations performed with SRIM [19], the implantation depth was 40 μm with a straggling (FWHM of the depth distribution) smaller than 2 μm. The intensity of the beam was maintained at the low value of about 6000 ions/s to minimize detector damage and the dead time of the acquisition system. To obtain a rather uniform distribution on the detector surface, the beam was defocused by using quadrupole lenses positioned about 2 m upstream from the detector. The implantation was confined within the detector surface by a collimator, having a square hole the size of the detector, positioned about 10 cm from the detector surface.

The DSSSD had an active area of 16 × 16 mm^2, and each face was divided into 48 strips with the strips on the back face perpendicular to the ones on the front face. A total of 2304 pixels were defined by requiring only two signals in coincidence, one from each side of the detector ("multiplicity 1-1" events). The energy calibration of all channels was performed using standard α-particle calibration sources, correcting for the effect of the dead layer of the detector. At low energy, linearity was checked using a pulser. Many details and characteristics of the detection technique are described in Refs. [15] and [20], so we review here only those aspects that are most relevant for the present measurements.

The Q-value of the $\alpha + d$ channel in the β decay of ^{6}He is 2.033 MeV. The energy is shared among the electron, the neutrino, and the two ions. Since the leptons carry almost no momentum, the ions are emitted almost back-to-back with energies inversely proportional to their masses. The range of 1-MeV deuterons in silicon is 12.2 μm and as a result the ions do not escape from the detector. More precisely, because the interstrip distance measures 35 μm, the combined energy of the emitted α particle and deuteron is collected within a single pixel. Conversely, β particles have a much larger mobility and deposit only a very small energy into a pixel. With an electronic detection threshold just above 100 keV, only about 1.6% of the total electrons emitted by multiplicity 1-1 events were detected. For very few events, the maximum detected energy for electrons attained 600 keV. Above this energy, only one β particle out of more than 10^7 emitted is detected, as shown in an analysis of the detector behavior [20] based on previous measurements and a simulation of the detector response [15, 21].

A small fraction of the events generated by the implantation of the ^{6}He nuclei produced signals in the energy range of interest (0.5 to 2 MeV) owing to incomplete charge collection in the detector and to ions, scattered along the beam line that still reach the detector. In our measurements, this fraction was around 10^{-4}, two orders of magnitude larger than the branching ratio for deuteron emission, so that the $\alpha + d$ decay events could not be identified in the overwhelming implantation background. For this reason, the ^{6}He beam was modulated in periods of 1 s beam-on and 2 s beam-off, and only the $\alpha + d$ events occurring during the beam-off period were accepted. The beam modulation was achieved by using a 1/3 Hz rotating shutter wheel with a 120° cutout placed in the beam path. The wheel also activated a photoresistor at each turn, giving a time reference that defined the beam-on and beam-off periods.

Instantaneous and complete suppression of the ion beam (to a level significantly better than 10^{-6}) required attention to various experimental factors. The use of a deflection magnet as described in Ref. [15] did not completely eliminate beam events during the beam-off period. With the use of a shutter wheel, the beam needs to be well collimated at the wheel position to avoid stray scattered particles from reaching the implantation detector. The precise definition of the transition between beam-on and beam-off periods is also important in calculating the number of decay events expected within a chosen time window. During our campaign we performed three measurements (including the one reported in Ref. [15]) on the ^{6}He nucleus to improve on these aspects of the experiment.

Figures 1(a) and 1(b) show the energy spectrum of all events recorded during the beam-off periods in Run 2 and 3, respectively (the same spectrum for Run 1 is presented in Fig. 8 of Ref. [15]). For Run 3, the dynamics of such events is shown in the inset of Fig. 1(b). The exponential fit gives a half life $T_{1/2} = 801(10)$ ms, as expected

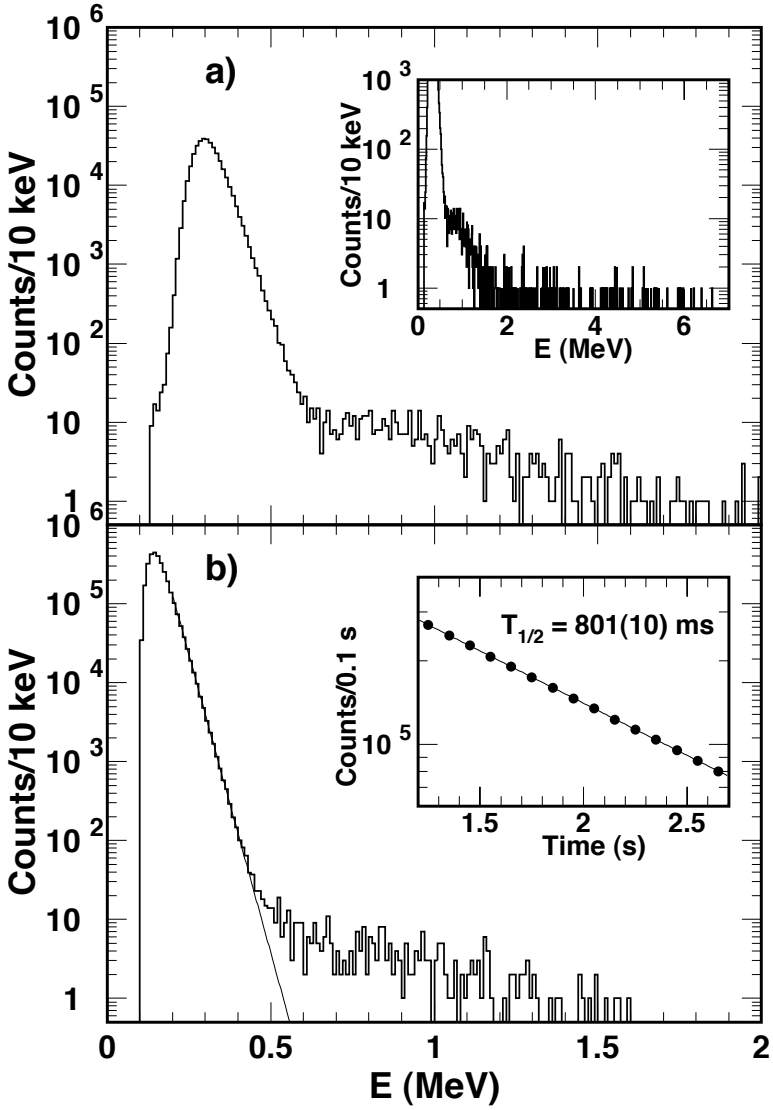

Figure 1: (a) Total-energy spectrum of events detected during the beam-off period following the implantation of ^{6}He in Run 2. The inset of (a) shows the same spectrum up to 7 MeV). Panel (b) presents the results for Run 3, which were done under the same conditions as Run 2. The β-particle signals have a maximum energy of about 600 keV. Above this value, events are due to $\alpha + d$ emission events. The thin solid line in (b) is an exponential function fitted to the β-particle spectrum up to 400 keV. The inset of (b) shows the time behavior of all decay events, where the time scale refers to the beginning of the beam-on period.

from the decay of ^{6}He. The uncertainty is mainly due to dead-time corrections that distort the decay curve. In the energy spectrum, pure β-decay events induce signals that decrease exponentially in number to a maximum energy of about 600 keV. The events at higher energy are due to the $\alpha + d$ emission channel (up to 2 MeV), plus any background. The presence of the latter is evident for Run 2 where events up to 6 MeV and beyond appear in the spectrum [see inset of Fig. 1(a)].

The background has two possible sources: I. constant background due to residual decay activity present in the detection chamber or due to cosmic rays and II. beam particles leaking through to the detector, around the shutter wheel, during beam-off periods (with a small fraction of them being capable of generating a signal in the energy range of interest). Type I events were evaluated in long, repeated off-line background measurements, with the detection chamber in the same location and conditions as during the actual beam irradiation. An observed weak α-decay activity was caused by a mechanical component in the detector chamber that had been contaminated by the calibration sources. The event rate was found to be essentially constant over the various runs and amounted to 1.2 ± 0.1 events/h, of which only 0.10 ± 0.02 events/h were in the energy range of interest. Given the total irradiation time in each run (10–80 hours), one can see that this contribution is small. Type II events are revealed by the presence of events at full implantation energy during the beam-off period. This was observed during Runs 1 and 2, but completely suppressed in Run 3 by improvements in the shutter wheel system. Using this improved setup we later measured in Run 4 the decay of the pure β^+ emitter ^{18}Ne ($T_{1/2} = 1.67$ s [22], $Q_{\beta^+} = 3.424$ MeV, which is similar to that of ^{6}He). As discussed in [20], no events were observed in the energy range 0.6–2.0 MeV for 1.30×10^8 implantations, placing an upper limit of 4 events for the corresponding range in Run 3 (where the observation time was four times longer). For the previous runs, type II background was estimated from the number of detected implantations in the beam-off period and the fraction, 10^{-4} [15], that would induce the background. Also, an analysis was made of the dynamics of the events of interest (between 0.6 and 2.0 MeV) as shown in Fig. 2. When only decay events were present (as in Run 3, Fig. 2 top), an exponential fit gave a half life $T_{1/2} = 0.83(18)$ s as expected for ^{6}He. For Run 2 (Fig. 2 bottom), a pure exponential decay gave a slower decay rate [where the corresponding half life would have been $T_{1/2} = 1.10(17)$ s], indicating the presence of a constant background. A second fit, this time using an exponential function fixed at the known ^{6}He decay rate plus a constant offset (free parameter), provided a quantitative estimate of the background.

Table I summarizes the relevant quantities for each run. The "events above β's" are those between 0.525 and 2 MeV detected during the beam-off period (with the "observation window" indicating the fraction of observed decays). Where necessary, β events were subtracted using an exponential fit (see Fig. 1). The net $\alpha + d$ events are obtained taking into account the background sources of type I and II just described (together in Table I). The branching ratio of the deuteron-emission channel is then calculated by dividing the number of $\alpha + d$ events by the number of implanted ions, and corrections are applied for the time window of the observation and for the dead time of the acquisition system. Beside the error on the number of $\alpha + d$ events, the main additional uncertainty originates from the count of the implanted ions, for which a fraction induces signals on two adjacent strips when the implantation occurs close to their common edge. This effect depends on the beam energy and for ^{6}He

Table I: Summary of the measurements with the ^{6}He and ^{18}Ne beams. See text for the definition of the $\alpha + d$ events. The weighted mean of the results for the branching ratio of ^{6}He into $\alpha + d$ is $\bar{B} = (1.65 \pm 0.10) \times 10^{-6}$.

Run	Duration	Implanted ions	Observation window	Events above β's	Background events	Net $\alpha + d$ events	Dead time beam off	Branching ratio (in 10^{-6})
1 (^{6}He)	10^h20^m	1.86×10^8	32%	96 ± 20	1 ± 1	95 ± 20	5.0%	1.7 ± 0.4
2 (^{6}He)	73^h05^m	5.11×10^8	42%	587 ± 24	162 ± 69	425 ± 73	4.0%	2.0 ± 0.4
3 (^{6}He)	82^h30^m	4.61×10^8	44%	319 ± 18	4 ± 4	315 ± 18	4.2%	1.62 ± 0.11
4 (^{18}Ne)	25^h47^m	1.30×10^8	29%	—	—	—	—	—

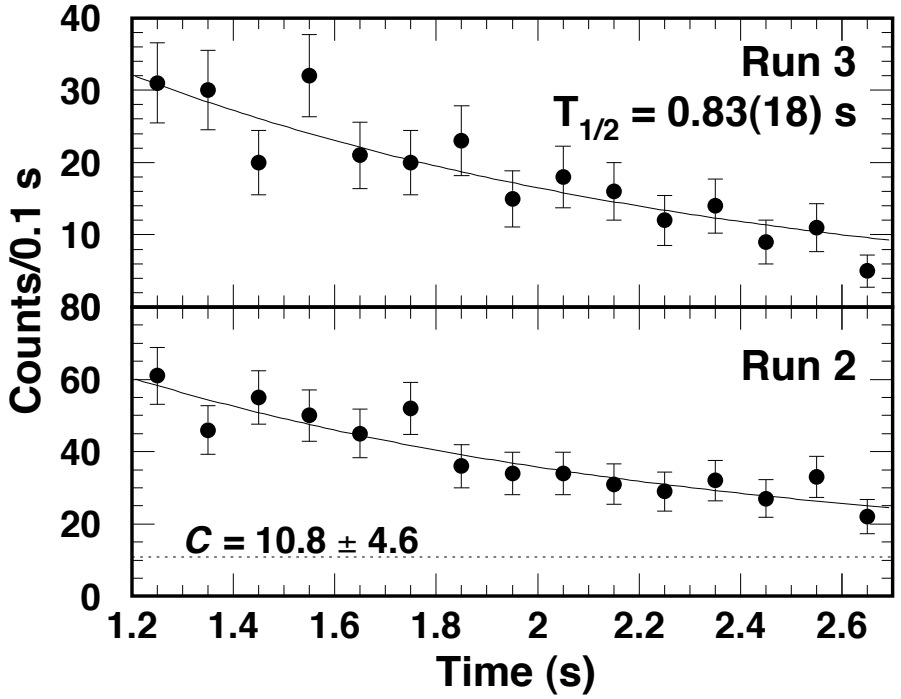

Figure 2: Dynamics for events with an energy between 0.6 and 2 MeV detected in the beam-off periods after the implantation of ^{6}He. The top panel shows Run 3, the bottom panel shows Run 2, and the time scale refers to the beginning of the beam-on period. Events in Run 3 were fitted with a single exponential (solid line) that yielded a half life $T_{1/2} = 0.83(18)$ s. For Run 2, the solid line is a two-component fit, with a constant offset (free parameter C) plus an exponential function with the decay rate of ^{6}He. The dotted line shows the level of the fitted offset. The result indicates that, of the total 587 ± 24 events, 162 ± 69 are due to background.

contributes to 5% of the total error. The weighted mean of the branching ratio values measured in the three runs is $\bar{B} = (1.65 \pm 0.10) \times 10^{-6}$. The energy threshold above which events were counted was $E_{\rm c.m.} = 525$ keV, corresponding to a deuteron energy $E_d = 350$ keV. This threshold is the same as the values reported in Refs. [4–6].
Since the energy dependence of the background present in Runs 1 and 2 was not known, a reliable energy spectrum of the $\alpha + d$ events was obtained using only the data collected in Run 3. A procedure was adopted to subtract the β events at low energy, by fitting them with an exponential function as shown in Fig. 1(b). The resulting $\alpha + d$ spectrum is shown in Fig. 3 in units for the transition probability, together with the data from Ref. [6] and the theoretical prediction from Ref. [13].

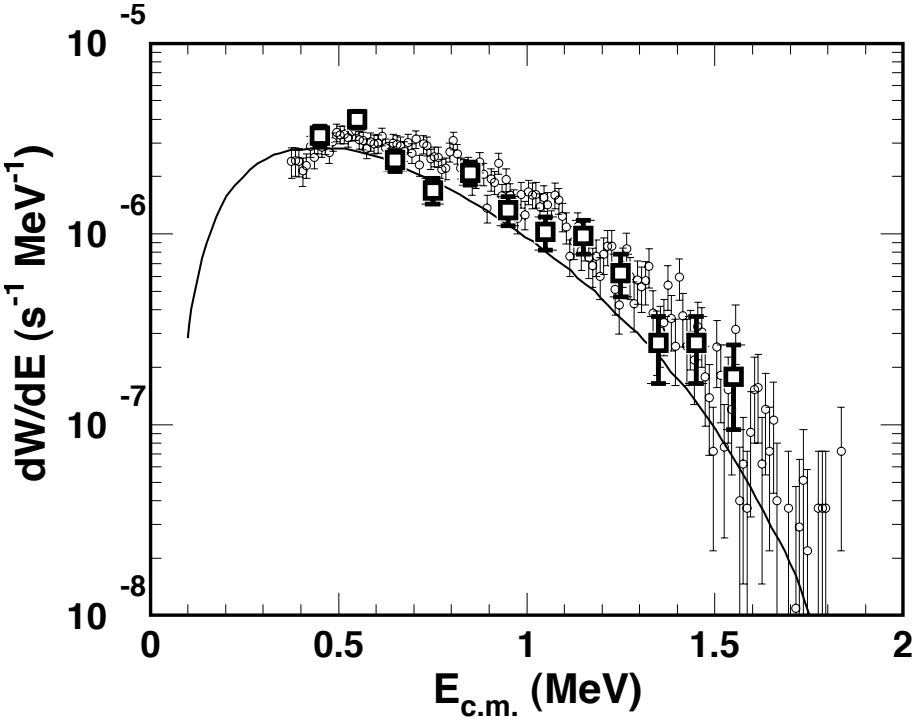

Figure 3: Transition probability as function of the centre-of-mass energy $E_{\mathrm{c.m.}}$ for the $\alpha + d$ branch of the β decay of ^{6}He. The squares are our results from Run 3 and circles are data from Ref. [6]. The solid line is the prediction from Ref. [13] corresponding to a Gaussian $\alpha + d$ interaction potential (V_m in Ref. [13]).

III. DISCUSSION

The energy spectrum of the $\alpha + d$ events measured using our technique agrees very well with the data from Ref. [6], both in shape and magnitude. We confirm the low value of the branching ratio for this channel and considerably reduce its uncertainty, from 50% to 6%. The new value corresponds to a transition probability $W = (1.42 \pm 0.09) \times 10^{-6}$ s^{-1} (for a deuteron energy $E_d \geq 350$ keV). The low value is due to the cancellation between two parts of the Gamow-Teller matrix element, as pointed out in Ref. [9] and then confirmed by several successive theoretical calculations. The various models [8, 11–13], briefly reviewed in Section I, agree in predicting ratios on the order of 10^{-6}. We base our discussion on these calculations because they cover the approaches presently viable. With the improved precision of our results, a more thorough comparison becomes possible.

The Gamow-Teller matrix element connects the initial ^{6}He ground-state and final scattering $\alpha + d$ wave functions through the well-known spin-isospin operators. The

cancellation takes place between the contributions of two separate regions of the spatial integral; the exact amount depends upon the choice of *both* the ^{6}He and $\alpha + d$ wave functions. It is therefore difficult to separately draw conclusions about the two. However, from the analysis of Refs. [11] and [13], some points clearly emerge. Consider first the $\alpha + d$ wave function. The correct order of magnitude of the branching ratio is reproduced only if such a wave function has two nodes, one of which is located at small distances. If the wave function is calculated from a potential model as in Refs. [8] and [13], the result depends upon the choice of the $\alpha + d$ potential. In Fig. 3 we show the transition probability from Ref. [13], corresponding to a Gaussian potential (the one shown is the V_m appearing in the Erratum [13]) capable of reproducing at the same time the experimental ^{6}Li binding energy and (fairly) the $\alpha + d$ low-energy phase shifts. The authors show that a better agreement can be achieved by a small renormalization of the potential. In Ref. [8] the $\alpha + d$ wave function does not have nodes, which is one of the reasons for the large overestimate (by about a factor 20) of the branching ratio. In the parameter-free model of Ref. [11] the agreement is again good (the prediction being about a factor of 2 larger than our measured value). The $\alpha + d$ wave function is there obtained from a microscopic calculation employing a nucleon-nucleon potential; the choice of the basis states makes it possible, both here and in Ref. [13], to reproduce both the ^{6}Li binding energy and $\alpha + d$ phase shifts. This discussion does not apply to the R-matrix calculation of Ref. [12], because in this case an overall normalization can be absorbed in the fitted constants, reaching the correct order of magnitude for the branching ratio. With this approach, only the asymptotic form of the $\alpha + d$ wave function (thus the phase shifts) enters the calculation.

Precise agreement with the experimental data also requires the correct form of the ^{6}He ground-state wave function. Because the level of the cancellation in B_{GT} is very large, small contributions are important. The wave function should be correctly described up to large distances—in Ref. [13], it was required to extend the spatial integral up to 30 fm to achieve convergence. For the same reason, the wave function needs to be "complete", including also weak components. Depending on the description employed, this completion can be achieved by the choice of a sufficiently large configuration basis (as for the microscopic model in Ref. [11]) or by the inclusion of the components with a large hypermomentum (as for the hyperspherical-coordinates model of Ref. [13]). Besides the value of the overall branching ratio, the energy dependence of the transition probability (Fig. 3) constitutes a further constraint. As shown in Ref. [13], the use of a two-body asymptotic form for the ^{6}He wave function (as in Ref. [12] for example), instead of a three-body one, can cause a distortion of the spectrum on the order of 30% (this being the difference in the ratios of the values of dW/dE at 0.5 and 1.0 MeV between the two models). The present experimental results confirm the need of using a ^{6}He ground-state wave function having the correct three-body asymptotic behavior. The position of the maximum of the experimental data and of the theoretical prediction still differ slightly, but a small modification of the potential can lead to a better agreement [13]. However, it would also be desirable to extend the measurement down to lower energies to reduce uncertainties.

The transition probability is very sensitive to the precise location of the nodes in the wave functions (and, for the $\alpha + d$ wave function, to their behavior at different scattering energies). The present measurement can be used as a stringent test of the ^{6}He (halo) wave function only if a consistent description is adopted for all the states

involved. In Ref. [13] an accurate wave function in hyperspherical coordinates is used for ^{6}He, but obtaining the $\alpha + d$ scattering wave function from a potential model allows for a degree of freedom (the potential) that can be used, within certain limits, to fit the transition probability independently from the description of ^{6}He. (We stress again that, in principle, the potential could be fixed by requiring a better fit of the $\alpha + d$ phase shifts). So far, the only fully consistent approach is the parameter-free, microscopic calculation of Ref. [11]. Within this model, both the ^{6}He and ^{6}Li binding energies are reproduced, as well as the $\alpha + d$ phase shifts. However, the total branching ratio is overestimated by a factor of 2 and the shape of the transition probability as a function of the energy is different, being similar in magnitude to the experimental data at 1.5 MeV but about a factor of 3 larger at 0.5 MeV. Improvements can be sought by changing the basis functions, for example by enlarging the range of the intercluster distances in the various configurations (20 fm being the range used in Ref. [11]).

IV. CONCLUSIONS

We measured the weak $\alpha + d$ branch in the β decay of the halo nucleus ^{6}He by implanting ^{6}He post-accelerated ions in a silicon detector and observing the signal from the emitted particles. The weighted mean of three successive measurements gave a branching ratio $\bar{B} = (1.65 \pm 0.10) \times 10^{-6}$, corresponding to a transition probability $W = (1.42 \pm 0.09) \times 10^{-6}$ s^{-1} for a deuteron energy $E_d \geq 350$ keV. The sum energy spectrum of the emitted ions was also measured. Our results are in agreement with the most recent experimental results from Ref. [6] and are about a factor of 5 smaller than those reported in Ref. [5]. The precision of the branching ratio is significantly improved in the present measurement. Existing calculations [9–11, 13] show that the quenching of the branching ratio is due to a cancellation in the Gamow-Teller matrix element between contributions from different parts of the spatial integral. To achieve such a large quenching and reproduce the correct energy dependence of the transition probability dW/dE, precise requirements are placed on the initial ^{6}He and final $\alpha + d$ wave functions. In particular, the former needs to be specified up to very large distances (about 30 fm) and to possess the correct three-body asymptotic form. To reduce the uncertainties in the models, future measurements should aim at extending the $\alpha + d$ spectrum to even lower energies.

Acknowledgments

We thank L. Buchmann and P. Descouvemont for providing the data from Ref. [6] and [13], respectively, in tabular form. R.R. acknowledges postdoctoral research support from the Fund for Scientific Research-Flanders (Belgium) (F.W.O.-Vlaanderen). This work was supported by the Interuniversity Attraction Poles Programme - Belgian

Science Policy (IUAP) under project P5/07.

[1] P. G. Hansen, A. S. Jensen, and B. Jonson, Annu. Rev. Nucl. Part. Sci. **45**, 591 (1995).
[2] M. J. G. Borge *et al.*, Z. Phys. A **340**, 255 (1991).
[3] I. Mukha *et al.*, Phys. Lett. **B367**, 65 (1996).
[4] K. Riisager *et al.*, Phys. Lett. **B235**, 30 (1990).
[5] M. J. G. Borge, L. Johannsen, B. Jonson, T. Nilsson, G. Nyman, K. Riisager, O. Tengblad, K. Wilhelmsen Rolander (ISOLDE Collaboration), Nucl. Phys. **A560**, 664 (1993).
[6] D. Anthony, L. Buchmann, P. Bergbusch, J. M. D'Auria, M. Dombsky, U. Giesen, K. P. Jackson, J. D. King, J. Powell, and F. C. Barker, Phys. Rev. C **65**, 034310 (2002).
[7] P. Descouvemont and C. Leclercq-Willain, J. Phys. G **18**, L99 (1992).
[8] M. V. Zhukov, B. V. Danilin, L. V. Grigorenko, and N. B. Shul'gina, Phys. Rev. C **47**, 2937 (1993).
[9] D. Baye, Y. Suzuki, and P. Descouvemont, Prog. Theor. Phys. **91**, 271 (1994).
[10] K. Varga, Y. Suzuki, and Y. Ohbayasi, Phys. Rev. C **50**, 189 (1994).
[11] A. Csótó and D. Baye, Phys. Rev. C **49**, 818 (1994).
[12] F. C. Barker, Phys. Lett. **B322**, 17 (1994).
[13] E. M. Tursunov, D. Baye, and P. Descouvemont, Phys. Rev. C **73**, 014303 (2006); **74**, 069904(E) (2006).
[14] P. Descouvemont, C. Daniel, and D. Baye, Phys. Rev. C **67**, 044309 (2003).
[15] D. Smirnov *et al.*, Nucl. Instrum. Methods Phys. Res. A **547**, 480 (2005).
[16] G. Ryckewaert, J. M. Colson, M. Gaelens, M. Loiselet, and N. Postiau, Nucl. Phys. **A701**, 323c (2002).
[17] D. R. Tilley, C. M. Cheves, J. L. Godwin, G. M. Hale, H. M. Hofmann, J. H. Kelley, C. G. Sheu, and H. R. Weller, Nucl. Phys. **A708**, 3 (2002).
[18] D. Miljanic *et al.*, Nucl. Instrum. Methods Phys. Res. A **477**, 544 (2000).
[19] J. F. Ziegler, J. P. Biersack, and U. Littmark, *The Stopping and Range of Ions in Solids* (Pergamon Press, New York, 1985).
[20] J. Büscher, J. Ponsaers, R. Raabe, M. Huyse, P. Van Duppen, F. Aksouh, D. Smirnov, H. O. U. Fynbo, S. Hyldegaard, and C. A. Diget, Nucl. Instrum. Methods Phys. Res. B **266**, 4652 (2008).
[21] R. Raabe *et al.*, Phys. Rev. Lett. **101**, 212501 (2008).
[22] D. R. Tilley, H. R. Weller, C. M. Cheves, and R. M. Chasteler, Nucl. Phys. **A595**, 1 (1995).

Chapter 4

Charged-particle emission in the β decay of the one-neutron halo nucleus ^{11}Be

The one-neutron halo nucleus ^{11}Be has already been introduced briefly in Chapter 1. In this chapter a study of the delayed charged-particle (^{7}Li+ α) emission in the β decay of this nucleus is presented based on two experiments. In one of the experiments the ^{11}Be isotopes were produced in the β decay of ^{11}Li, the Borromean two-neutron halo nucleus that was also introduced in Chapter 1. The decay channels to bound states in ^{11}Be contain valuable halo structure information of the ^{11}Li mother nucleus. By performing an appropiate analysis of the ^{7}Li + α energy spectrum in the ^{11}Be β decay, final states in the daughter nucleus ^{11}B can be identified and their structure can be investigated. Finally, by observing the pattern of the β-strength distribution in the ^{11}Be decay, the effect of its halo can be discussed.

4.1 Current knowledge of the β decay of ^{11}Be

One of the best studied one-neutron halo nuclei is ^{11}Be ($Z = 4$, $N = 7$). The parity of its ground state ($J^{\pi} = \frac{1}{2}^{+}$) is even whereas odd would have been most simply expected from the ordering of the levels in the independent particle shell model. This is shown in Figure 4.1 where the nuclear orbitals for neutrons and protons are presented as a function of energy. Two protons and two neutrons fill the full 1s-shell. The other two protons can be placed in the lower proton $1p_{3/2}$ orbital of the 1p-shell. Four neutrons fill the neutron $1p_{3/2}$ orbital and the last single neutron will occupy the $1p_{1/2}$ orbital in this classical filling of

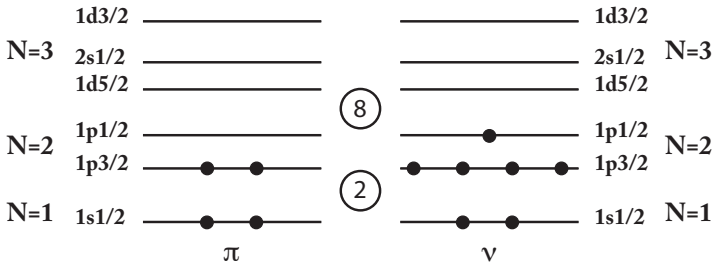

Figure 4.1: Shell model states for protons (π) and neutrons (ν) as a function of energy as deduced from a harmonic oscillator potential with addition of an l^2- and a spin-orbit term. The orbitals are specified by the shell number N, the angular momentum l (l = 0, 1 and 2 for s, p and d), and spin $j = l \pm 1/2$. One orbital can contain at maximum $2j + 1$ nucleons of the same type. Note the large energy gaps at 2 and 8, indicating the extra stability for nuclei with closed shell configurations.

the nuclear orbitals. The combination of the filled 1s-shells, the even number of protons and odd number of neutrons in the 1p-shells, give rise to a negative parity of the ^{11}Be ground state in this framework.

The positive parity assignment for the ^{11}Be ground state is based on a series of experimental results from ^{11}Be β-decay studies [75] in combination with observations of γ transitions in ^{11}B [76] and from measurements [77] of the muon capture in ^{11}B. The spin assignment was fixed to $J = \frac{1}{2}$ following the $l = 0$ stripping pattern observed in the ^{10}Be(d,p)^{11}Be reaction [78]. The anomalous ground state was predicted already in 1960 from the systematics of the lowering of the $2s_{1/2}$ state with respect to the $1p_{1/2}$ level in the $N = 7$ isotones [79]. When residual two-body interactions are taken into account the competition between the $2s_{1/2}$ neutron level and the $1p_{1/2}$ level was shown to be more favorable to the former as more $1p_{3/2}$ protons are removed while moving from ^{13}C($Z = 6$, $N = 7$) through ^{12}B($Z = 5$, $N = 7$) to ^{11}Be. The ordering of levels can also be understood in terms of a strong prolate deformation of ^{11}Be by looking at the Nilsson diagram ([80] p.221), see Figure 4.2. The signature of the $1p_{1/2}$ level is found in the first excited $J^\pi = \frac{1}{2}^-$ state of ^{11}Be at 320 keV which is the only bound excited state in this nucleus due to the small binding energy (S_n = 501.25(58) keV [33], see Figure 4.4).

β-decay studies of the ^{11}Be nucleus have started [75] only one year after the discovery of this radioisotope [81]. The β^- decay of this nucleus has a half life of 13.81(8) s [82] and is characterised by a large Q_{β^-}-value of 11.506(6) MeV [83]. In the first measurement [75] four β branches were observed, including the two

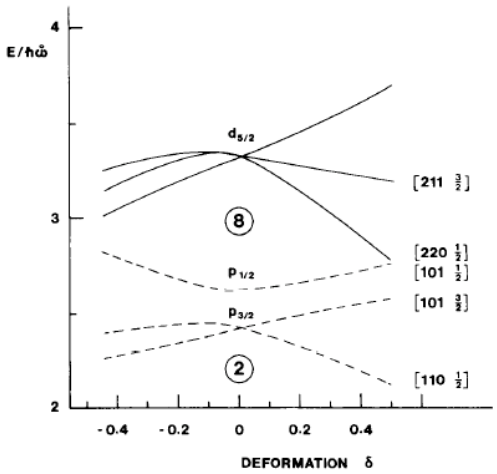

Figure 4.2: Spectrum of single-particle orbits in a spheroidal potential. The orbits are labelled by the asymptotic quantum numbers $[Nn_3\Lambda\Omega]$ referring to large prolate deformations. Levels with even and odd parity are drawn with solid and dashed lines, respectively. The ^{11}Be ground state corresponds between $[101\frac{1}{2}]$ and $[220\frac{1}{2}]$. The figure is taken from [80] p.221

largest first-forbidden transitions to the $J^\pi = \frac{3}{2}^-$ ^{11}B ground state and the $J^\pi = \frac{1}{2}^-$ first excited state, presently known to be at 2125 keV (2124.693(27) keV [84]). Five γ rays were observed with a NaI(Tl) detector both in singles and in coincidence with β particles that were measured with a plastic scintillator. By comparing the single β with the γ-β coincidence spectra an absolute intensity of 33(3)% for the 2125 keV γ line in the β decay of ^{11}Be was derived.

In the second experiment [85] eight γ transitions in ^{11}B were observed following the β decay of ^{11}Be formed in the ^{9}Be(t,p)^{11}Be reaction. The first experimental proof for the charged-particle emission in the decay was found by placing the irradiated target in front of a series of Si detectors with different thicknesses. Above a β-particle contribution at low energies (the cut-off energy was dependent on detector thickness) a continuous α spectrum was observed. This particle emission channel is open when states in ^{11}B are fed at energies above the ^{7}Li + α threshold energy of 8.665(4) MeV [83]. So the available energy for the β-delayed α emission is Q_α = 2.841(7) MeV. If energetically permitted the emission can proceed via the ^{7}Li ground state ($J^\pi = \frac{3}{2}^-$) or its narrow first excited state at 478 keV ($J^\pi = \frac{1}{2}^-$) (477.612(3) keV [84]). The total α activity was calculated by extrapolating the α spectrum at high energies towards the lower energy region. A separate measurement of the γ-ray

spectrum was made and care was taken to obtain the same integrated beam current in both observations. By comparing the known intensity (33(3)% [75]) of the 2125 keV γ-ray with the measured α yield they obtained an intensity of 3.0(7)% for the α-particle emission per ^{11}Be decay. Because of the possible feeding of the ^{7}Li first excited state, α-γ coincidence measurements were performed with Si and NaI(Tl) detectors. Taking only events above a threshold of 0.3 MeV (just above the β cut-off energy) an upper limit of 5% was placed on the number of α particles that were accompanied by 478 keV γ rays. In the analysis of the α spectrum several states in ^{11}B above the ^{7}Li + α threshold were considered. These were taken from reaction experiments ^{7}Li(α,α)^{7}Li, ^{7}Li(α,α')^{7}Li*(478 keV) [86] and ^{7}Li(α,γ) [87] : states at 9870 keV ($J^{\pi} = \frac{3}{2}^{+}$), 10250 keV (preferred $J^{\pi} = \frac{3}{2}^{-}$) and 10380 keV ($J^{\pi} = \frac{1}{2}^{+}$). The first two states are presently known at respective energies of 9.876(8) MeV and 10.260(15) MeV [84] and are shown in Figure 4.3. The latter state was anticipated by [86] but not confirmed by [87] and presently not tabulated [84]. So there was no unique establishment of the states at these excitation energies in ^{11}B. The analysis was also complicated by several factors. For example, in the case of the ^{9}Be(t,p)^{11}Be reaction, the ^{11}Be was stopped in the tantalum backing of the ^{9}Be target foil. This leads to a significant energy loss of the escaping α particles and thus one also has to consider the depth distribution of the ^{11}Be within the Ta. Due to the experimental difficulties in this experiment it was proposed that only the 9.876 MeV state was responsible for the α particles observed but no firm conclusions could be made and upper limits on the other two contributions were given.

The search for charged-particle emission in the ^{11}Be β decay was reprised almost ten years later [88]. In this reinvestigation the formed activity in the ^{9}Be(t,p)^{11}Be reaction was transported by a helium-jet system and the radiation was measured with Si and NaI(Tl) detectors on opposite sides of an implantation tape. The α-energy spectra were obtained both in singles as well as in coincidence with 478 keV γ rays. Those spectra clearly suffer from noise and a β-particles contribution at lower energies. No accurate energies of the observed α and ^{7}Li particles were given. From the α-energy spectrum in coincidence with 478 keV γ rays and the observed γ's in coincidence with heavy particles from the decay, a weighted average of (12.6 ± 1.2)% was obtained for the relative α-particle branching ratio to the first excited state of ^{7}Li and thus (87.4 $\pm$ 1.2)% to the ^{7}Li ground state [88]. The authors argued these values not being in contradiction with the previous upper limit of 5% for the relative branching ratio to the ^{7}Li* + α channel (described above) because of the experimental difficulties encountered in that measurement [85]. The total α yield was compared with a simultaneous measurement of the 2125 keV γ line. Using the known intensity of the latter [75] a β branching of 2.9(4)% to the state at 9.876 MeV in ^{11}B was calculated. From the α-energy spectrum the authors

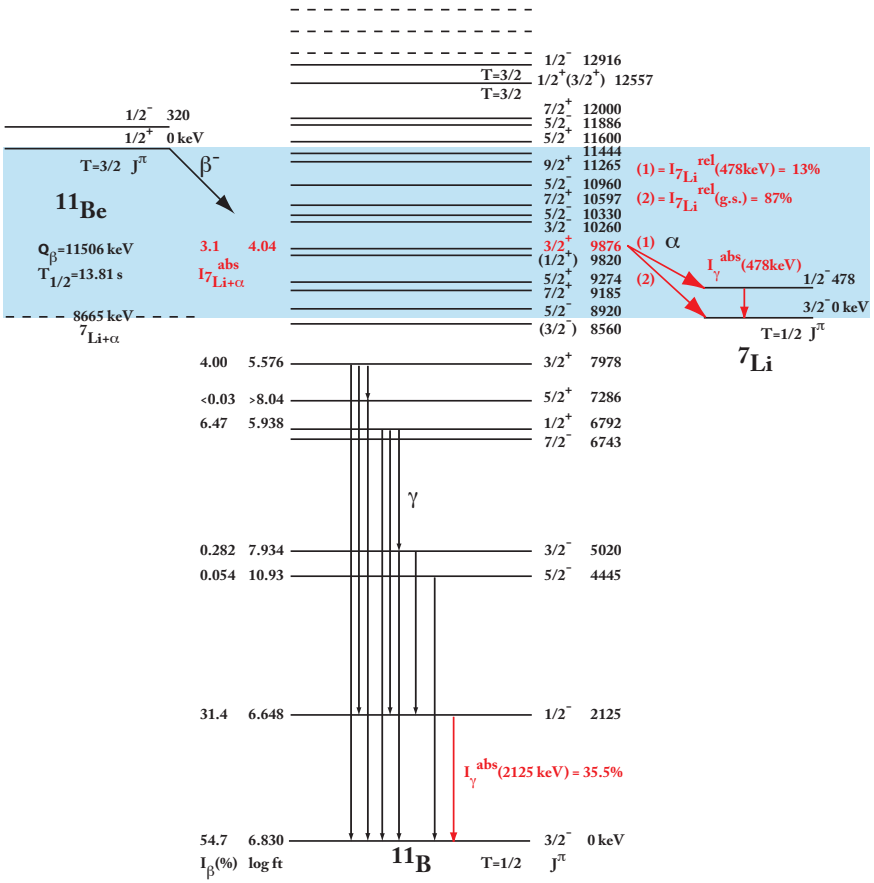

Figure 4.3: This scheme summarizes the present knowledge of ^{11}Be β decay. Mass input (Q-values) and level energies are taken from [83] and [84], respectively. More info is given in the text.

excluded the significant involvement of any state of ^{11}B above the 9.876 MeV state.

In 1982 the β decay of ^{11}Be was revised for the last time [89]. γ singles, γ-γ coincidences, β singles and β-γ coincidences were studied in this decay. A branching ratio for the unique first-forbidden β transition to the 4445 keV ($J^\pi = \frac{5}{2}^-$) state (4444.89(50) keV [84]) was obtained and the intensity of the 2125 keV γ ray in the decay was remeasured to be $(37.0 \pm 2.5)\%$. Together with the old value of [75] this gives an adopted value of $(35.5 \pm 1.8)\%$. Hence, all the β branches were renormalized. The branching ratio to the state at 9.876 MeV was re-evaluated to be 3.1(4)%.

All the information gathered from previous experiments on the β decay of ^{11}Be is summarized in the decay scheme that is presented in Figure 4.3. In the first place we were looking in our experiment, described in the next sections, for a precise determination of the α branching in the β decay of ^{11}Be, trying to improve on the branching ratio value and the energy spectrum of the emitted α and ^{7}Li ions. The energy region of interest for this study is indicated as a blue "window". The numbers and transitions indicated in red in Figure 4.3 are important in the discussions that will appear in the next sections and their values are taken from [89].

4.2 Experimental setup

The β decay of ^{11}Be was investigated during a campaign, focusing on the ^{11}Li nucleus [45], which took place at the Isotope Separator and ACcelerator(ISAC) facility [90] at TRIUMF (Vancouver, Canada). The ^{11}Be nuclei were obtained from the β decay of the ^{11}Li ions produced at ISAC and implanted in a silicon strip detector as described in Chapter 2. The Isotope Separation On-Line (ISOL) technique [91] was employed to produce the beam of ^{11}Li ions: A thick (20 g/cm^2) Ta target was bombarded by the 500 MeV, 35 μA proton beam from the TRIUMF Cyclotron; reaction products were ionized by surface ionization, ^{11}Li was selected by a magnetic analyzer and post-accelerated. A stripping foil was used to increase the charge state of the ions, a method that avoided delays in the post-acceleration process. The ^{11}Li ions were brought to an energy of 1.5 MeV/nucleon, the maximum allowed by the ISAC-1 accelerator, corresponding to a total energy of 16.5 MeV.

The ^{11}Be isotopes were produced in the decay of the implanted ^{11}Li. The decay of ^{11}Li ($T_{1/2} = 8.5(2)$ ms [84]) is complex, with channels leading to several unstable daughter nuclei due to a large Q-value of 20.551(1) MeV [33, 34] and low particle break-up thresholds in the ^{11}Be daughter nucleus. The decay scheme is presented in Figure 4.4. A summary showing the branching ratios and daughter half lives is given in Table 4.1.
The branching to the ^{11}Be ground state is found to be negligible and an upper

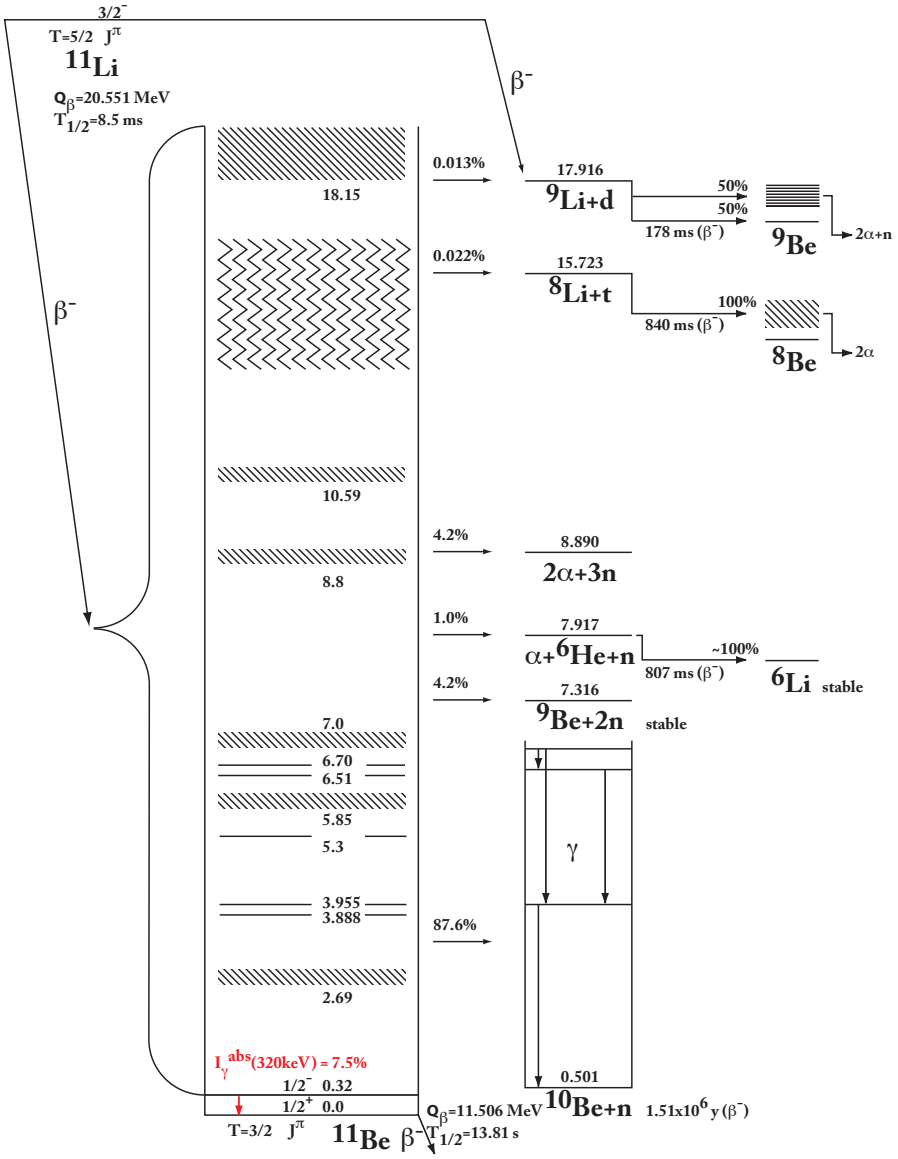

Figure 4.4: Decay scheme of ^{11}Li based on Figure 1 of [92]. Level energies, in MeV and relative to the ^{11}Be ground state, and half lives are taken from [84]. Q-values and masses come from [83].

Table 4.1: β-decay channels of ^{11}Li and half lives of its unstable daughters (the decay of neutrons is ignored since they escape our detection setup).

Branching ratio and decay channel				Daughter half life
(a)	7.5% [1]		$^{11}\mathrm{Be} + \gamma$	13.81 s
(b)	87.6%	[93]	$^{10}\mathrm{Be} + n$	10^6 y
(c)	4.2%	[93]	$^{9}\mathrm{Be} + 2n$	stable
(d)	1.0%	[37]	$^{6}\mathrm{He} + \alpha + n$	807 ms
(e)	1.9%	[93]	$2\alpha + 3n$	stable
(f)	0.022%[2]		$^{8}\mathrm{Li} + t$	840 ms
(g)	0.013%	[45]	$^{9}\mathrm{Li} + d$	178 ms

[1] Weighted average of the values presented in Table 4.2

[2] Not yet published, from the analysis of the ^{11}Li decay data measured in this campaign. Analysis technique described in [45].

Table 4.2: Experimental values for the branching ratio (BR) to first excited state of ^{11}Be in the β decay of ^{11}Li

Ref.	BR
[94]	$(5.2 \pm 1.4)\%$
[95]	$(9.2 \pm 0.7)\%$
[93]	$(6.3 \pm 0.6)\%$
[96]	$(7.8 \pm 0.8)\%$
[97]	$(7.6 \pm 0.8)\%$

limit of 2% was placed on this branch [95]. Hence, the ^{11}Be nuclei are mainly produced in the branch (a) (see Table 4.1) to its first excited state at 320 keV. This transition has been observed in several measurements of the β decay of ^{11}Li using different experimental techniques. An overview is given in Table 4.2. The first measurement [94] in Table 4.2 used the (33 ± 3)% intensity of the 2125 keV γ-ray transitions in ^{11}B from [75] whereas in [93] the revised value (35.5 ± 1.8)% [89] was taken into the calculation. The weighted average for the branching ratio to the ^{11}Be first excited state in the β decay of ^{11}Li can be calculated from the values in Table 4.2: I_γ^{abs}(320 keV) = (7.5 ± 0.3)%. This value does not change if the result from [94] is corrected for the revised value for the 2125 keV γ-ray intensity. The result is shown in Figure 4.4 in red because it is an important factor in the calculation of the branching ratio of the ^{7}Li + α emission channel in the β decay of ^{11}Be, the focus of this study.

In order to select and observe the decay of the ^{11}Li daughter nuclei, the implantation of ^{11}Li in a thin double-sided silicon strip detector (DSSSD, described in Chapter 2) was modulated with a period of 20 s beam on - 20 s beam off. About 11.6×10^6 ^{11}Li ions were implanted in the beam on period at a rate of ≈ 230 ions/sec. In the beam off period, the activity of other daughters decays rapidly, and eventually becomes negligible with respect to the ^{11}Be decay signal. Among the channels listed in Table 4.1, in fact, only channel (f) is relevant with respect to the study of the ^{7}Li + α branch in the ^{11}Be decay, because the decay of the ^{8}Li daughter proceeds entirely via the emission of two α particles with a broad spectrum extending up to ≈ 15 MeV; in channel (d), ^{6}He decays by pure β emission (to the 10^{-6} level [98, 99], see Paper II presented in Chapter 3); channel (g) is also negligible due to the combination of the smaller branching ratio, the short half life of the daughter ^{9}Li, and the partial branching ratio for the emission of α particles in the daughter decay [95].

To ensure a uniform distribution on the detector surface, the beam was defocused using electric quadrupole lenses. In Figure 4.5 the implantation (beam on) (a) and decay (beam off) (b) profiles are shown in the pixel matrix defined by the strips on the front and the back side. Strips 81 and 82 were taken out of the analysis because for these strips during the experiment there was a disconnection between the preamplifier and the shaper module. From the energy of the ^{11}Li beam, the implantation depth was calculated to be 43 μm, with a straggling (FWHM of the depth distribution) smaller than 2 μm, using the SRIM program (Stopping and Range of Ions in Matters [59]). Because of the very low recoil energy (less than 1 keV) the ^{11}Be produced in the β decay remain in the same position, close to the middle plane of the detector. The available energy for the ^{7}Li + α emission channel in the β decay of ^{11}Be was calculated in section 4.1 to be Q_α = 2.841(7) MeV. Due to kinematics the maximum energy of the emitted α particle equals 7/11 of this energy, that is

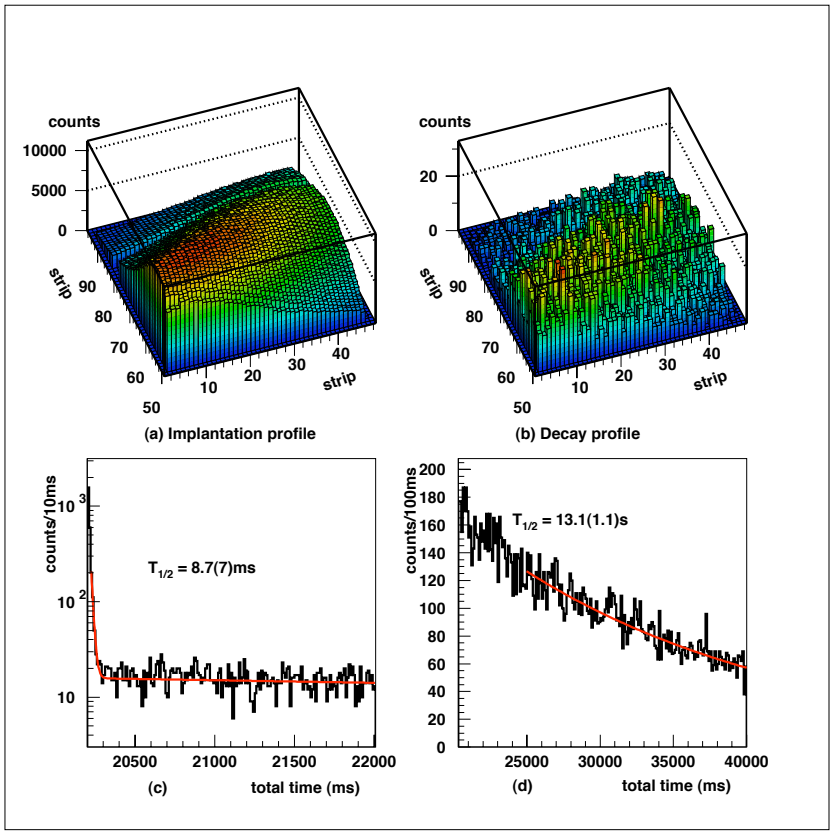

Figure 4.5: (a) Beam distribution on the pixel matrix during the beam on period. The events that are shown have energies around 16.5 MeV. (b) Distribution of events during the beam off period. (c) The first part of the beam off period is fitted with two exponential functions. The beam off period start at 20220 ms. The presented result gives the half life for the short-living component. (d) A time fit on the decay spectrum after 5 seconds in the beam off period with a single exponential function is presented.

about 1.8 MeV. This corresponds to a range of less than 6.5 μm [59]. Clearly, all ion emissions are confined within the pixel where they originated (see Chapter 2, [43, 44]).
As explained in Chapter 2 the analysis is performed on events that correspond to two firing strips, one on each side of the detector. We want to recall the method used in case of a parent nucleus implanted in a zone corresponding to an inter-strip section on one of the faces, as discussed in [44]. The charge generated by the ions is shared between two strips: for implantation events, both strips will give a signal, while for decay events it may happen that the signal in one strip is below threshold (in the case of ^{11}Be, the charge generated in a decay is always sufficient to generate a trigger in at least one of the strips). To correct, events with signal in two neighboring strips are reconstructed by summing the two energies, and assigned to the pixel with the highest energy. The procedure is only applied for energies above the β background (500 keV).

The detector was calibrated using a standard three-peak α source and a ^{148}Gd source, at regular intervals during the measurement. Particular care was devoted to reduce the electronic noise. The detection threshold was set below 200 keV for most of the strips; the value of 200 keV was used in the offline data analysis. The trigger efficiency at this energy, measured using pulser signals [44], was 75%, rapidly increasing to 100% at 300 keV.

4.3 Results

To verify that the implanted activity belongs to ^{11}Li the time behavior of events in the beam off period is investigated. In Figure 4.5 (c) the time profile of events coming in the first 10 seconds of the beam off period is fitted with the sum of two exponential functions, one corresponding to the longer-living daughter activity and the other to the first decay events. The actual beam off period starts at 20220 ms. The result for the short living component gives a half life $T_{1/2} = 8.7(7)$ ms indicating that the implanted activity corresponds to ^{11}Li ($T^{\text{lit}}_{1/2} = 8.5(2)$ ms [84]). When during the same experimental campaign a continuous ^{11}Li beam was implanted to study the $^{9}\text{Li} + d$ and $^{8}\text{Li} + t$ channels in the β decay of ^{11}Li, a fit on the time profile of events coming within 40 ms after an implantation in the same pixel gives a similar value of 8.7(1) ms [45]. After waiting 5 seconds in the beam off period most of the ^{11}Li daughter activity has decayed except for the produced ^{11}Be. This can be checked by a fit on the time interval [25000 ms, 40000 ms], where 40000 ms refers to the end of the beam off period. This gives a value of $T_{1/2} = 13.1 \pm 1.1$ s and the result is shown in Figure 4.5 (d). This confirms the assignment of events in this time window to the ^{11}Be β decay ($T^{\text{lit}}_{1/2} = 13.81(8)$s [84]).

The α branching in the β decay of ^{11}Be can be studied in the energy spectrum

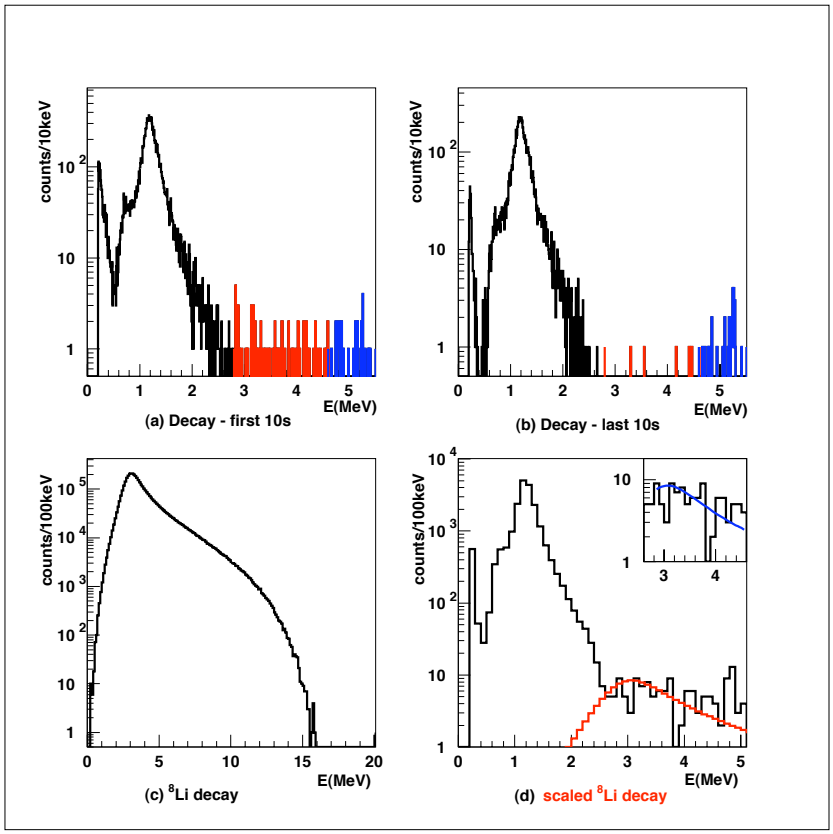

Figure 4.6: (a) Energy decay spectrum taken in the first 10 seconds of the beam off period. In the energy interval between 2.8 MeV and 4.5 MeV ^{8}Li decay events are seen and around 5 MeV there is a constant α background. (b) Decay spectrum taken in the last 10 seconds of the beam off period. Same comments as in (a). (c) Decay spectrum of ^{8}Li, recorded in the 2.5 s beam off period after 2.5 s of ^{8}Li implantation. (d) Full energy decay spectrum presented together with a scaled ^{8}Li decay spectrum resulting from a scaling in the energy interval 2.8 MeV - 4.5 MeV shown in the inset as explained in the text.

of events in the implantation detector recorded in the beam off interval. In such a spectrum the number of events are plotted versus the average energy recorded in the two strips that define the pixel where the event took place. This is done with a condition on the energy difference between the two strip energies in order to reduce the contribution of β particles [43, 44]. In this case the constraint $|E_p - E_n| < 200$ keV was applied. In Figure 4.6 the energy spectra are presented for two time intervals in the beam off period: (a) [20220 ms, 30000 ms] and (b) [30000 ms, 40000 ms] . At low energies β particles are the main contribution with a cut-off at about 400 keV. They mainly correspond to the feeding of states in ^{11}B below the lowest particle threshold of 8.665 MeV for the ^{7}Li + α channel. In the energy interval between this cut-off energy and the Q-value of the α branching in the ^{11}Be β decay of 2.841 MeV, the signature of the delayed α emission can be searched for, as indicated in Figure 4.3.

One can clearly observe in the first part of the beam off interval events in the energy interval between 2.8 MeV and 4.5 MeV (artificially colored red) whereas this activity is negligible in the last part. Since the energy spectrum for events originating from the β decay of ^{11}Be has an endpoint of about 2.8 MeV, these events must belong to some other ^{11}Li daughter activity. Following the discussion given above, the events are assigned to ^{8}Li decay events. ^{8}Li decays mainly to a broad 2^+ state around 3 MeV in ^{8}Be which breaks up into two α particles. The activity indicated in blue in Figure 4.6 (a) and (b) around 5 MeV can be assigned to α activity built up in the detection chamber during earlier experiments and is constant in time.

4.3.1 The ^{8}Li + t channel in the ^{11}Li β decay

To study the α branching in the β decay of ^{11}Be, a clean energy spectrum in the beam off period is needed. As discussed above Figure 4.6 showed that in the first part of the decay period, the α particles from the ^{8}Li β decay have a non-negligible contribution. This gives another possibility to investigate the ^{8}Li+ t channel in the ^{11}Li decay in addition to the correlation method described in [45]. Therefore, one needs to know the detector response to the decay of ^{8}Li. The respons was obtained by implanting a ^{8}Li beam in a modulation of 2.5 s beam on-2.5 s beam off. An energy decay spectrum for the two emitted α particles is again collected in the beam off period and the result is presented in Figure 4.6(c). The part of this ^{8}Li decay spectrum in the region between 2.8 MeV and 4.5 MeV, above the Q-value for α branching in ^{11}Be decay and below the constant α background, can be scaled to give the best agreement with the decay spectrum from the 20 s on-20 s off ^{11}Li beam modulation in the same energy interval. This is shown in the inset of Figure 4.6 (d). The ^{8}Li decay spectrum is then scaled correspondingly (red spectrum) and plotted together with the full decay spectrum in Figure 4.6(d). The result gives the

total contribution of the ^{8}Li decay in the beam off period. Since the number of implantations is accurately measured by counting the events with energies of $\approx$ 16.5 MeV, the branching ratio for the ^{8}Li+ t channel can be calculated. The number of ^{8}Li decay events are counted in the 2.8 MeV - 4.5 MeV energy interval in the scaled total ^{8}Li decay spectrum presented in Figure 4.6(d). The calculation takes into account the acquisition deadtime in the beam on and beam off periods, the half life of ^{8}Li in combination with the specific beam modulation and the fraction of the ^{8}Li decays in the 2.8 MeV - 4.5 MeV energy interval over the total integral. A value of $2.59(27)\times10^{-4}$ is obtained in agreement with the preliminary result from the calculation described in [45] given in Table 4.1.

4.3.2 α emission in the ^{11}Be β decay

After waiting 5 seconds in the beam off period the contribution of ^{8}Li decays in the energy region below 2.8 MeV is reduced to the level of 0.02% of the total number of expected ^{8}Li decays in the full energy region. This number takes into account the energy profile of the ^{8}Li decay spectrum, the ^{8}Li half life and the 20 s on-20 s off beam modulation. Given the total number of ^{11}Li implantations and the branching ratio for the ^{8}Li + t channel calculated in the previous section, only 1 event (0.66) is expected to contribute below 2.8 MeV. One can conclude that the decay spectrum obtained after waiting 5 seconds in the beam off period is a pure ^{11}Be decay spectrum. In this spectrum the integral is taken between 400 keV, above the β cut-off energy, and 2.8 MeV. The total ^{7}Li + α branching in the ^{11}Li β decay via bound states of ^{11}Be is then calculated to be BR(^{11}Li $\rightarrow$ ^{11}Be(bound)) $\times$ BR(^{11}Be $\rightarrow$ ^{7}Li + α) = (3.69 $\pm$ 0.03)$\times10^{-3}$. This value again contains corrections for acquisition deadtime and the time observation window taking into acount the ^{11}Be half life. If one assumes there is no branching to the ^{11}Be ground state in the β decay of ^{11}Li (an upper limit of 2% was placed in [95]) the result can be rewritten following the convention used in Figures 4.3 and 4.4:

$$I_{\gamma}^{abs}(320\text{ keV}) \times I_{^{7}\text{Li}+\alpha}^{abs} = (3.69 \pm 0.03) \times 10^{-3}. \quad (4.1)$$

The value I_{γ}^{abs}(320 keV) corresponds to the feeding of the first excited ^{11}Be state in the β decay of ^{11}Li. Different results for this branching ratio are given in Table 4.2 with a resulting weighted average, I_{γ}^{abs}(320 keV) = (7.5 $\pm$ 0.3)%. If this value is used in equation (4.1) the branching ratio for α emission in the β decay of ^{11}Be is calculated to be $I_{^{7}\text{Li}+\alpha}^{abs}$ = (4.9 $\pm$ 0.2)%. This result is in disagreement with the present value of (3.1 $\pm$ 0.4)% [89] by a factor 1.6 .
The values in Table 4.2 were calculated using different intensities of the ^{11}B 2125 keV γ ray in the β decay of ^{11}Be. It is worthwile to set up a procedure

to calculate $I_{\gamma}^{abs}(320\ keV)$ from equation (4.1) that does not require the direct knowledge of $I_{^7Li+\alpha}^{abs}$.
In equation (4.1) it is known that

$$I_{^7Li+\alpha}^{abs} = I_{^7Li}^{abs}(g.s.) + I_{^7Li}^{abs}(478\ keV) = I_{^7Li}^{abs}(478\ keV) \times (1 + \frac{I_{^7Li}^{abs}(g.s.)}{I_{^7Li}^{abs}(478\ keV)}). \quad (4.2)$$

It is clear that $I_{^7Li}^{abs}(478\ keV) = I_{\gamma}^{abs}(478\ keV)$ and :

$$I_{\gamma}^{abs}(478\ keV) = \frac{I_{\gamma}^{rel}(478\ keV)}{I_{\gamma}^{rel}(2125\ keV)} \times I_{\gamma}^{abs}(2125\ keV). \quad (4.3)$$

By combining all these three equations the final formula is derived:

$$I_{\gamma}^{abs}(320\ keV) \times \frac{I_{\gamma}^{rel}(478\ keV)}{I_{\gamma}^{rel}(2125\ keV)} \times$$

$$(1 + \frac{I_{^7Li}^{abs}(g.s.)}{I_{^7Li}^{abs}(478\ keV)}) \times I_{\gamma}^{abs}(2125\ keV) = (3.69 \pm 0.03) \times 10^{-3} \quad (4.4)$$

The γ-intensity ratio $\frac{I_{\gamma}^{rel}(478\ keV)}{I_{\gamma}^{rel}(2125\ keV)}$ has been measured in ^{11}Li β-decay experiments [100, 101] and [102, 103] to be 0.0069(7) [104] and 0.0063(7) [105], respectively, giving an average value of 0.0066(5). As mentioned before, the relative feedings of the ^{7}Li(g.s.) + α ($I_{^7Li}^{rel}$(g.s.)) and ^{7}Li(478 keV) + α ($I_{^7Li}^{rel}$(478 keV)) channels in the ^{11}Be β decay were calculated in [88] to be (87.4 ± 1.2)% and (12.6 ± 1.2)%, respectively. If we take the absolute γ intensity for the 2125 keV line in the ^{11}Be β decay from [89], $I_{\gamma}^{abs}(2125\ keV)$ = (35.5 ± 1.8)%, and use the fact that $\frac{I_{^7Li}^{abs}(g.s.)}{I_{^7Li}^{abs}(478\ keV)} = \frac{I_{^7Li}^{rel}(g.s.)}{I_{^7Li}^{rel}(478\ keV)}$, a value of (20 ± 3)% is obtained for $I_{\gamma}^{abs}(320\ keV)$ from equation (4.4). This result disagrees with the average value from literature, (7.5 ± 0.3)%, by almost a factor 3. The only factor in equation (4.4) that can be derived from the implantation experiment performed at TRIUMF, other than the total ^{7}Li + α branching ratio, is the ratio $\frac{I_{^7Li}^{rel}(g.s.)}{I_{^7Li}^{rel}(478\ keV)}$. The goal is to redefine this ratio as precisely as possible by applying an appropiate fit on the decay energy spectrum, in order to be able to check on the present discrepancy for $I_{\gamma}^{abs}(320\ keV)$.

The pure ^{11}Be decay spectrum, taken after 5 seconds in the beam off period for reasons given above, is presented in black in Figure 4.7. All events in the spectrum above the pure β cut-off around 400 keV correspond to the charged-particle emission in the ^{11}Be β decay. At first sight there are mainly two contributions, one big peak around 1.2 MeV and a smaller one around 700 keV. These contributions correspond respectively to the summed ^{7}Li + α

energy from the feeding of the ^{7}Li ground state and first excited state coming from the excited state in ^{11}B around 9.876 MeV as shown in Figure 4.3. In order to come to a full understanding of the decay spectrum, the R-matrix formalism is applied. This framework has originally been developed for nuclear reaction studies but it can also be applied in β-decay studies [106–108] (see Appendix A). In the following sections the relative feedings of the ^{7}Li(g.s.) + α and ^{7}Li(478 keV) + α emission channels are further investigated together with the contributions and/or influences of different states in ^{11}B.

One level, two channels approximation

As a first approximation the R-matrix formalism for only one level, the one at 9.876 MeV, and two channels, ^{7}Li(g.s.) + α and ^{7}Li(478 keV) + α, was applied to fit the experimental data. The 9.876 MeV state has a spin-parity assignment $J^{\pi} = \frac{3}{2}^{+}$. Total angular momentum and parity conservation leads to the following possibilities for the relative orbital momentum l in the emission of the α particle:

$$9.88 \text{ MeV}; \frac{3}{2}^{+} \rightarrow {}^{7}\text{Li(g.s.)}; \frac{3}{2}^{-} + \alpha(0^{+}) \qquad l = 1, 3 \tag{4.5}$$

$$9.88 \text{ MeV}; \frac{3}{2}^{+} \rightarrow {}^{7}\text{Li(478 keV)}; \frac{1}{2}^{-} + \alpha(0^{+}) \qquad l = 1. \tag{4.6}$$

Because of the higher centrifugal barrier ($\propto \frac{l(l+1)\hbar^2}{2mr^2}$; m = reduced α mass, r = radial distance to center of potential [109], section 4.5.2) for the $l = 3$ α particle, the decay rate for this channel is reduced and can be neglected with respect to the $l = 1$ α-emission channel (see Appendix A.5.2).
The decay spectrum is fit using equation A.56, presented in Appendix A. With only one ^{11}B level taken into account and two channels, four parameters are used for the fit: one β-strength parameter, $\tilde{g}_{1,GT}$, the resonance energy, $\tilde{E}_1$, and two reduced widths, $\tilde{\gamma}_{1c}$ (c = 1,2). The index $c = 1$ refers to the ^{7}Li(g.s.) + α channel whereas $c = 2$ corresponds to the coupling to the ^{7}Li(478 keV) + α channel. Given the spin-parity of the 9.876 MeV level, there is no allowed Fermi transition and we only have one β-strength parameter, $\tilde{g}_{1,GT}$, corresponding to a Gamow-Teller transition. When broad levels are involved it is hard to define $\log(ft)$ values for transitions to these states, since the phase space factor is energy dependent and hence changing over the width of the level. It is therefore better to start from the matrix element, $M_{\lambda x}$ ($x = F$ or GT), corresponding to the transition. This matrix element can be calculated directly from the fit results using equation A.48 given in Appendix A. With this matrix element we

can calculate $(ft_{1/2})_\lambda$ using the following formula [108]:

$$(ft_{1/2})_\lambda = \frac{K}{M^2_{\lambda F} + M^2_{\lambda GT}} = \frac{K}{B(F) + (\frac{g_A}{g_V})^2 B(GT)}, \tag{4.7}$$

where K = 6146(6) [110], $B(F)$ and $B(GT)$ the reduced Fermi and Gamow-Teller transition probabilities, respectively, and g_V and g_A the weak interaction vector and axial-vector coupling constants, with g_A/g_V = -1.266 as derived from the measurement of the decay of the free neutron [111].

This general procedure will be used for all fits described in this Chapter. When extra, interfering levels are involved it becomes impossible to talk about separate branching ratios to the different states and the only way we can express the strength of the transitions is by calculating the matrix elements and corresponding $\log((ft_{1/2})_\lambda)$ values.

For the normalization of formula A.56 the number of counts, N, in the energy region of interest has to be known as well as the partial half life to this region, $t_{1/2}$. N can be derived directly from the experimental spectrum. In the energy region between 400 keV and 2.8 MeV, where we expect the charged-particle emission events, 12799 ± 113 events (N) were counted. From this experiment though, it is impossible to calculate $t_{1/2}$. Therefore we use for the fits described in this section, the result from a complementary experiment described in section 4.4. The branching ratio to the energy interval [400 keV, 2.8 MeV] in the β decay of ^{11}Be is given by equation (4.8): BR = (3.47 ± 0.12)×10^{-2}. Given the half life of ^{11}Be ($T_{1/2}$ = 13.81(8) s [82]), we can calculate $t_{1/2}$ = (398 ± 14) s.

The parameters that were kept fixed are: the Q-value = 11.506 MeV for the ^{11}Be β decay, the ^{7}Li + α threshold at 8.665 MeV in ^{11}B and the excited state of ^{7}Li at an energy of 478 keV. The channel radius for the α emission is also kept fixed at a value $a_c = r_0(A_1^{1/3} + A_2^{1/3})$, where A_1 = 4 and A_2 = 7 corresponding to the emitted α and ^{7}Li particles, respectively. With r_0 chosen to be 1.42 fm this results in a channel radius of a_c = 4.96 fm which is a typical value for the application of the R-matrix theory. The same channel radius a_c is taken for both decay channels. The effect of β summing explained in Chapter 2 was not included in the definition of the R-matrix framework in our case (see Appendix A). Therefore one can expect the fitted resonance energy, $\tilde{E}_1$, to be larger than the real physical value. The difference between these two values was predicted in section 2.4 to lie around 12 keV.

The first fit is performed in the energy interval [580 keV, 1250 keV] (range (a)). The result is shown in Figure 4.7 (a) and the numerical results are given in Tables 4.3 and 4.4 . At low energies the theoretical fit function shows very good agreement with the experimental data . However there is a clear underestimation of the high-energy tail. Therefore the fit is repeated, this time for a wider energy range [580 keV, 2250 keV] (range (b)). It is clear from this

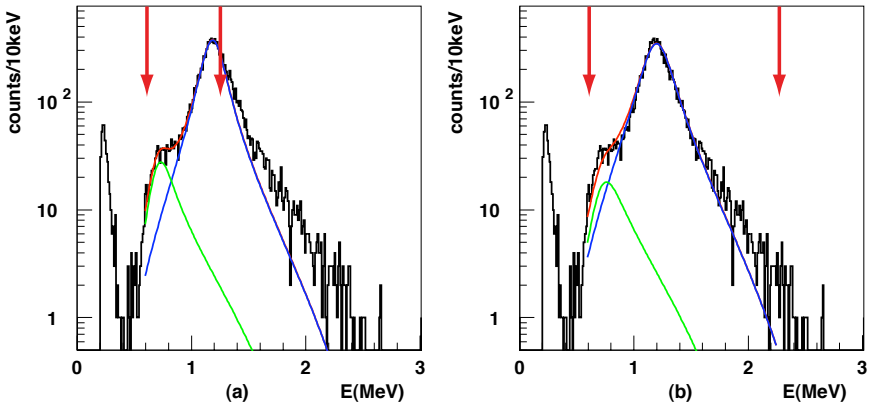

Figure 4.7: The black experimental ^{11}Be β-decay spectrum is fitted in the R-matrix formalism for one state and two channels. In (a) the fit range is [580 keV, 1250 keV] in (b) [580 keV, 2250 keV], both ranges indicated with the red arrows. The contributions of the ^{7}Li(g.s.) + α and ^{7}Li(478 keV) + α channel are shown in blue and green, respectively. The total theoretical curve is shown in red.

Table 4.3: Results from the R-matrix fit using the one level, two channels approximation. The partial widths Γ_{1c} are calculated from the reduced widths $\tilde{\gamma}_{1c}$ using the formula A.58 of Appendix A.5 . The percentage of the total width ($\Gamma_1 = \Gamma_{11} + \Gamma_{12}$) is given between brackets.

Fit range	$\tilde{E}_1$(MeV)	$\tilde{\gamma}_{11}$(MeV$^{1/2}$)	$\tilde{\gamma}_{12}$(MeV$^{1/2}$)	
range (a) [1]	9.892(2)	0.96(3)	0.72(3)	
		Γ_{11}(keV)	Γ_{12}(keV)	Γ_1(keV)
		221(11) (92.5(5)%)	18(1) (7.5(5)%)	239(11)
range (b) [2]	9.930(2)	1.22(5)	0.74(5)	
		Γ_{11}(keV)	Γ_{12}(keV)	Γ_1(keV)
		322(16) (94.2(6)%)	20(2) (5.8(6)%)	342(16)

[1] [580 keV, 1250 keV] ; $\chi^2_{red} = 0.86$

[2] [580 keV, 2250 keV] ; $\chi^2_{red} = 2.74$

Table 4.4: Results from the R-matrix fit using the one level, two channels approximation.

Fit range	$\tilde{g}_{1,GT}$	$M_{1,GT}$	$\log((ft_{1/2})_1)$
range (a)	1.07(4)	0.69(3)	4.12(4)
range (b)	1.37(5)	1.10(7)	3.71(5)

result, shown in Figure 4.7 (b), that the theoretical R-matrix curve tries to reproduce the experimental data at higher energies. However, the price that is paid for this better agreement can clearly be seen at the low-energy tail, where the fit is poorer than in the case of the first fit, Figure 4.7 (a). So, it is likely to think that this fit result is not based on a good physical ground. This can also be concluded from the resulting parameter values listed in Tables 4.3 and 4.4. First of all the reduced χ^2 is much worse than for the first fit. Secondly, the resonance energy, $\tilde{E}_1$, is shifted to a higher value lying 54 keV above the literature value, E = 9.876(8) MeV, for this state. This is a factor 4.5 more than the shift of $\sim$ 12 keV that can be expected from the energy summing of the accompanying β particle as shown by the simulations described in Chapter 2. One can immediately conclude that the result for the first fit, $\tilde{E}_1$ = 9.892(2) MeV is in good agreement in this respective, lying $\sim$ 16 keV above the literature value. A third proof for this 'artificial' solution is found in the partial widths, Γ_{1i} (i = 1,2) for the two channels and the total width, Γ_1. This $\frac{3}{2}^+$ state around 9.88 MeV has been observed in reaction experiments, e.g. [86, 87, 112], and in the measurement of the β decay of ^{11}Be [88]. In the reaction experiments the calculated width of the state ranges from 104 keV to 130 keV whereas in the β-decay experiments indications of a large width of 200 keV were found. So there is no unique assignment for the width of this state but the adopted value in literature is $\Gamma = 110 \pm 15$ keV. The second fit gives a total width that is a factor of 3 larger than this tabulated value. The β feeding of the state, expressed by the $\log((ft_{1/2})_1)$ values listed in Table 4.4, agrees with the literature value 4.04 ± 0.08 [89] for the first fitting range whereas the fit in range (b) predicts a feeding that is about three times larger.

For the two fits the coupling to both channels is expressed in % of the total width of the state in Table 4.3. These values can be compared with the literature values of 87.4% and 12.6% for the feeding of the ^{7}Li ground state and first excited state, respectively [88]. There is a clear discrepancy between these tabulated values and the result of this first approximation using the R-matrix formalism. Despite this poor agreement for the relative feeding of both channels and the width of the state around 9.88 MeV, it is clear that this level in ^{11}B is responsible for the main contribution in the decay spectrum.

So, what is the explanation for the underestimation of the experimental data at higher energies? In Chapter 2 the effect of β summing on the energy spectrum was simulated. It was clear that this generated a shift of the energy spectrum to higher energies and a slight asymmetry for the assumed Lorentzian spectrum. This effect is nevertheless not enough to explain the discrepancy between the data and the fits presented in Figure 4.7.

The energy region of interest in ^{11}B between the ^{7}Li + α threshold and the Q-value for β decay of ^{11}Be has been investigated in the past in several reaction experiments and the observed states are listed in Table 4.5. Since the spin-parity of the ^{11}Be ground state is $\frac{1}{2}^+$ allowed β decays proceed towards $\frac{1}{2}^+$ and $\frac{3}{2}^+$ states in ^{11}B. Since there are no other states with this spin-parity assignment in the energy region we are looking at, maybe the missing intensity of the theoretical fit can be explained by the forbidden transitions. However the smallest $\log(ft)$ values for first-forbidden transitions observed in the β decay are 6.830 ± 0.016 and 6.648 ± 0.025 for the ^{11}B ground state and first excited state at 2125 keV, respectively. These transitions are thus already a factor 100 less intense than the allowed transition to the state around 9.88 MeV, for which the present value $\log(ft) = 4.04 \pm 0.08$ [89] is tabulated. If we look at the dependence of the spherical bessel function, $j_L(kr)$, for an L-forbidden transition, $j_L(kr) \propto \frac{(kr)^L}{(2L+1)!!}$ [109] section 5.3.4, it is likely to think that the minimum $\log(ft)$ value for a first-forbidden transition in the region of interest is about 7, i.e. a factor 1000 more. Even the factor 100 would exclude the first-forbidden transitions from the present analysis.

Other possibilities that can explain the non-perfect fit result, are contributions of an extra $\frac{1}{2}^+$ state or the interference of the 9.876 MeV state with another $\frac{3}{2}^+$ state. These options are investigated in the following sections.

Incoherent contribution

In this section we are considering the contribution of a $J^\pi = \frac{1}{2}^+$ state in the decay energy spectrum. Since this spin-parity is different from the 9.876 MeV state, the angular correlations between the outgoing particles can be distinguished, and therefore their contributions can be summed incoherently. Hence the same approximation, i.e. one level-two channels, can be applied to the suggested $\frac{1}{2}^+$ level and the fitting procedure is now performed with 8 parameters. The first state that has isospin number $T = \frac{3}{2}$ ($T(^{11}\mathrm{Be}_{g.s.}) = \frac{3}{2}$) is the state at 12.557 MeV (Table 4.5). From isospin selection rules in β decay we therefore only include a Gamow-Teller transition to the suggested $\frac{1}{2}^+$ state. Since there is no $\frac{1}{2}^+$ ^{11}B state known in this energy region, see Table 4.5, all parameters are left free during the fit. The results are shown in Figure 4.8 and the resulting parameter values are given in Tables 4.6 and 4.7. State 1 and 2 correspond to

Table 4.5: ^{11}B levels in the region around the ^{7}Li + α threshold at 8.665 MeV and the ^{11}Be β-decay Q-value of 11.506 MeV, taken from [84]

E_x(MeV ± keV)	J^π;T	τ_m(fs) or $\Gamma_{c.m.}$(keV)
7.97784 ± 0.42	$\frac{3}{2}^+$; $\frac{1}{2}$	τ_m = 0.57 ± 0.06
8.5603 ± 1.8	$(\frac{3}{2}^-)$	0.70 ± 0.07
8.9202 ± 2.0	$\frac{5}{2}^-$	Γ = 4.37 ± 0.02eV
9.1850 ± 2.0	$\frac{7}{2}^+$	$1.9^{+1.5}_{-1.1}$eV
9.2744 ± 2	$\frac{5}{2}^+$	4
9.82 ± 25	$(\frac{1}{2}^+)$	
9.876 ± 8	$\frac{3}{2}^+$	110 ± 15
10.26 ± 15	$\frac{3}{2}^-$	150 ± 25
10.33 ± 11	$\frac{5}{2}^-$	110 ± 20
10.597 ± 9	$\frac{7}{2}^+$	100 ± 20
10.96 ± 50	$\frac{5}{2}^-$	4500
11.265 ± 17	$\frac{9}{2}^+$	110 ± 20
11.444 ± 19		103±20
11.600 ± 30	$\frac{5}{2}^+$	170 ± 30
11.886 ± 17	$\frac{5}{2}^-$	200 ± 20
12.000 ± 200	$\frac{7}{2}^+$	$\propto$ 1000
12.557 ± 16	$\frac{1}{2}^+(\frac{3}{2}^+)$; $\frac{3}{2}$	210 ± 20
12.916 ± 12	$\frac{1}{2}^-$; $\frac{3}{2}$	200 ± 25

Table 4.6: Results from the R-matrix fit assuming incoherent contributions from two levels with two break-up channels. The partial widths $\Gamma_{\lambda c}$ are calculated from the reduced widths $\tilde{\gamma}_{\lambda c}$ using the formula A.58 of Appendix A.5 . The percentage of the total width ($\Gamma_\lambda = \Gamma_{\lambda 1} + \Gamma_{\lambda 2}$) is given between brackets. $\chi^2_{red} = 1.22$

λ	$\tilde{E}_\lambda$(MeV)	$\tilde{\gamma}_{\lambda 1}$(MeV$^{1/2}$)	$\tilde{\gamma}_{\lambda 2}$(MeV$^{1/2}$)	
1 ($\frac{3}{2}^+$)	9.90(1)	0.95(5)	0.68(6)	
		Γ_{11}(keV)	Γ_{12}(keV)	Γ_1(keV)
		228(18) (93.1(9)%)	17(2) (6.9(9)%)	245(18)
2 ($\frac{1}{2}^+$)	10.76(2)	0.32(3)	0.8(8)	
		Γ_{21}(MeV)	Γ_{22}(MeV)	Γ_2(MeV)
		0.14(9) (20(30)%)	0.5(8) (80(30)%)	0.7(8)

Table 4.7: Results from the R-matrix fit assuming incoherent contributions from two levels with two break-up channels.

λ	$\tilde{g}_{\lambda,GT}$	$M_{\lambda,GT}$	$\log((ft_{1/2})_\lambda)$
1 ($\frac{3}{2}^+$)	1.05(6)	0.68(5)	4.12(7)
2 ($\frac{1}{2}^+$)	1.26(5)	1.0(6)	3.8(5)

the $\frac{3}{2}^+$ and $\frac{1}{2}^+$ states, respectively.

The suggested $\frac{1}{2}^+$ is fitted at 10.76 MeV but the width of about 700 keV is extremely large. Therefore it looks like the fitting procedure tries to apply a background contribution at higher energies by predicting a very broad state. The same artefact was encountered in the analysis of the elastic and inelastic scattering reactions ^{7}Li(α,α)^{7}Li and ^{7}Li(α,α')^{7}Li*(478 keV) where a broad $\frac{1}{2}^+$ level was introduced around 10.380 MeV (see 4.1) to generate a background at $E_{\alpha L} = 2.5$ MeV in the cross section spectra [86]. The fact that this $\frac{1}{2}^+$ level was not confirmed by any other measurement nor predicted by theoretical models, strengthens the belief of an artificial fit result. The only state that has no real spin-parity assignment in ^{11}B is a state around 11.44 MeV. This state is observed in the inelastic scattering reaction ^{7}Li(α,α')^{7}Li*(478 keV) together with the 9.88 MeV state but its width of 103 $\pm$ 20 is very small in comparison with our fit result. Nevertheless, the fit parameters for the state around 9.88 MeV are physically acceptable. From Table 4.7 we see that the result for the feeding of the state agrees with the literature value (4.04 $\pm$ 0.08 [89]) whereas the feeding of the extra $\frac{1}{2}^+$ state is highly overestimated.

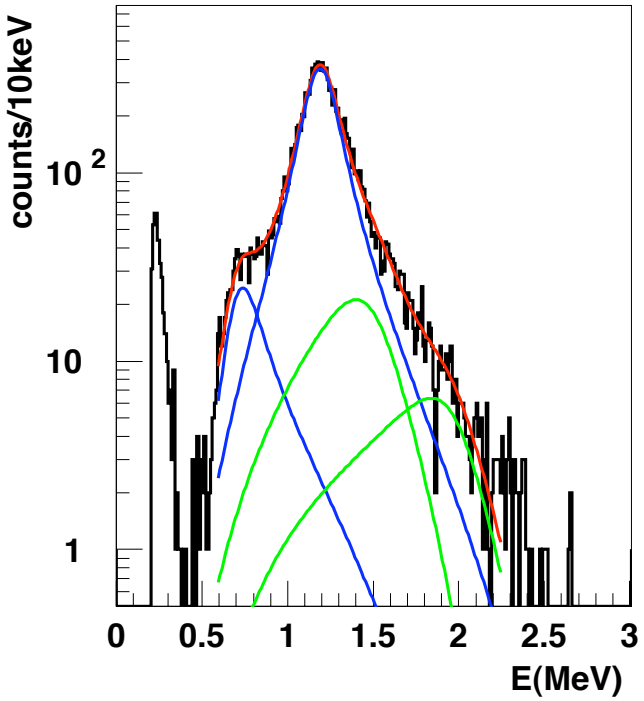

Figure 4.8: R-matrix fit of the ^{11}Be β-decay spectrum in the range [580 keV, 2250 keV] assuming two non-interfering states and two channels. The contributions for the $\frac{3}{2}^+$ and the $\frac{1}{2}^+$ states are shown in blue and green, respectively. The total theoretical curve is shown in red.

Coherent contribution

Another explanation for the current discrepancy between the theoretical curve and the experimental data is the presence of another $\frac{3}{2}^+$ state. Due to interference between the two states with the same spin-parity the line-shape of the 9.88 MeV state can be distorted. This second $\frac{3}{2}^+$ level can be situated either below or above the 9.88 MeV state, two possibilities that are covered separately below.

Subthreshold state

If the extra $\frac{3}{2}^+$ state is lying below the 9.88 MeV state, it is expected to be situated under the ^{7}Li + α threshold. The reason for this conclusion lies in the following fact. If the new level would lie in between it would have to be fed reasonably strongly to have an effect on the decay spectrum, so most likely one would have seen it already in the early ^{11}Be β-decay experiments. A candidate for the subthreshold state is the known level at 7.97784(42) MeV shown in Table 4.5. The feeding for this state is known, $\log(ft) = 5.576 \pm 0.033$.

When all parameters were left free in the fit, this resulted in an unphysical, negative, value for $\tilde{E}_2$, the resonance energy of the subthreshold state. Therefore this parameter was fixed at 7.99 MeV, which accounted for a β-summing shift of 12 keV for the state around 7.978 MeV according the simulations performed in Chapter 2.

The results are shown in Figure 4.9 and Tables 4.8 and 4.9. We can see from Table 4.9 that the contribution of the subthreshold state is highly overestimated by an unphysical amount. The feeding of the state around 9.88 MeV agrees with the current literature value. The width of the state however is rather large, the two reduced widths exceeding the Wigner limit (see Appendix A equation A.60). So, in conclusion the interference with another $\frac{3}{2}^+$ state below the ^{7}Li + α threshold does not appear to be the good physical answer to the problem.

Level above 9.88 MeV

The possibility of interference with a higher-lying state is discussed here. Figure 4.10 shows the result if the decay energy spectrum is divided by the β-decay phase space factor, f_β, using the parametrization proposed in [60] and described in Appendix A.5.1. In this modification the assumption was made that the energy in the spectrum corresponds to the summed ^{7}Li and α energies in the 'elastic' ^{7}Li(g.s.) + α channel. The upturn at higher energies in the corrected decay spectrum is a signature of interference of the state around 9.88 MeV with another higher-lying $\frac{3}{2}^+$ state. The interference is constructive between the two states and destructive in the region outside, resulting in the observed

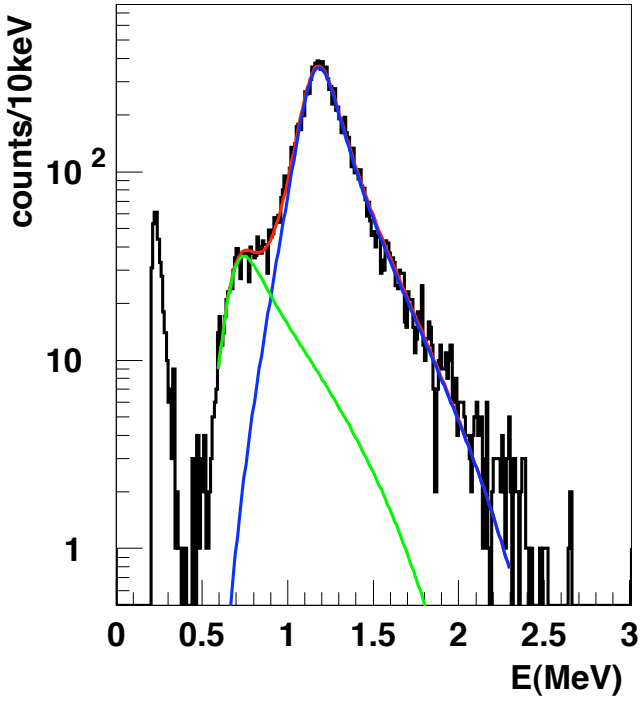

Figure 4.9: R-matrix fit of the ^{11}Be β-decay spectrum assuming contributions of two interfering $\frac{3}{2}^+$ states, one state around 9.88 MeV and another level fixed at 7.99 MeV under the ^{7}Li + α threshold. The contributions of the ^{7}Li(g.s.) + α and ^{7}Li(478 keV) + α channel are shown in blue and green, respectively. The total theoretical curve is shown in red.

Table 4.8: Results from the R-matrix fit using two coherently contributing $\frac{3}{2}^+$ levels and two channels. One level is fixed at an energy below the ^{7}Li + α threshold. The partial widths Γ_{1c} are calculated from the reduced widths $\tilde{\gamma}_{1c}$ using the formula of A.58 of Appendix A.5. The percentage of the total width ($\Gamma_1 = \Gamma_{11} + \Gamma_{12}$) is given between brackets. $\chi^2_{red} = 1.30$

λ	$\tilde{E}_\lambda$(MeV)	$\tilde{\gamma}_{\lambda 1}$(MeV$^{1/2}$)	$\tilde{\gamma}_{\lambda 2}$(MeV$^{1/2}$)	
1	9.887(4)	1.51(7)	1.31(7)	
		Γ_{11}(keV)	Γ_{12}(keV)	Γ_1(keV)
		261(18) (90.3(9)%)	28(2) (9.7(9)%)	289(18)
2	7.99 [1]	0.07(5)	0.08(5)	

[1] fixed energy, see text

Table 4.9: Results from the R-matrix fit using two coherently contributing $\frac{3}{2}^+$ levels and two channels.

λ	$\tilde{g}_{\lambda,GT}$	$M_{\lambda,GT}$	$\log((ft_{1/2})_\lambda)$
1	1.69(8)	0.75(6)	4.04(6)
2	16(9)	11(6)	1.7(5)

Table 4.10: Results from the R-matrix fit using two coherently contributing $\frac{3}{2}^+$ levels and two channels. The partial widths $\Gamma_{\lambda c}$ are calculated from the reduced widths $\tilde{\gamma}_{\lambda c}$ using the formula of A.58 of Appendix A.5 . The percentage of the total width ($\Gamma_\lambda = \Gamma_{\lambda 1} + \Gamma_{\lambda 2}$) is given between brackets. $\chi^2_{red} = 1.07$

λ	$\tilde{E}_\lambda$(MeV)	$\tilde{\gamma}_{\lambda 1}$(MeV$^{1/2}$)	$\tilde{\gamma}_{\lambda 2}$(MeV$^{1/2}$)	
1	9.896(3)	1.14(5)	0.85(4)	
		Γ_{11}(keV)	Γ_{12}(keV)	Γ_1(keV)
		255(15) (92.4(8)%)	21(2) (7.6(8)%)	276(15)
2	11.56(16)	-0.31(9)	0.01(16)	
		Γ_{21}(keV)	Γ_{22}(keV)	Γ_2(keV)
		310(180) ($\sim$ 100%)	1(10) ($\sim$ 0%)	310(180)

distortion of the 9.88 MeV lineshape. This type of interference is presented schematically in Figure 4.11.
To verify this physical solution by a fit using the R-matrix formalism, the same procedure as in the case of the extra subthreshold state was followed. All the parameters were left free. The results are shown in Figure 4.12 and Tables 4.10 and 4.11. For both states the matrix elements are calculated from the corresponding β-strength parameter according to equation A.48 in Appendix A. The resulting $\log(ft)$ value is only calculated for the state around 9.88 MeV since the center of the higher-lying state is situated above the Q-value and the integrated Fermi function, f, is only defined for energies below this threshold value. The feeding of the state around 9.88 MeV is in good agreement with the tabulated value (4.04 $\pm$ 0.08 [89]). The opposite signs for the reduced widths for the ^{7}Li(g.s.) + α channel of the two states reflect the interference effects described above. Because of the small contribution of the ^{7}Li(478 keV) + α channel and the fact that it is not well separated from the other channel, it is hard to draw conclusions on the relative signs for this 'inelastic' channel. Still, it is fair to say that the suggestion of the presence of a higher-lying $\frac{3}{2}^+$ state gives the best fit result. This is proven by the χ^2_{red} value of 1.07 in comparison with the fits described above. However, due to the rather low statistics of the experimental data no precise characteristics can be assigned for the suggested extra $\frac{3}{2}^+$ state. This will be further discussed in section 4.5.

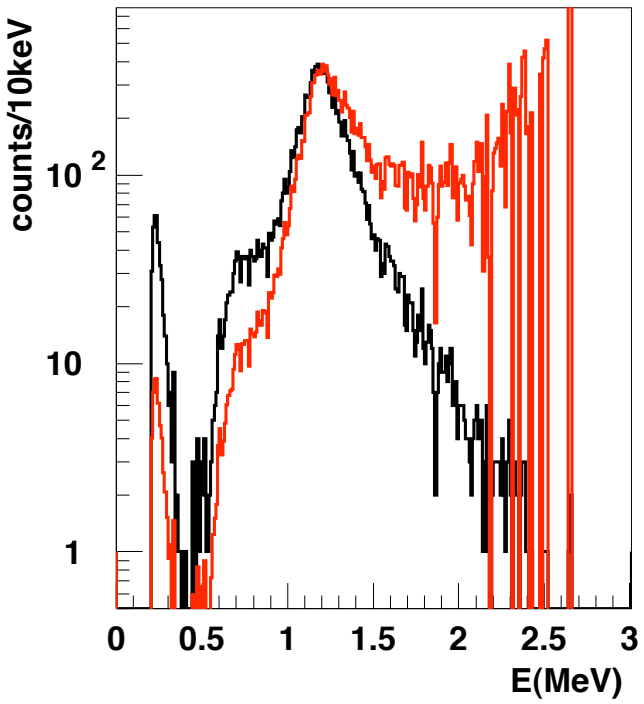

Figure 4.10: The lineshape of the state around 9.88 MeV is investigated by taking the β-decay phase space factor f_β out of the (black) experimental decay spectrum. The resulting (red) spectrum is normalized to the original one at 1.2 MeV.

Table 4.11: Results from the R-matrix fit using two coherently contributing $\frac{3}{2}^+$ levels and two channels.

λ	$\tilde{g}_{\lambda,GT}$	$M_{\lambda,GT}$	$\log((ft_{1/2})_\lambda)$
1	1.28(5)	0.74(4)	4.06(5)
2	1.6(6)	1.2(5)	/

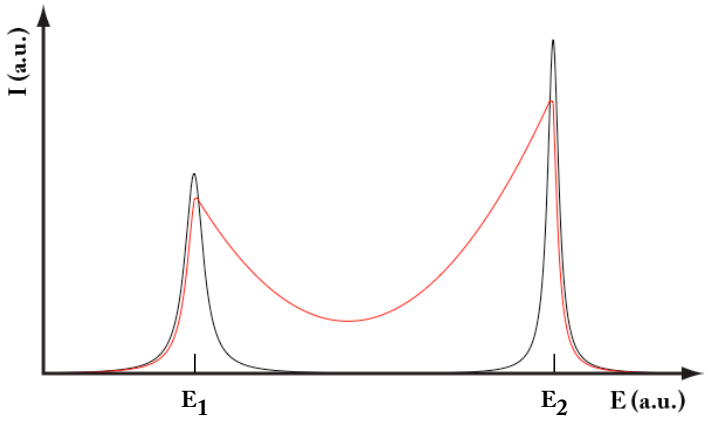

Figure 4.11: The energy spectrum for non-interfering states with Lorentzian lineshapes centered around the resonance energies E_1 and E_2 is presented in black without any background. If the states have the same spin and parity, interference between the two states can change the shape of the resonances. One of the possibilities mentioned in the text is the constructive and destructive interference in the energy region inside and outside the interval [E_1, E_2], respectively. This is shown schematically by the red spectrum.

4.4 ^{11}Be β-decay measurement at ISOLDE

4.4.1 Motivation

In section 4.3.2 the total ^{7}Li + α branching in the ^{11}Li β decay via bound states of ^{11}Be was calculated to be $(3.69 \pm 0.03)\times10^{-3}$. A procedure which can be used to find both branching ratios that contribute to this number was presented in the same section. This method and hence the final results depend on other experiments (e.g. [100, 101] and [102, 103]) measuring (relative) γ intensities in the β decays of ^{11}Be (via the β decay of ^{11}Li). A first estimate of $I_\gamma^{abs}(320\text{ keV}) = (20 \pm 3)\%$ was presented in the same section. To calculate this number the relative feedings of the two ^{7}Li + α channels were taken from [88]. From the R-matrix analysis described in the previous section it is however clear that we strongly disagree with these numbers. In the best fit with two coherently contributing $\frac{3}{2}^+$ ^{11}B states, the relative feedings of the ^{7}Li(g.s.) + α and ^{7}Li(478 keV) + α channels were found to be 92.4(8)% and 7.6(8)% (see Table 4.10), respectively, compared to 87.4(12)% and 12.6(12)% in [89]. With the new result for $\frac{I^{rel}_{^7Li}(\text{g.s.})}{I^{rel}_{^7Li}(478\text{ keV})}$ a value for $I_\gamma^{abs}(320\text{ keV}) = (12.0 \pm 1.6)\%$ is

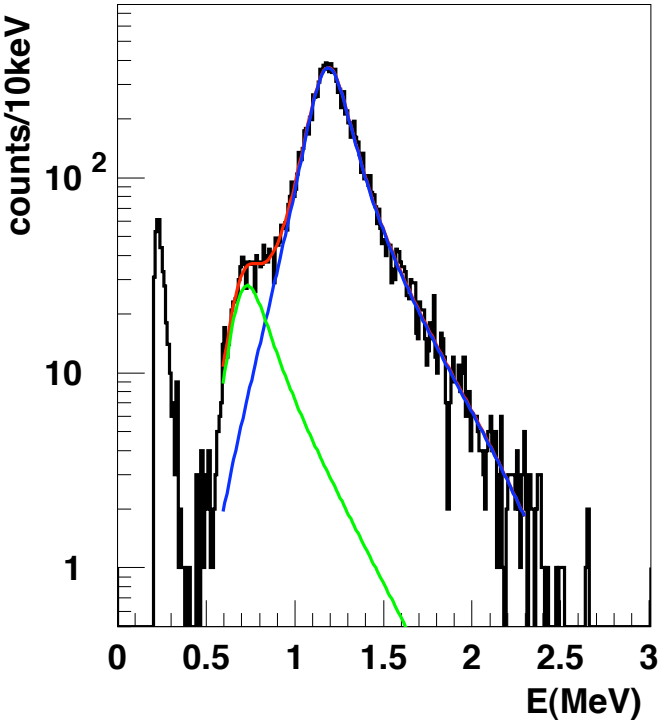

Figure 4.12: R-matrix fit of the ^{11}Be β-decay spectrum assuming contributions of two interfering $\frac{3}{2}^+$ states, one state around 9.88 MeV and one higher-lying state. The contributions of the ^{7}Li(g.s.) + α and ^{7}Li(478 keV) + α channel are shown in blue and green, respectively. The total theoretical curve is shown in red.

calculated when the same values for $\frac{I_\gamma^{rel}(478\text{ keV})}{I_\gamma^{rel}(2125\text{ keV})} = 0.0066(5)$ ([100, 101] and [102, 103]) and $I_\gamma^{abs}(2125\text{ keV}) = (35.5 \pm 1.8)\%$ [89] are used. This result still disagrees with the average value of $(7.5 \pm 0.3)\%$ by a factor 1.6 .

If, on the other hand, one of the two branching ratios, $I_\gamma^{abs}(320\text{ keV})$ or $I_{^7\text{Li}+\alpha}^{abs}$, could be measured directly with our experimental technique, the other value can be found from their product. The first excited state of ^{11}Be is a bound state. Hence the β feeding of this level is followed by a γ-ray emission which we do not detect. Since we are, with the present experimental setup, also insensitive to β-delayed neutron emission it is not possible to experimentally determine the feeding of the ^{11}Be first excited state in the β decay of ^{11}Li. The total ^{7}Li + α branching in the β decay of ^{11}Be, $I_{^7\text{Li}+\alpha}^{abs}$, however can be measured if the ^{11}Be nuclei are directly implanted in the DSSSD. It was with this objective that another experiment was performed at ISOLDE (CERN, Geneva, Switzerland) which will be described in this section. Moreover we can compare the obtained charged-particle decay spectrum with the one from the earlier TRIUMF experiment. By performing the same R-matrix analysis on this new data we can check the results presented in section 4.3.2.

4.4.2 Experimental Setup

The ^{11}Be nuclei were produced at ISOLDE by an energetic 1.4 GeV proton beam with an average intensity of 1.3 μA on a Ta target. The protons are delivered by the PS (Proton Synchrotron) booster. In this experiment 10 out of 14 proton pulses, that come every 1.2 s, of the supercycle of the PS booster were sent to the ISOLDE target. After surface ionization in a tungsten tube and selective laser ionization by the RILIS (Resonant Ionization Laser Ion Source [113]) the radioactive ion beam (RIB) is mass separated by the General Purpose Separator (GPS). After injection of the continuous RIB in a Penning Trap (REXTRAP), short ion bunches are transported to the Electron Beam Ion Source (EBIS) for charge breeding. The beam delivered by EBIS consists of the required radioactive ions originating from the ISOLDE target and residual gas ions from the REXTRAP combination. Therefore an additional mass separation according to A/q is required. At a rate of $\sim$ 39Hz the EBIS injects bunches of particles in the REX (Radioactive beam EXperiment) linear accelerator and about 1 ms after the EBIS spill, the radio frequency (RF) of REX was switched off. In the linac the ions are accelerated to the desired energy. The ^{11}Be ions (4+) were transported to the experimental setup with an energy of 2.86 MeV/A.

The experimental setup consisted of the DSSSD, extensively described in Chapter 2, and a 500 μm thick Si surface barrier detector placed behind it. The beam contained some ^{22}Ne contaminant. To prevent these stable ions from

being implanted in the DSSSD, six 6 μm thick aluminium foils were placed in front of the detector. After passing these foils the ^{11}Be ions still had an energy of $\sim$ 15 MeV, corresponding to an implantation depth of $\sim$ 25 μm in the DSSSD (78 μm thickness). The ^{22}Ne contaminant with an energy of $\sim$ 60 MeV on the other hand was completely stopped by the aluminium foils. In the end $\sim$ 1E+5/s ^{11}Be ions were implanted in the detector.

The electronics scheme of the experimental setup is presented in Figure 4.13. The data acquisition system "ISOLDE DAQ", an implementation of the Multi-Branch System [52], was used and run in multi-event mode. The physics triggers, related to events in the DSSSD and the back detector, do not generate a readout but only gates on the ADC, TDC and scaler modules, always on all modules together. These modules convert the data and keep them in a buffer until a readout occurs. This readout is made always on all modules of which some can be empty. Reconstruction of the events in a buffer is made possible by counters that identify the corresponding events in ADC's, TDC's and scalers. Readouts can be forced by:

- An "EBIS trigger": this trigger occurs 1 ms after the EBIS spill, i.e. when the REX RF was off. The number of this kind of incoming triggers during the experiment is exactly known since these events are counted on the scaler module.

- A "T1 trigger": this trigger is generated by a proton spill. This means that this trigger can occur every 1.2 s but it depends on the proton supercycle. Like "EBIS triggers" the exact number of incoming "T1 triggers" is counted by the scaler module.

- A "forced T1 trigger": if for 20 s there are no protons, a software trigger is automatically generated which forces a readout. These triggers are not counted in the scaler.

- A "buffer full trigger": when one of the converter modules has a full buffer (32 events) an interrupt is generated which forces a readout of all modules.

A clock is connected to a scaler channel for absolute time information. In this case 1 unit corresponded to 1 μs and with only 26 bits this means that the clock restarted every $\sim$ 67 s. The total duration of the experiment, which consisted of four subsequent "runs", can be derived from this clock information by looking at the number of clock restarts and the time information at the beginning and end of each run.

During conversion of the data and the buffer readout, the system is busy and no triggers are accepted to generate gates. From Figure 4.13 it is clear that the total dead time is the total "OR" of all conversion and readout intervals.

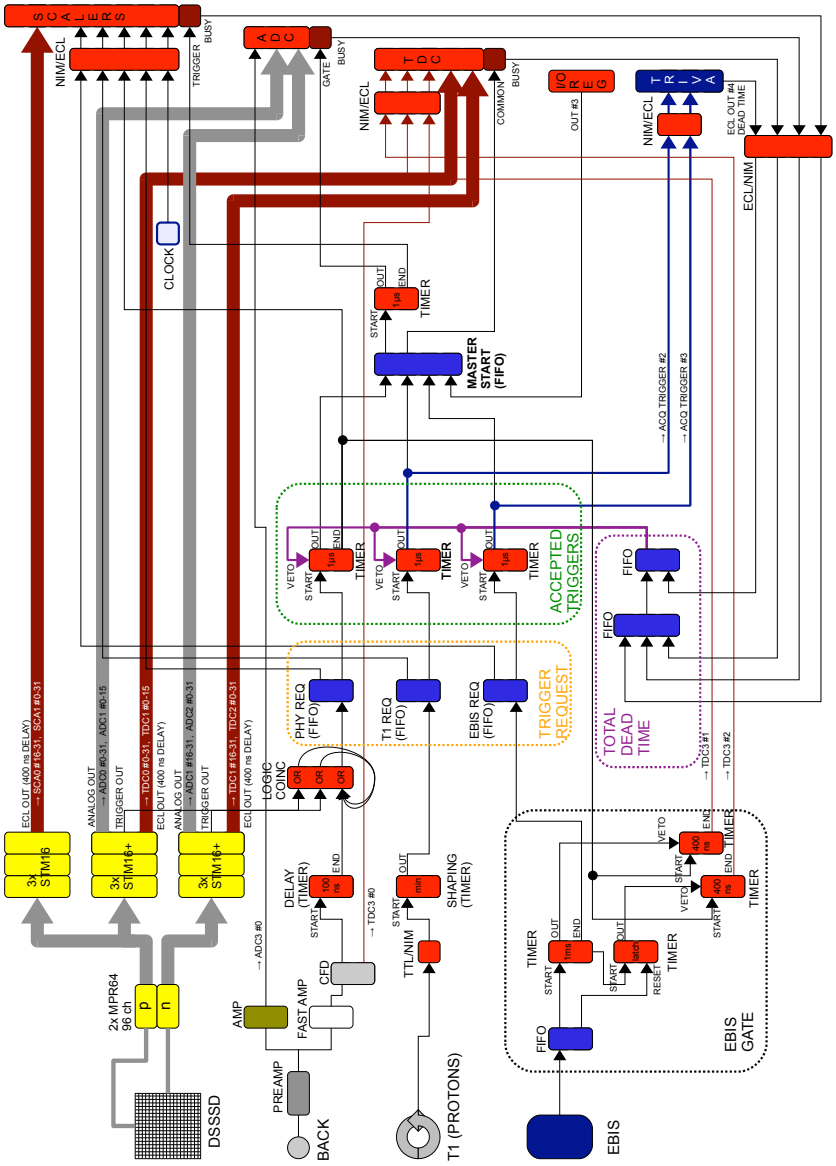

Figure 4.13: Electronics scheme that was used for the β-decay measurement of ^{11}Be at ISOLDE.

The typical dead time related to the data conversion is $\sim$ 9 μs as seen by the time information of two subsequent events. The dead time following a readout depends on the kind of trigger: "EBIS trigger" $\sim$ 9 μs, "T1 trigger" $\sim$ 11 ms, "forced T1 trigger" $\sim$ 40 ms and "buffer full trigger" $\sim$ 2.5 ms. An extra contribution to the total dead time comes from the fact that the data file has to be saved to a harddisk. During this process the system is busy for about 1 s.

The 48 front strips of the DSSSD are connected to two sets of three Mesytec STM-16 amplifiers [51]. One set has a high gain setting (like the amplifier set for the back strips), chosen to ideally observe the charged-particle emission events in the ^{11}Be β decay. The other set has a low gain setting and the energy threshold on these modules is placed at 8 MeV. This energy value is much higher than the Q-value for β-delayed charged-particle emission, Q_α = 2.841(7) MeV, and possible background radiation. The triggers originating from these three amplifiers are hence coming from implantation events. They are counted in the scaler in 48 separate channels, free from dead-time effects (Figure 4.13). In this way we can directly measure the number of ^{11}Be ions that were implanted during the experiment.

The accepted triggers, related to either physics events or EBIS/proton spills, all generate gates on the converter modules. To identify a real physics event as an event occuring during the beam on or beam off period, a flag was created in the TDC modules. This is shown in Figure 4.13 ("EBIS GATE") and illustrated in Figure 4.14. One TDC channel is related to the beam on period and another one to the beam off period, and only one of them is active in the corresponding beam interval. In principle, to calculate the α branching ratio in the β decay of ^{11}Be the number of decay events related to ^{7}Li + α emission have to be counted in all beam off periods. However, the total dead time of the system makes the calculation a bit more difficult. Due to this dead time some triggers are not accepted. Amongst them, there are "EBIS triggers" that indicate the beginning of the beam off period (and thus the end of the beam on period). Given the period of the EBIS cycle, $\sim$ 25.6 ms, and the dead time of 1 s for saving to disk, it is possible that the decays occuring in about 40 EBIS cycles cannot be observed. The implantation events of these cycles on the other hand are constantly counted by the scaler. So a procedure had to be worked out to define good decay periods for which a total decay and dead time could be measured. The first event in the beam off period after a beam on period indicates the start of a decay time interval. The timestamp of this event is held in the memory as a reference as well as the number of requested and accepted physics triggers. From this moment on the number of decays can be counted, always remembering the last number of requested and accepted triggers. If then a beam on event is registered, the time difference between this event and the start reference of the beam off period is checked. When this time difference

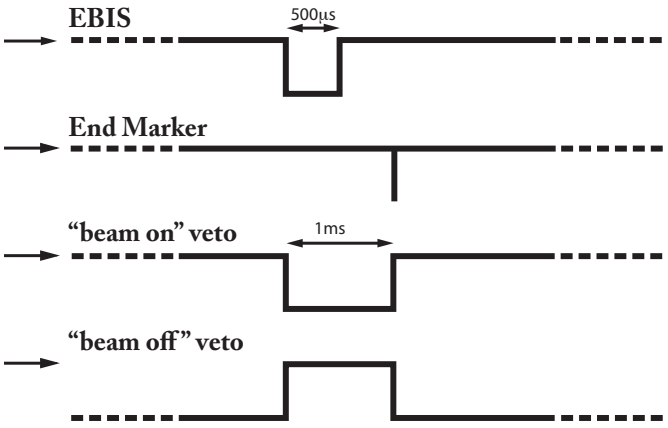

Figure 4.14: The EBIS (black) signal is the start to a gate of length 1 ms, the "beam on" veto (see Figure 4.13), of which the End Marker is used to open a new gate, the "beam off" veto on a dual timer (see Figure 4.13) in latch mode. This last timer is reset by the original EBIS pulse. The periodicity of these signals is about 25.6 ms. The End Marker also works as an "EBIS trigger" for readout of the converter buffers. The two gates are sent as vetos on dual timers where the input comes from an accepted physics event. After a delay of $\sim$ 400 ns the End Markers are sent to corresponding TDC channels.

is smaller than the length of the EBIS period, the beam off period is listed as a 'good' decay interval. The corresponding decays measured in this kind of periods are saved for further analysis. The procentual dead time in the decay interval is calculated by taking the ratio of the differences in accepted and requested physics triggers between the last decay event and the start reference.

4.4.3 Results

The ^{11}Be β-decay spectrum is measured in periods where the beam is stopped. To suppress the β-particle contributions from the feeding of bound ^{11}B states, appropiate conditions have to be used in the off-line analysis. Every strip had a very low noise level during this experiment. Given this fact, the multiplicity of events (see Chapter 2) is defined by the number of strips on both sides that have both an ADC and a TDC signal in coincidence, requiring just a non-zero energy value. If only *M11* events are accepted in the analysis, we obtain the black spectrum in Figure 4.15 where the number of events are given as a

function of the average energy of the two detector faces. The energy threshold of 200 keV is chosen to limit the size of the analysis files. This *M11* condition strongly suppresses the pure β-particle contribution at low energies. However, in this way we lose charged-particle emission events where the energy is shared between two neighboring strips on one or both sides. To account for this, we add the energies of the two neighboring strips if the multiplicity on that side is equal to 2 and assign the summed energy to the strip with the highest initial energy (see Paper I). By doing so we can reconstruct new *M11* events from events that were initially labelled as *M12*, *M21* or *M22* events. The resulting energy spectrum is presented in red in Figure 4.15. In the energy region between 200 keV and 400 keV about 8 times more events are counted with respect to the original *M11* spectrum (black). So, the pure β-particle signals are less suppressed with these reconstruction conditions. But in the interesting energy region between 400 keV and 2.8 MeV, where we expect to see the charged-particle emission events, 17% more events are observed.

In order to obtain a good β-suppression factor without losing good charged-particle emission events, an extra condition had to applied to the reconstruction method. The energies of two neighboring strips are only added when at least one of the two strips has an energy higher than a certain threshold value. This threshold value has to be chosen on a good physical basis. The GEANT4 simulation of the energy loss of β particles in one pixel of the DSSSD, presented in Chapter 2, can be a guide in this respect. In Figure 2.11 in the latter Chapter we see that the highest deposited energy for β particles is about 200 - 250 keV. In Figure 4.16 the decay energy spectra for different threshold values are presented. The red spectrum, corresponding to a threshold value of 0 keV, is the same as in Figure 4.15. One can clearly see that a higher threshold value suppresses more pure β events whereas at higher energies only minor differences are observed. For further analysis the threshold value of 350 keV was chosen, corresponding to the blue spectrum, presented in Figure 4.15 and Figure 4.16. From Figure 4.15 one can conclude that the recombination procedure with the threshold value of 350 keV gives approximately the same β suppression as the pure *M11* condition. For higher energies the actual value of the threshold value is not crucial as indicated by the agreement between the red and the blue spectra.

In Chapter 2 it was shown that the pure β contribution can be further reduced by requiring a maximum energy difference between the front and the back side of the DSSSD. In this analysis of this experiment the condition $|E_1 - E_2| < 160$ keV was applied. This choice was defined by the spread of events around $E_p = E_n = 1.2$ MeV in Figure 4.17 where the events in the decay period (with the recombination threshold value of 350 keV) are shown in a scatter plot presenting the energy of the back side versus the energy of the front side of the DSSSD. The same concept was actually applied for the data presented in the

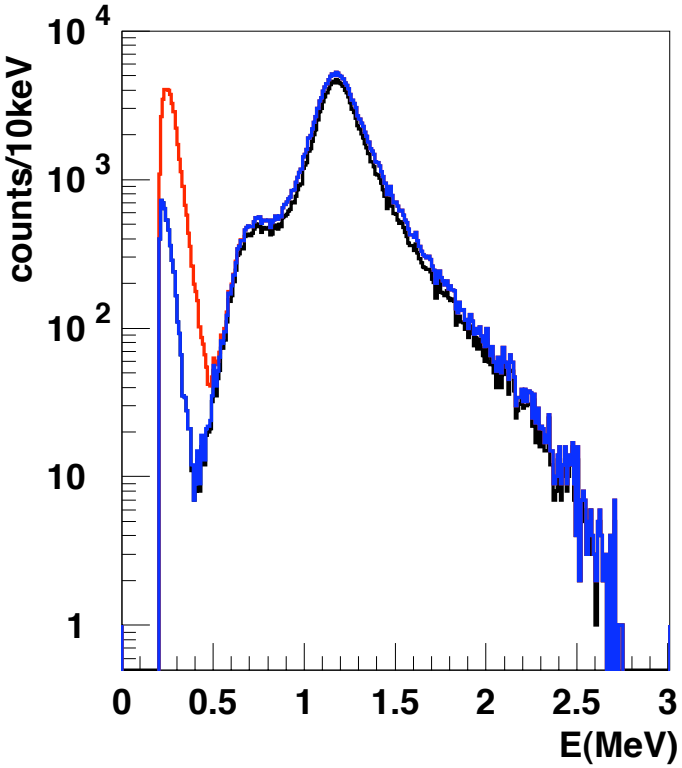

Figure 4.15: ^{11}Be β-decay energy spectrum. The black spectrum corresponds to pure *M11* events. Reconstructed *M11* events (see text) using an energy threshold of 0 keV and 350 keV are shown in red and blue, respectively.

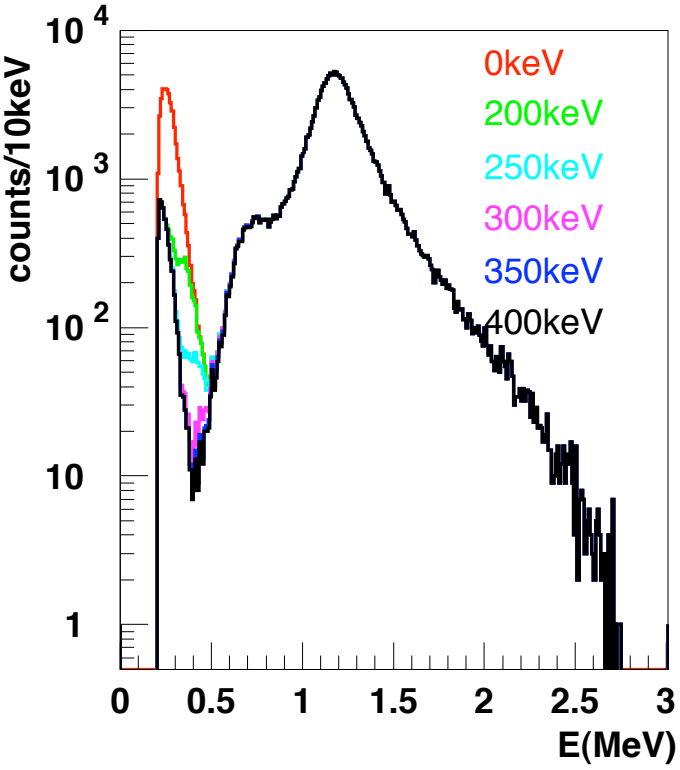

Figure 4.16: ^{11}Be β-decay energy spectra corresponding to reconstructed *M11* events (see text) are presented in this plot. Different energy thresholds were used as indicated.

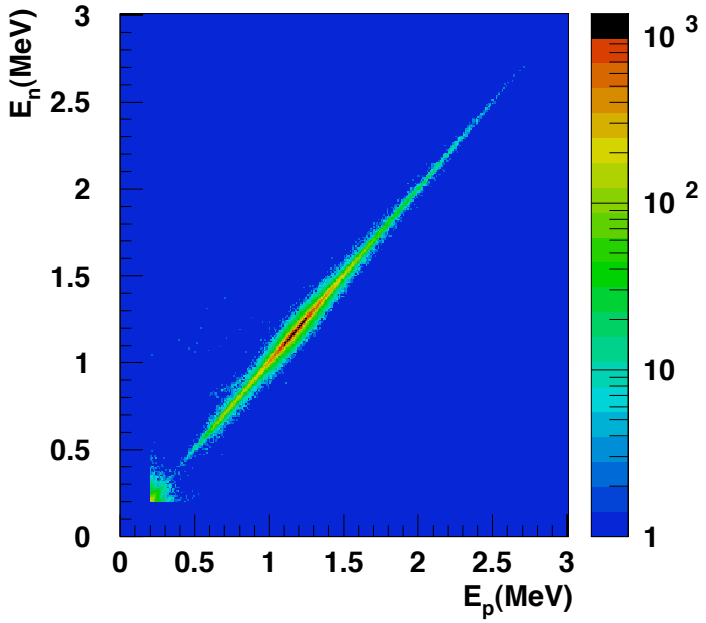

Figure 4.17: Energy scatter plot of ^{11}Be β-decay events. More info is given in the text.

previous section 4.3, with a recombination threshold value of 500 keV and a maximum energy difference of 200 between the two detector faces. The decay energy spectra of the two different data sets are compared in Figure 4.18. For the TRIUMF data the spectrum that was obtained after waiting 5 seconds in the beam off period and analysed using the R-matrix framework in section 4.3 was taken for this figure. The spectra are normalized to each other around the center of the largest contribution in the charged-particle emission at 1.2 MeV, the ISOLDE spectrum containing about 14 times more statistics than the one from the TRIUMF data. The figure shows a very nice qualitative agreement of the decay spectra, both at low and high energies.

Branching ratio calculation

To calculate the total α branching in the β decay of ^{11}Be 'good' decay periods were selected as explained in the previous section 4.4.2. The total time interval in which the charged-particle decay events were counted was 1251.092 s (T_D). The total time of the measurement on the other hand was 3142.796

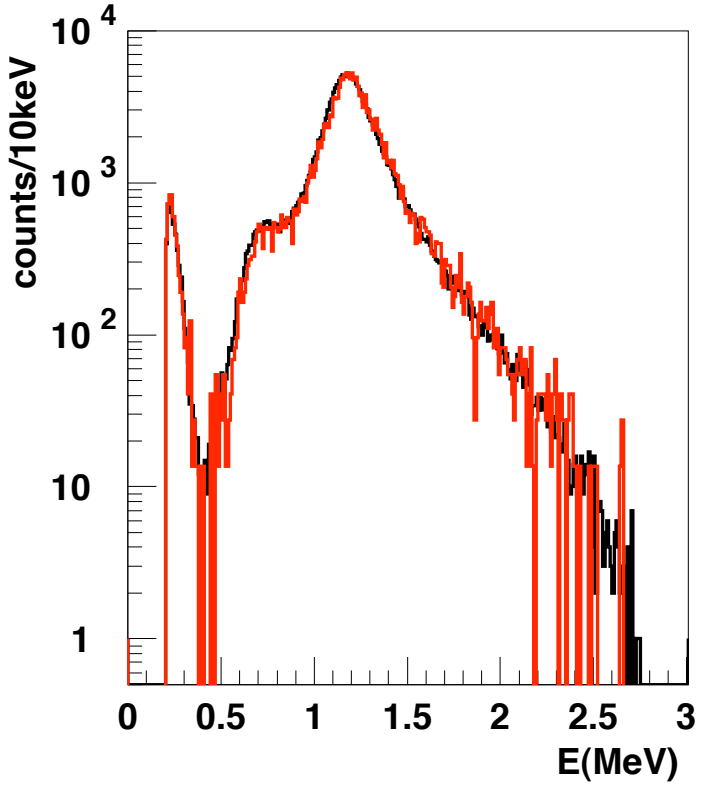

Figure 4.18: ^{11}Be β-decay energy spectra from the experiments at ISOLDE and TRIUMF (red), normalized to each other at 1.2 MeV.

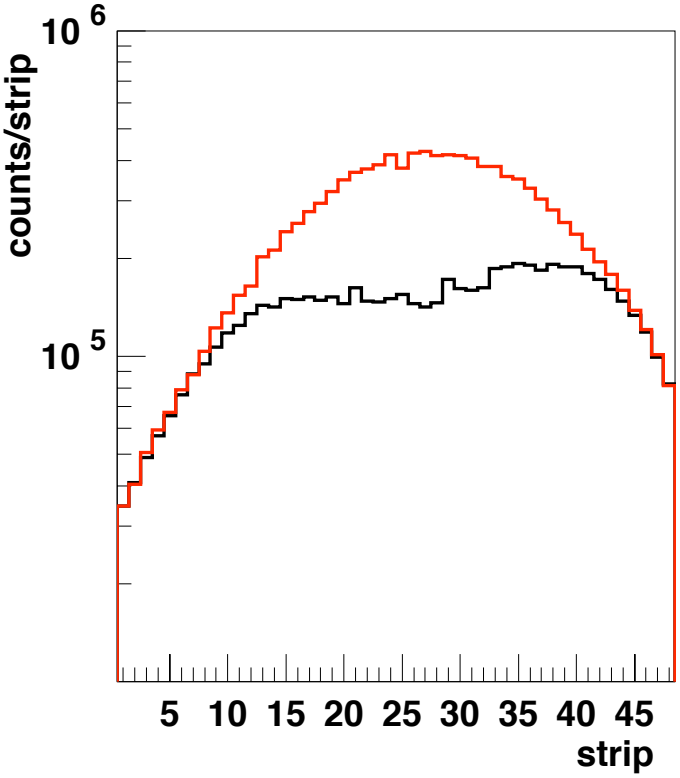

Figure 4.19: Number of implantations and decays per front strip of the DSSSD, normalized at the first strip.

s (T_T). Because of the large half life of ^{11}Be ($T_{1/2}$ = 13.81(8) s [82]) with respect to the beam on/off structure the decay is measured in saturation mode. Therefore only 39.8% of the total number of decays was taken into account for the branching ratio calculation. The acquisition dead time in the total decay period was calculated to be 11.69% (DT_D) by counting the number of requested and accepted triggers in all the time intervals that contribute to this period (see above, 4.4.2).

The number of implantations can be derived from the scaler counts corresponding to the triggers of the shapers with high-energy thresholds. Figure 4.19 shows the number of implantations as a function of the strip number on the front side of the detector. This profile can be compared with the number of decays per strip, also presented in Figure 4.19, but scaled to the number of im-

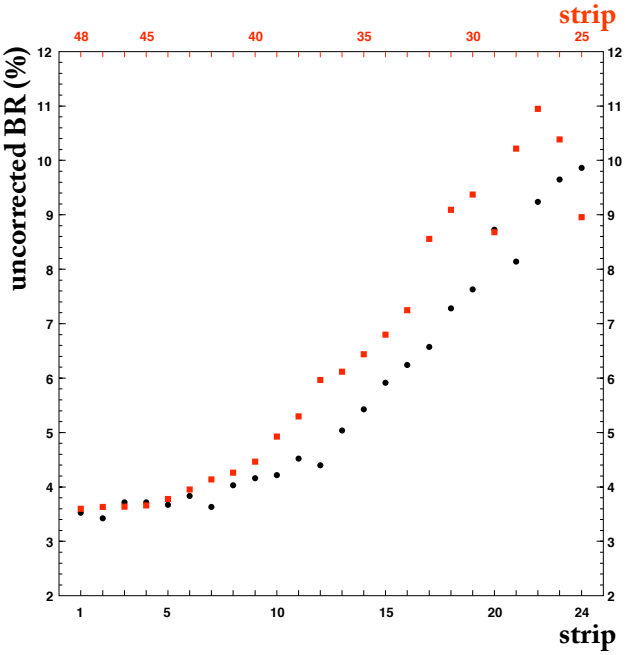

Figure 4.20: The calculated uncorrected (see text) ^{7}Li + α branching (%) in the β decay of ^{11}Be is presented here as a function of the strip number.

plantations by normalizing to the first strip. Whereas the decay profile shows a normal distribution of the events over the detector area, there is clearly a saturation effect for implantations in the strips around the center of the detector. Only for the first 7 and last 5 strips the difference between the two profiles stays within 10%. Since the beam is focused on the DSSSD the implantation rate around its center is higher than at its edges. If the implantation rate in a strip becomes higher, additional to an increase in dead time, it becomes more probable that pile-up effects show up in the electronic channel. This is the main reason for the saturation effect seen in Figure 4.19. It is nevertheless clear from the same figure that the implantation rate is not the only contributing factor since this rate is obviously higher in the last 5 strips than in the first 7 strips. So there must also be a dependence on the individual electronic channel corresponding to a specific strip.

In every strip of the front side of the detector an uncorrected branching ratio can be calculated by counting the number of implantations and decays in that strip. The term uncorrected is used because from Figure 4.19 it is clear

that the counted number of implantations in the scaler does not correspond to the real number of implantations for every strip. The total implantation and decay time as well as the acquisition dead time given above are used in this calculation. In Figure 4.20 the uncorrected branching ratio is plotted as a function of the strip number. The black points correspond to the first 24 strips whereas the red points refer to the last 24 strips shown in reverse order. It is clear that due to the saturation effect for implantations described above there is a steep increase of the uncorrected branching ratio towards the center of the detector. The trend for the values at the edge strips (first 7 and last 5) can be approximated by a horizontal line. Since we are sure that not in all these strips the correct number of implantations is counted, only the first two strips will be used for the calculation of the α branching ratio. In these two strips the implantation rate is the lowest over the whole surface of the detector and hence the probability of pile-up effects is smaller than in the other strips. The number of implantations and decays counted in these two strips are 75422 and 920, respectively. The number of decays are counted in the energy interval [400 keV, 2.8 MeV], where we expect the charged-particle emission events. The ^{7}Li + α branching ratio is thus calculated by the following formula, where I and D refer to the number of implantations and decays in the first two strips, T_T = 3142.796 s and T_D = 1251.092 s are the total measurement time and the total decay time interval, respectively, and DT_D = 11.69% the acquisition dead time in the latter period:

$$\begin{aligned} \mathrm{I}^{\mathrm{abs}}_{^{7}\mathrm{Li}+\alpha} &= \frac{D \times T_T}{I \times T_D \times (1 - DT_D)} \\ &= (3.47 \pm 0.12) \times 10^{-2} \end{aligned} \tag{4.8}$$

In this result the error is defined by the statistical uncertainty on the number of decays and implantations.

The total branching ratio for ^{11}Li β-decay channels to the ^{11}Be ground state or states that decay to this latter state can now easily be calculated from the result for the total ^{7}Li + α branching in the ^{11}Li β decay via those bound states, $(3.69 \pm 0.03)\times10^{-3}$, presented in section 4.3.2. We obtain a value of $(10.6 \pm 0.4)\times10^{-2}$. Since the β decay to the ^{11}Be ground state is first-forbidden and no ground state feeding γ-ray transitions in ^{11}Be have been observed other than the 320 keV line, we assume this number corresponds to the branching ratio to the first excited state at 320 keV of ^{11}Be. This result will be further discussed in section 4.5.

R-matrix analysis

In this section the charged-particle spectrum that was presented in blue in Figure 4.15 will be analysed using the R-matrix framework. It was already pointed out that the decay spectra of both experiments at TRIUMF and ISOLDE show nice agreement (Figure 4.18). Especially in the higher energy region the gain in statistics in the spectrum from the ISOLDE data will provide more information on the possible contributions of other ^{11}B states than the one at 9.876 MeV in the ^{11}Be β-delayed charged-particle emission. As was done in the section 4.3.2 the new decay energy spectrum is divided by the β-decay phase space factor, f_β, using the parametrization presented in Appendix A.5.1. Like in Figure 4.10 a clear upturn at high energies is observed in Figure 4.21. So, it is shown that this feature is no artefact coming from the low statistics in that energy region in Figure 4.10. From this result, it should not be a surprise that the R-matrix analysis with two coherently contributing states (one around 9.88 MeV and one higher-lying one) and two decay channels gave the best results in section 4.3. With the new data and the same R-matrix framework, one now can try to obtain more precise quantitative information on the ^{11}B states that are involved in the ^{7}Li + α emission following the ^{11}Be β decay.

For a correct normalization in the fitting procedure with formula A.56 we again need the number of counts (N) in the energy interval [400 keV, 2.8 MeV], i.e. $N = 180236 \pm 425$. The partial half life, $t_{1/2}$, to this energy region is again calculated with the result presented by equation (4.8) for the α branching in the ^{11}Be β decay, $t_{1/2} = (398 \pm 14)$ s. All 8 parameters ($\tilde{E}_\lambda$, $\tilde{\gamma}_{\lambda i}$, $\tilde{g}_{\lambda,GT}$; λ = 1,2 and i = 1,2) were left free in the fit. The results are presented in Figure 4.22 and Tables 4.12 and 4.13.

The first state around 9.88 MeV has a large coupling to the ^{7}Li(g.s.) + α channel presented by the large reduced width $\tilde{\gamma}_{11}$. The resulting partial widths for the channels, ^{7}Li(g.s.) + α and ^{7}Li(478 keV) + α, are about 92% and 8% of the total width, respectively. The feeding of the state is shown in Table 4.13 to agree with the present literature value (4.04 ± 0.08 [89]). These results will be further discussed in section 4.5.

The second contributing $\frac{3}{2}^+$ state that interferes with the first state is expected at an energy of about 11.57 MeV. This means that this state is lying almost 65 keV above the Q-value for the ^{11}Be β decay, $Q_{\beta^-} = 11.506(6)$ MeV. Because of its width, fit to a value of 112 keV, the tail of the resonance falls in the available energy window and interference between the two states comes into play. The kind of interference effect that is predicted from the shape of the spectrum in Figure 4.21 has already been shown in Figure 4.11. The opposite signs of the reduced widths for the ^{7}Li(g.s.) + α channel of the two states again represent this constructive interference between the two states. Because the center of the second state is lying above the Q-value for β decay, the $\log(ft)$

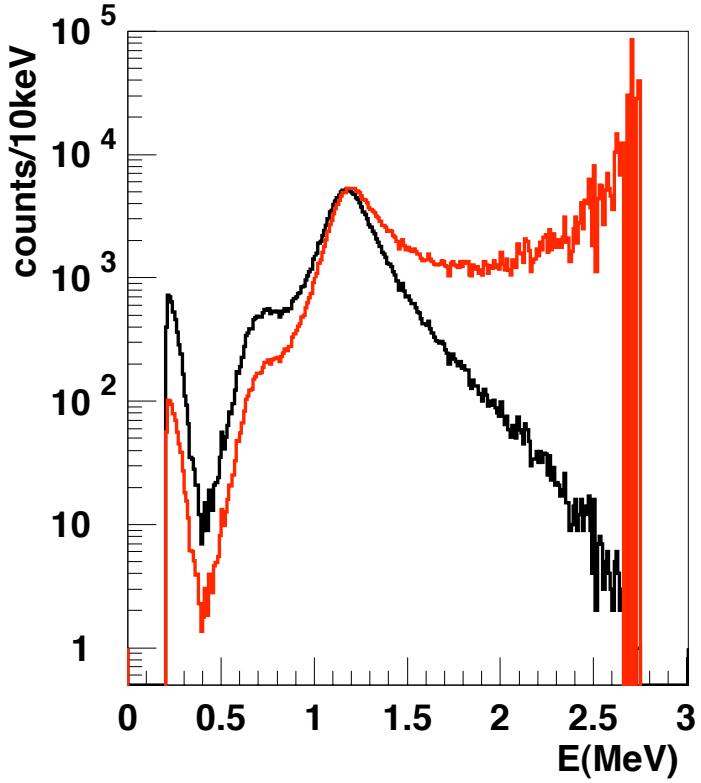

Figure 4.21: The lineshape of the state around 9.88 MeV is investigated by taking the β-decay phase space factor, f_β, out of the (black) experimental decay spectrum. The resulting (red) spectrum is normalized to the original one at 1.2 MeV.

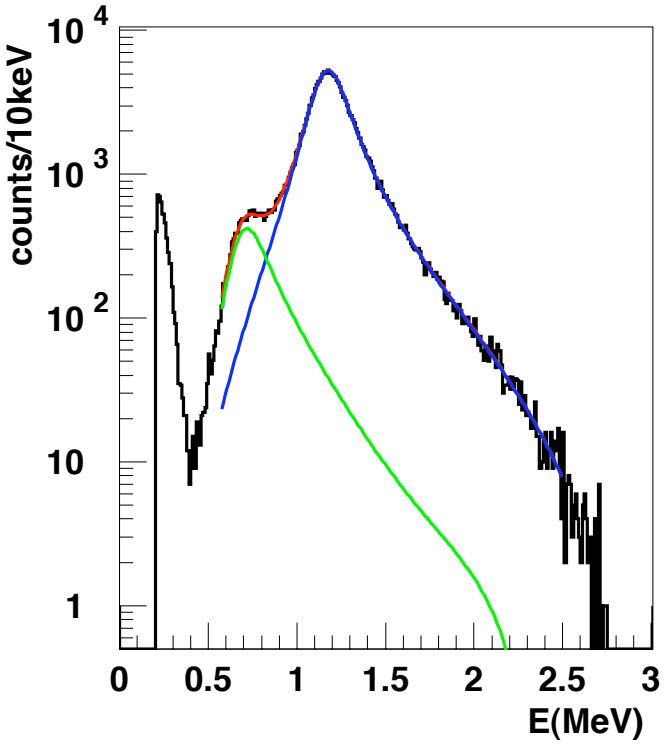

Figure 4.22: R-matrix fit of the ^{11}Be β-decay spectrum assuming contributions of two interfering $\frac{3}{2}^+$ states, one state around 9.88 MeV and one higher-lying state. The contributions of the ^{7}Li(g.s.) + α and ^{7}Li(478 keV) + α channel are shown in blue and green, respectively. The total theoretical curve is shown in red.

value is not defined and the strength of the transition to this state has to be derived from the matrix element (see Table 4.13).

Table 4.12: Results from the R-matrix fit using two coherently contributing $\frac{3}{2}^+$ levels and two channels. The partial widths $\Gamma_{\lambda c}$ are calculated from the reduced widths $\tilde{\gamma}_{\lambda c}$ using the formula of A.58 of Appendix A.5 . The percentage of the total width ($\Gamma_\lambda = \Gamma_{\lambda 1} + \Gamma_{\lambda 2}$) is given between brackets. $\chi^2_{red} = 1.04$

λ	$\tilde{E}_\lambda$(MeV)	$\tilde{\gamma}_{\lambda 1}$(MeV$^{1/2}$)	$\tilde{\gamma}_{\lambda 2}$(MeV$^{1/2}$)	
1	9.885(1)	1.228(13)	0.958(15)	
		Γ_{11}(keV)	Γ_{12}(keV)	Γ_1(keV)
		252(4) (92.0(4)%)	22(1) (8.0(4)%)	274(10)
2	11.57(3)	-0.180(12)	0.049(20)	
		Γ_{21}(keV)	Γ_{22}(keV)	Γ_2(keV)
		106(14) (95(4)%)	6(5) (5(4)%)	112(15)

Table 4.13: Results from the R-matrix fit using two coherently contributing $\frac{3}{2}^+$ levels and two channels.

λ	$\tilde{g}_{\lambda,GT}$	$M_{\lambda,GT}$	$\log((ft_{1/2})_\lambda)$
1	1.351(15)	0.727(12)	4.065(15)
2	2.78(20)	2.04(15)	/

4.5 Discussion

4.5.1 β decay of ^{11}Li towards the first excited state at 320 keV in ^{11}Be

In section 4.4.3 the ^{7}Li + α branching in the β decay of ^{11}Be was measured to be $I^{abs}_{^7Li+\alpha} = (3.47 \pm 0.12)\%$. This value is in good agreement with the present literature value of $(3.1 \pm 0.4)\%$ [89]. Combining this result with the total ^{7}Li + α branching in the ^{11}Li β decay measured at TRIUMF (section 4.3.2) a branching ratio to the first excited state at 320 keV in ^{11}Be in the ^{11}Li β decay was obtained, $I^{abs}_\gamma(320\text{ keV}) = (10.6 \pm 0.4)\%$. This result disagrees with an average literature value of $(7.5 \pm 0.3)\%$ by a factor 1.41(8).

From the R-matrix analysis of the energy spectrum of the ^{11}Be β decay, measured at TRIUMF, the relative feedings of the two ^{7}Li + α channels were found to be 92.4(8)% and 7.6(8)%, for the ^{7}Li ground state and first excited state, respectively. With the procedure presented in section 4.3.2 an alternative value $I^{abs}_\gamma(320\text{ keV}) = (12.0 \pm 1.6)\%$ was calculated (see section 4.4.1). During the more recent experiment at ISOLDE (section 4.4) more statistics was obtained and the corresponding relative feedings of the ^{7}Li + α channels found

by the R-matrix analysis, are 92.0(4)% (^{7}Li(g.s.)) and 8.0(4)% (^{7}Li(478 keV)). Using the same values for the relative γ-intensity, $\frac{I_\gamma^{rel}(478\text{ keV})}{I_\gamma^{rel}(2125\text{ keV})} = 0.0066(5)$ ([100, 101] and [102, 103]), and the absolute γ intensity in the ^{11}Be β decay, $I_\gamma^{abs}(2125\text{ keV}) = (35.5 \pm 1.8)\%$ [89], a new result is calculated for the β feeding of the first excited state of ^{11}Be, $I_\gamma^{abs}(320\text{ keV}) = (12.6 \pm 1.3)\%$.

Within the limits of uncertainty all the independent values given above for $I_\gamma^{abs}(320\text{ keV})$ are in agreement. This fact proves that the β-delayed charged-particle emission in the ^{11}Be decay is quantitatively well understood. Since the result from the direct measurement at ISOLDE is more precise and does not depend on other experimental values for absolute and relative γ-intensities, we will adopt the value $I_\gamma^{abs}(320\text{ keV}) = (10.6 \pm 0.4)\%$ for further discussion.

The first three experimental values for $I_\gamma^{abs}(320\text{ keV})$ presented in Table 4.2 all depend on the absolute intensity of the 2125 keV γ line in the ^{11}Be β decay. As mentioned above, different values for this latter intensity were used in the various calculations. By combining our experimental results for the β-delayed charged-particle emission with the relative γ-intensity, $\frac{I_\gamma^{rel}(478\text{ keV})}{I_\gamma^{rel}(2125\text{ keV})} = 0.0066(5)$, an independent value for $I_\gamma^{abs}(2125\text{ keV}) = (41 \pm 4)\%$ is derived. To obtain this result we used the total ^{7}Li + α branching and the relative feeding of the ^{7}Li(478 keV) + α channel in the ^{11}Be β decay. This result is larger than the literature value but the two numbers still coincide within the limits of uncertainty.

A crucial factor in the calculation of the total ^{7}Li + α branching ratio (and hence $I_\gamma^{abs}(320\text{ keV})$) is the purity of the ^{11}Li beam at TRIUMF. Especially the presence of directly produced ^{11}Be ions is critical. The ion source that was used in the experiment had negligible efficiency for surface ionizing Be, B and C. These three elements were also badly released from the target. The only possible process that can create such Be, B or C beams is through electrons liberated by photons out of the electrode in front of the ion source and thus flying towards the ion source with some keV energy equivalent. This possible contamination could be deduced by using the large mass difference between the mass 11 isobars and the high mass-resolving power of the isotope separator. For ^{11}Li and ^{11}Be the ratio $\frac{M}{\Delta M} \sim 500$ which is about a factor 20 smaller than the mass resolution of the separator. The mass separator was tuned to the mass of ^{11}Be and no measurable activity was observed in the DSSSD. This was confirmed by the observations in the study of the $p(^{11}\text{Li},^9\text{Li})t$ reaction using the active target detector MAYA [114]. In this experiment at TRIUMF they also used a post-accelerated ^{11}Li beam (in this case an extra acceleration stage was used; ISAC-2) and possible contamination would have been really easy to spot.

In the study of the β decay of ^{11}Li described in [93] a ^{11}Be contribution of 7.3(18)% in the 60 keV A =11 ISOLDE beam was reported. This calculation

was performed using the absolute ^{11}Be γ intensity I_γ^{abs}(2125 keV) = (35.5 ± 1.8). When the intensity of (41 ± 4)% for this γ line is used to evaluate the experimental $\frac{I_\gamma^{rel}(320\text{ keV})}{I_\gamma^{rel}(2125\text{ keV})}$ ratio together with the new value for I_γ^{abs}(320 keV) = (10.6 ± 0.4)%, a ^{11}Be contamination of 8.0(8)% is found. This all would imply that they overestimated the number of betas with a factor 1.4 .

The β feeding to the first excited state at 320 keV in ^{11}Be contains valuable information about the halo structure of the mother nucleus ^{11}Li. First a log(ft) value for this transition corresponding to the branching ratio of (10.6 ± 0.4)% is calculated to be equal to 5.484(19). The decay half life $T_{1/2}$ = 8.5(2) ms [84] and total Q-value = 20551(1) keV [83] were used in this calculation together with the parametrization for the β-decay phase space factor, f, given in Appendix A.5.1. With this log(ft) value corresponds a reduced Gamow-Teller transition probability $B(GT)$ = 0.014, according to equation 4.7. In a first publication Suzuki and Otsuka [115] studied the effect of the ^{11}Li neutron halo on the one-body transition matrix elements as well as on two-body meson exchange currents. At the time of publication, 1994, the observed log(ft) = 5.58 [35] was larger than the calculated values obtained by using the Cohen-Kurath interactions [116] with harmonic oscillator (HO) wave functions and by taking into account only one-body terms: log(ft) = 4.59 - 4.80. Suzuki and Otsuka start with the assumption that neutrons of ^{11}Li are not excited into the *sd*-shell. Shell-model calculations are performed with single-particle wave functions consistent with the neutron separation energy. For the latter they used the value S_n = 160 keV, which is half of the average value of S_{2n} = 295 keV [117] and S_{2n} = 340 keV [84]. The calculation takes into account the spatial extension of the wave functions of the halo neutrons in the form of a Woods-Saxon wave function for $\nu p_{1/2}$. The decay to the ^{11}Be first excited state is dominated by the $\nu p_{1/2} \rightarrow \pi p_{3/2}$ transition. The other three out of four components of the GT transition matrix element in the *p*-shell, $\nu p_{1/2} \rightarrow \pi p_{1/2}$, $\nu p_{3/2} \rightarrow \pi p_{1/2}$ and $\nu p_{3/2} \rightarrow \pi p_{3/2}$, however cancel a large part of this contribution. Therefore the halo reduces the GT matrix element by 35 - 43%, depending on the different Cohen-Kurath interactions that were used. This reduction brings the theoretical log(ft) value closer to the experimental value.

The above halo effect is however not large enough to account for the experimentally observed retardation of the transition. The shell-model configuration space is hence extended as to include the *sd*-shell. Effects of the excitation of valence particles into this shell were investigated by using the Millener-Kurath interaction [118, 119]. Excitations of up to 2 valence particles in the *sd*-shell result in the increase of the log(ft) value by 0.08 - 0.12, depending on the interaction that was used. The addition of one-pion exchange currents due to Δ_{33}-isobar excitations leads to a reduction of the GT matrix element to $\sim$ 85% of its original value, even if the halo structure is neglected. It was concluded in [115] that the halo, the exchange currents and the mixing of the *sd*-shell con-

figuration contribute coherently to the retardation of the transition ^{11}Li(g.s., $\frac{3}{2}^-$) $\rightarrow$ ^{11}Be*(320 keV, $\frac{1}{2}^-$): the log(ft) is increased by 0.9 $\sim$ 1.0.

Triggered by the experimental results from Borge et al. at ISOLDE [93] and Aoi et al. at RIKEN [97], Suzuki and Otsuka presented a new study of the ^{11}Li GT transitions related to the structure of this isotope [120]. These experiments suggest a stronger retardation of the ^{11}Li(g.s.,$\frac{3}{2}^-$) $\rightarrow$ ^{11}Be*(320 keV,$\frac{1}{2}^-$) transition than before [35]: log(ft) values of 5.67 $\pm$ 0.04 [97] and 5.73 $\pm$ 0.03 [93] were obtained. Whereas in the first paper [115] single-particle halo wave functions were only used for the $\nu p_{1/2}$ neutron orbital, now the same was done for the $\nu 2s_{1/2}$ orbital. Again the Woods-Saxon potentials were fitted to the observed neutron separation energies. For the other orbitals HO wave functions were used and the following overlaps were obtained: $\langle \pi p | \nu p_{1/2} \rangle$ = 0.85 and $\langle \pi 2s_{1/2} | \nu 2s_{1/2} \rangle$ = 0.625.

A major issue with respect to the two-neutron halo in ^{11}Li is to what extend the $(1p_{1/2})^2$ and $(2s_{1/2})^2$ configurations are included. In their study Suzuki and Otsuka change the $\nu p_{1/2}^2$ contribution by lowering the single-particle energy of the $2s_{1/2}$ orbit and looking at the variation of the calculated log(ft) values. Figure 4.23 shows their result, the log(ft) value as a function of the pure p-shell configuration $P(p^7)$ (6 valence neutrons and 1 valence proton are placed in the $1p$ orbits outside a core of filled $1s$ orbits), together with three experimental results [35, 93, 97] and our new result (dotted line). The changes of the single-particle energy of the $2s_{1/2}$ orbit are denoted in the figure. In part (a) of the figure the $2s_{1/2}$ neutron orbit also forms a halo in addition to the $\nu p_{1/2}$ orbit while in (b) a HO wave function is taken for the $2s_{1/2}$ orbit. This latter approach is corresponding to the calculations in their previous paper [115]. From the little difference between (a) and (b) it was concluded that for the log(ft) value it is irrelevant whether the $\nu 2s_{1/2}$ orbit is a halo orbit or not. It should be noted that $P(p^7)$ is actually the probability of the $\nu p_{1/2}^2$ configuration for the last two neutrons. The authors point out that the log(ft) is determined predominantly by $P(p^7)$ and is not affected by details of the excited configuration: it is irrelevant whether two or four valence particles are excited into the *sd*-shell. When both $\nu p_{1/2}$ and $\nu 2s_{1/2}$ orbits have the halo structure, corresponding to part (a) of Figure 4.23, $P(p^7)$ turns out to be 46, 55 and 70%, corresponding to a lowering of the single-particle energy of the $2s_{1/2}$ orbit of 3.245, 3.185 and 3.035 MeV in [93], [97] and [35], respectively.

Our experimental result for the ^{11}Li(g.s., $\frac{3}{2}^-$) $\rightarrow$ ^{11}Be*(320 keV, $\frac{1}{2}^-$) transition, log(ft) = 5.484(19), corresponds to a nearly pure p-shell configuration in the ^{11}Li nucleus based on the calculation of Suzuki and Otsuka [120]. Other experimental observations however show qualitative indications of a substantial $(2s_{1/2})^2$ contribution in the ^{11}Li neutron halo. For example, from the observation of charged particles emitted in the ^{11}Li decay, β feeding to an excited state

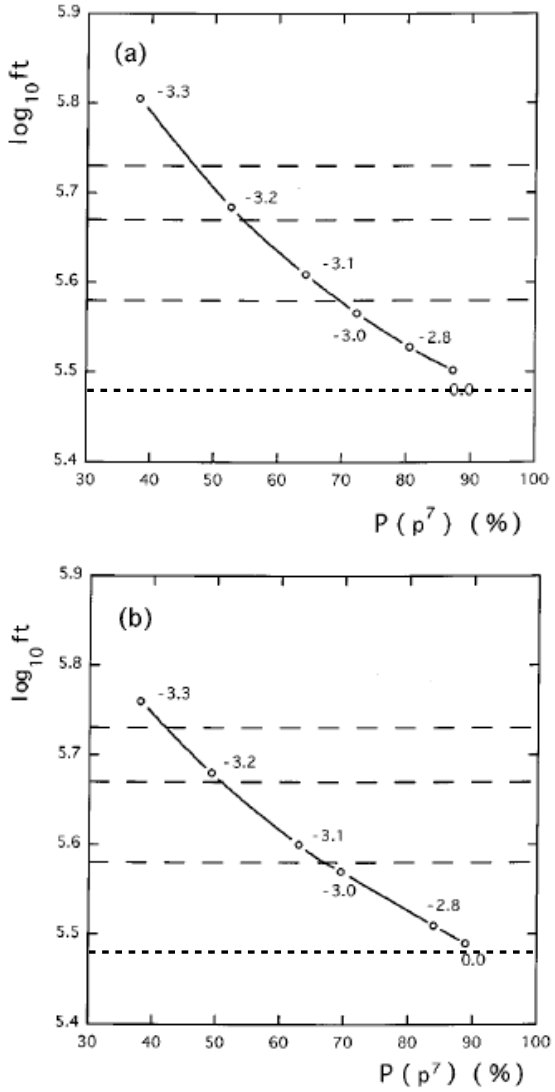

Figure 4.23: Log(ft) values of the GT transition ^{11}Li(g.s.,$\frac{3}{2}^-$) $\rightarrow$ ^{11}Be*(320keV,$\frac{1}{2}^-$) vs. the probability of the pure p-shell configuration, $P(p^7)$. Dashed lines show the observed log(ft) values: log(ft) = 5.73 $\pm$ 0.03 [93], 5.67 $\pm$ 0.04 [97], 5.58 $\pm$ 0.03 [35], whereas the dotted line represents our new result 5.484 $\pm$ 0.019. Numbers denoted in the figure correspond to the energy in MeV with which the single-particle $2s_{1/2}$ orbit is lowered. (a) $\nu 2s_{1/2}$ as well as $\nu p_{1/2}$ are halo orbits. (b) Only $\nu p_{1/2}$ is a halo orbit. Figure taken from [120].

at 18.15(15) MeV in ^{11}Be (see Figure 4.4) with a large GT strength, $B(GT) \geq 1.6$, has been observed [92, 121]. A striking result of this experiment was the strong suppression of the neutron branch from this state to the 0^+ ground state in ^{10}Be. This channel, with the largest decay energy, has a partial width less than 3×10^{-3}. The reason for this is connected to the structural features of the state around 18 MeV and the mother nucleus ^{11}Li. Due to the negative parity of the excited state in ^{11}Be fed via an allowed transition and parity conservation, only p-wave neutrons may be emitted into the $^{10}\mathrm{Be}_{g.s.}$ + n decay channel of ^{11}Be*. Hence a very small admixture of this configuration should be present in the wave-function of the excited ^{11}Be state. The large strength of the β transition implies a broad overlap of this state and the ground state of ^{11}Li. If the assumption is made that only ^{11}Li halo neutrons participate in the particular GT β transition, the contribution of $\nu p^2_{1/2}$ configuration should be very small. Another evidence for strong mixing of the *sd*-shell configuration in the ^{11}Li halo is found in the observation of the magnetic moment of this nucleus in comparison with theory. With the unchanged single-particle energies for the neutron *sd* orbits, corresponding to 89% probability of the $p^2_{1/2}$ configuration, Suzuki and Otsuka [115] calculated a value of 3.90 nm. When the $p^2_{1/2}$ configuration probability is changed to 63%, according to [35], the calculated magnetic moment becomes 3.76 nm and gets closer to the observed value: 3.67 nm [122].

4.5.2 β decay of ^{11}Be: a new state at 11.56 MeV in ^{11}B

From the R-matrix analysis of the energy spectra of the charged-particle emission in the β decay of ^{11}Be, measured both at TRIUMF and ISOLDE, we concluded that mainly two states above the ^{7}Li + α threshold are involved in this decay channel. One of these ^{11}B states is a well known resonance at 9.876(8) MeV. This state has been observed in numerous experiments using different reactions: ^{7}Li(α,α')^{7}Li*(478 keV) [86, 87, 123–125], ^{7}Li(α,α)^{7}Li [86], ^{9}Be(^{3}He,p)^{11}B [112, 126], ^{10}B(d,p)^{11}B [126] and ^{12}C(^{10}Be,^{11}B*)^{11}B [127]. The spin-parity $J^\pi = \frac{3}{2}^+$ was suggested by Cusson [86] and confirmed by Paul [87] by performing an analysis of the data on elastic and inelastic α scattering on ^{7}Li, based on the R-matrix theory. From Figures 4.10 and 4.21 the interference of this state with a higher-lying $\frac{3}{2}^+$ state was suggested. This idea was confirmed by the R-matrix analysis which gave the best fit result when the state around 9.88 MeV was found to be interfering with a state just above the Q-value of 11.506(6) MeV.

The fit on the ISOLDE energy spectrum results in a state at an energy E_x = 11.56(3) MeV, where the result of Table 4.12 is corrected for the β summing of 12 keV, as explained in Chapter 2. In this energy region in ^{11}B, presently two candidates are tabulated in literature: one state at 11.444(19) MeV, the other

at 11.600(30) MeV, see Table 4.5. The first state around 11.44 MeV has been observed in several reaction experiments: ^{7}Li(α,α')^{7}Li*(478 keV) [86, 124], ^{7}Li(α,α)^{7}Li [86] and in [126] with reactions ^{9}Be(^{3}He,p)^{11}B and ^{10}B(d,p)^{11}B. No spin-parity assignment has been coupled to this state. The second state around 11.60 MeV was found in the following experiments: ^{7}Li(α,α')^{7}Li*(478 keV) [86, 124], ^{7}Li(α,α)^{7}Li [86] and in [128, 129] with reactions ^{10}B(n,α)^{7}Li and ^{10}B(n,α')^{7}Li*(478 keV). From the analysis of the last two reactions, a spin-parity $J^{\pi} = \frac{5}{2}^{+}$ was assigned to a very weak resonance at $E_{\mathrm{n}} = 170$ keV, corresponding to an energy of 11.61 MeV in ^{11}B. When this state was removed from the theoretical R-matrix function, reasonable fits were obtained and the results for the other states remained the same, indicating the weak presence of this state. Finally, from the analysis of the ^{12}C(^{10}Be,^{11}B*)^{11}B reaction Ahmed et al. suggest the presence of a ^{11}B state at $\sim$ 11.5 MeV [127]. It is clear that we cannot uniquely identify this state with one of the states presently tabulated in literature. However, the shape of our decay energy spectra and the results of the R-matrix analysis strongly suggest the existence of a $J^{\pi} = \frac{3}{2}^{+}$ state in ^{11}B at an energy around the Q-value for ^{11}Be β decay.

Teeters and Kurath studied the positive-parity states of ^{11}B in a complete $1\hbar\omega$ representation using the weak coupling model [130]. Appropiate interactions were taken for the $1p$-shell [116], the $1p$-sd particle-hole interaction from [118] and the $1s$-$1p$ and $1s$,sd-$(1p)^2$ matrix elements from [131]. The ten positive-parity states identified below 12 MeV (see Table 4.5 with exception of two states at 6.7918(3) MeV ($\frac{1}{2}^{+}$) and 7.28551(43) MeV ($\frac{5}{2}^{+}$) [84]) all have representatives in the calculated states, see Figure 4.24. However, one extra $\frac{3}{2}^{+}$ state was calculated. A remarkable feature of the calculation is that the calculated $\frac{3}{2}^{+}$ levels are in much worse agreement with experiment than the other J-values. This can be seen in Figure 4.25 where the states with $J \leq \frac{9}{2}$ are compared with experiment. The calculated $\frac{3}{2}^{+}$ levels lie about 1.5 MeV above the observed levels. According to the authors this suggests a modification of the particle-hole interaction. Maybe the $\frac{3}{2}^{+}$ state found in the R-matrix analysis at 11.56(3) MeV corresponds to one of the states produced by the calculation that can be seen in Figure 4.25. This is of course suggestive but keeping in mind the agreement between experimental states with other J-values, it is likely the expect the existence of at least one extra $\frac{3}{2}^{+}$ state above the one at 9.876 MeV.

For the mirror nucleus ^{11}C ($Z = 6$, $N = 5$) only one $\frac{3}{2}^{+}$ state at 7.4997 MeV is tabulated which is the analogue state of the ^{11}B $\frac{3}{2}^{+}$ state at 7.97784(42) MeV [84]. So, presently no analogue states in ^{11}C have been observed for the states around 9.88 MeV and 11.56 MeV in ^{11}B.

The spectroscopic factors for the positive-parity states in ^{11}B are also presented in [130] relative to the ^{10}B ($J^{\pi} = 3^{+}$, $T = 0$) and ^{10}Be ($J^{\pi} = 0^{+}$, $T = 1$) ground states, to 6 excited $T = 0$ and two 2^{+} excited $T = 1$ ^{10}B states.

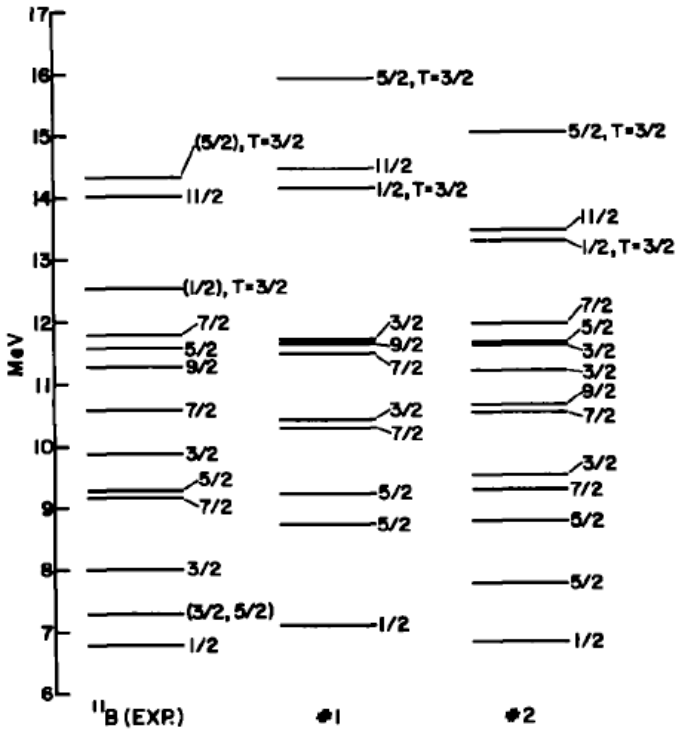

Figure 4.24: Positive-parity states for ^{11}B. Experimental states are shown on the left, spectra calculated with two sets of single-particle energies in subsequent columns. The energies of the *sd* orbits in the first set are lowered by 1 MeV in the second set, whereas the 1*s* orbit is lowered by 5 MeV. Only yrast levels are given above 12 MeV. Figure taken from [130].

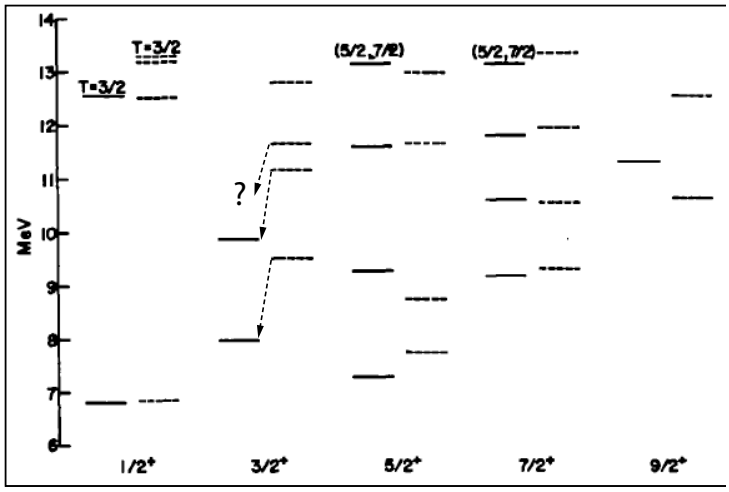

Figure 4.25: Positive-parity states for ^{11}B up to 13.5 MeV excitation energy for $J \leq \frac{9}{2}$ separated according to J. Solid lines correspond to the levels observed in experiments, dashed lines to levels calculated with the second set of single-particle energies (see Figure 4.24). The calculated $\frac{3}{2}^+$ states lie about 1.5 MeV above the observed levels, indicated by the dashed arrows. The third calculated $\frac{3}{2}^+$ level has not been experimentally observed yet but might correspond to the state that was found in the R-matrix analysis of the TRIUMF and ISOLDE data (more info in text). This is represented by the question mark in the figure. Figure taken from [130].

Also components involving coupling of a $1s$ hole to the ground or first excited state of ^{12}C were considered. The total intensity contained in all these contributions lies between 75% and 95% except for the $\frac{3}{2}^+$ state experimentally found around 9.88 MeV which shows only 64%. The spectroscopic factors for the extra calculated $\frac{3}{2}^+$ state were not given because they were too small. The $\log(ft)$ values for allowed β transitions are calculated in the same framework. Contributions to the matrix element resulting from a transition of the *sd* neutron to a *sd* proton and from transitions between core states of the initial and final state were taken into account. The main contribution comes from the ^{11}Be component where the ^{10}Be ($J^\pi = 0^+$, $T = 1$) is coupled to a $2s$ neutron, since there are strong transitions to the ^{10}B ($J^\pi = 1^+$, $T = 0$) core components of the final state. For the allowed β transition to the $\frac{3}{2}^+$ state around 9.88 MeV these contributions all add constructively, resulting in a $\log(ft)$ value of 4.03. This result is in good agreement with the early experimental value of (4.04 ± 0.08 [89]) and our value of (4.065 ± 0.015, see Table 4.13).

4.5.3 Relative feeding of ^{7}Li + α channels in the β decay of ^{11}Be

The wave functions of [130] were used in [88] to calculate the relative feedings of the ^{7}Li + α and ^{7}Li(478 keV) + α channels from the $\frac{3}{2}^+$ state around 9.88 MeV in ^{11}B. They found that the decay branch via ^{7}Li in its first excited state was $\sim 24\%$ of the total, a result that was found to be in reasonable agreement with their experimental value of $(12.6 \pm 1.2)\%$. By looking at the ^{11}Be β-decay energy spectra measured at TRIUMF and ISOLDE and the corresponding R-matrix fit parameters, our results are in disagreement with both these values. As mentioned above, from the analysis of the spectrum taken at ISOLDE with the higher statistics we obtain 92.0(4)% and 8.0(4)% for the ^{7}Li + α and ^{7}Li(478 keV) + α channels, respectively. This results is obviously in strong disagreement with the observation of Cusson [86]. In his paper he obtained a ratio of widths of the two channels $\Gamma_I/\Gamma_E = 4.0$. Here Γ_E and Γ_I correspond to the width of the state as observed in the ^{7}Li(α,α)^{7}Li and ^{7}Li(α,α')^{7}Li*(478 keV) reactions, respectively. This result however was calculated by using a rather large value for the ^{7}Li + α channel, $R = 6$ fm, which he was forced to use to connect the data from both reactions.

The R-matrix analysis in this work has been performed using a ^{7}Li + α channel radius of 4.96 fm. The reduced widths of the two channels for the state around 9.88 MeV both exceed the Wigner limit of 0.668 MeV (see A.60) by a factor of 2.3 (^{7}Li(g.s.) + α) and 1.4 (^{7}Li(478 keV) + α) as calculated from the results presented in Table 4.12. Those values indicate that it is not impossible that the state around 9.88 MeV has a ^{7}Li + α cluster-type configuration. These high-energy states are rather difficult to deal with from a theoretical point of

view. An effort to define the structure of the $\frac{3}{2}^+$ states in this energy region in ^{11}B has been made by Yamada [132] in $\alpha + \alpha + t$ OCM (Orthogonality Condition Model) with the Gaussian expansion method. This model has a huge model space describing the $\alpha + \alpha + t$ gas-like states, ^{7}Li + α cluster states and ^{8}Be + t cluster states as well as the shell-model-like ground state. The first $\frac{3}{2}^+$ state around E_x = 7.98 MeV is predicted at the correct energy and believed to have a dominant cluster structure of ^{7}Li(g.s., $\frac{3}{2}^-$) + α with the relative P-wave orbital motion of the α particle. The second $\frac{3}{2}^+$ state appears as a resonant state with E_x = 10.0 MeV and width = 50 keV in his calculation. The structure of this state has a mixed cluster structure of ^{7}Li(g.s) + α (P-wave, F-wave) and ^{7}Li*($\frac{1}{2}^-$) + α. Our experimental result for the total width of this state, Γ = 274(10) keV (see Table 4.12) is in strong disagreement with this calculation. The third $\frac{3}{2}^+$ state that was suggested from our experimental results from the experiments at TRIUMF and ISOLDE at an excitation energy of 11.56(3) MeV, is calculated at an energy E_x = 10.8 MeV with a width of 250 keV. This state is likely to have a ^{7}Li(g.s) + α cluster structure with the dominant F-wave relative orbital motion of the α particle. Although the results for the width of this state are again not in agreement, the presence of a third $\frac{3}{2}^+$ state seems to be very likely. Future studies on the structure of ^{11}B states, and boron isotopes in general, with respect to clustering will certainly get much interest since they are situated in between the beryllium and carbon nuclei. Well developed cluster structures and evidence of molecular-like structures are found in several beryllium [133–135] as well as in carbon isotopes [136–138].

4.5.4 The halo decay of ^{11}Be

In Chapter 1 it was suggested with equation 1.4 that in halo nuclei the halo particle(s) and the core might decay independently from each other due to their large spatial separation. This hypothesis can now be tested and discussed for the β decay of ^{11}Be in a simple picture. To a good approximation, the ground state of this nucleus can be described as an s-wave neutron around a ^{10}Be core and so the β decay of ^{10}Be ($J^\pi = 0^+$) should be considered. The only energetically allowed decay mode is a second forbidden transition to the 3^+ ground state of ^{10}B, see Figure 4.26. From the ^{10}C mirror decay however, also illustrated in Figure 4.26, we would expect large decay strengths to the 1^+ excited state at 0.718 MeV ($B(GT)$ = 3.44) and to the isobaric analogue state at 1.740 MeV ($B(F)$ close to 2) [32]. The isobaric analogue state in ^{11}B at 12.56 MeV cannot be populated in the β decay of ^{11}Be since the Q_β-value is 11.506(6) MeV. Contributions from the 'core' decay in equation 1.4 will hence correspond to a configuration where the 1^+ excited ^{10}B state is coupled to an s-wave neutron. Experimental evidence exists that the ^{10}B ground state plus s-wave neutron configuration is spread out over several states in ^{11}B from 9.2

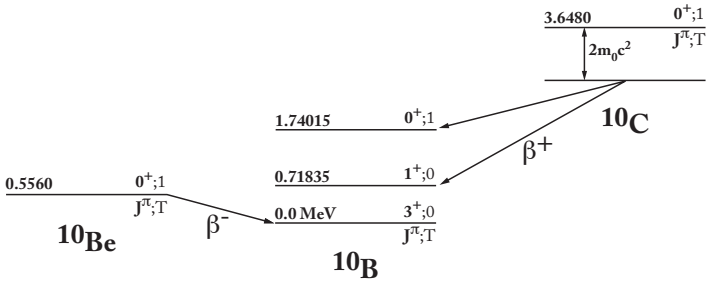

Figure 4.26: β decay scheme of the ^{10}Be core of the ^{11}Be halo nucleus and the mirror nucleus ^{10}C.

MeV to 12 MeV [128]. The situation for the excited state configuration might be similar since, before the experimental results presented in this work, it was believed that only the state in ^{11}B at 9.876 MeV was fed in the ^{11}Be β decay. The remaining strength of this configuration, as well as from the ^{10}Be plus proton part ('halo decay') was suggested to be situated at an excitation energy of 11 - 12 MeV. Our final experimental result for the feeding of states in ^{11}B presented in Table 4.13 correspond to $B(GT)$ values of 0.33 for the state at 9.876 MeV and 2.60 for the new state at 11.56 MeV. Hence, according to the results presented here part of the missing Gamow-Teller strength can indeed be found in the suggested energy region.

4.5.5 The ^{8}Li + t channel in the ^{11}Li β decay

In the first part of the beam off period of the TRIUMF experiment where ^{11}Li ions were implanted in a 20 s - 20 s beam on-beam off modulation, a signature of the emission of 2α particles in the β decay of ^{8}Li was observed. Hence, the ^{8}Li + t channel in the ^{11}Li β decay could be investigated in section 4.3.1. Given the ^{8}Li + t threshold in ^{11}Be at an energy of 15.723 MeV [84], this decay channel has a Q-value of $\sim$ 4.9 MeV and is fed via the resonance state around 18 MeV (see Figure 4.4). The β-delayed triton emission for ^{11}Li has been observed for the first time by Langevin et al. [38]. They reported a branching ratio of for tritons above 800 keV of $1(4)\times10^{-4}$. Later a branching ratio of $1.2(1)\times10^{-4}$ was observed [39, 92, 121]. A more recent experiment reports a value of $1.4(3)\times10^{-4}$ [139]. In [45] Raabe et al. obtained a branching ratio for the ^{9}Li + d channel to be $1.30(13)\times10^{-4}$. By performing a similar analysis for the ^{8}Li + t channel a branching ratio of $2.15(17)\times10^{-4}$ was obtained. With the data and procedure presented in section 4.3.1, this work gives a value of $2.59(27)\times10^{-4}$ in agreement with the value obtained by Raabe et al. . This

means that in the ^{11}Li β decay a larger branching to the ^{8}Li + t channel than to the ^{9}Li + d channel is present. The same qualitative result was derived from a charge-exchange reaction experiment with ^{11}Li nuclei where the authors concluded that in the β decay of ^{11}Li, the yield of the deuterons should be one order of magnitude less than the triton yield [140].

Intuitively a smaller branching ratio than for the ^{9}Li + d channel is expected for the ^{8}Li + t channel in the ^{11}Li β decay. The ^{11}Li nucleus can be described very well as a ^{9}Li core surrounded by two valence neutrons and the overlap with the final state ^{9}Li + d is expected to be large, whereas the overlap with the triton emission channel is expected to be much smaller. Presently no theoretical calculations have been performed on the branching ratio for the ^{8}Li + t channel. The larger value of this decay branch with respect to the deuteron emission channel might be related to the structure of the state around 18 MeV in ^{11}Be. Since this is a state at high excitation energy where all decay channels presented in Table 4.1 are open, it will be very difficult for any theoretical model to obtain quantitative information related to the ^{8}Li + t emission channel.

Conclusions and outlook

The β decay of the halo nuclei, ^{6}He, ^{11}Be and ^{11}Li has been studied using an implantation technique with a thin segmented silicon detector (DSSSD). Precise absolute branching ratios and accurate energy spectra of β-delayed charged-particle emission channels were obtained that contribute to a better understanding of nuclear structure of both mother and daughter states. All these measurements were performed with post-accelerated radioactive ISOL beams at different experimental facilities.

The advantages of the calorimetric method, where implantations and charged-particle emissions are observed in one small detector volume, are fully exploited in this work. Thanks to a good overall normalization of the decay channels and the reduction of pure β signals it is possible to study weak decay modes up to low energies. The β suppression has been investigated both qualitatively and quantitatively by applying different energy thresholds and detector strip multiplicity conditions in the off-line analysis. GEANT4 simulations on the effect of β summing were performed in order to come to a more complete mastering of the detection technique.

In a series of experiments at the CRC facility in Louvain-la-Neuve the β-delayed $\alpha + d$ emission in the ^{6}He decay has been studied. The absolute branching ratio $\bar{B} = (1.65 \pm 0.10) \times 10^{-6}$ for a deuteron energy $E_d \geq 350$ keV was measured with an uncertainty that was drastically reduced from 50% to 6%. This value confirms the need for a cancellation effect between two separate regions of the spatial integral in the Gamow-Teller matrix element and asks for a complete theoretical description of the ^{6}He ground state wave function up to very large distances in order to be reproduced. The observed energy dependence of the transition probability also requires the three-body asymptotic behavior of this wave function. Future experiments on this ^{6}He decay channel should aim to extend the charged-particle spectrum down to lower energies to guide fully consistent parameter-free theoretical models to a correct treatment of the ^{6}He and $\alpha + d$ wave functions.

At the TRIUMF facility in Vancouver a post-accelerated ^{11}Li beam was implanted in the DSSSD. By choosing appropriate time windows for the ra-

dioactive ion implantation and the observation of the subsequent β decays, the feeding of bound ^{11}Be states as well as the ^{7}Li + α emission channels in the decay of the latter nucleus could be investigated. To disentangle the results for both ^{11}Li and ^{11}Be β decays, a complementary experiment at ISOLDE in Geneva was performed where ^{11}Be ions were directly implanted in the detector. The branching ratio for the allowed transition to the first excited state at 320 keV in ^{11}Be, $I_{\gamma}^{abs}(320\ keV) = (10.6 \pm 0.4)\%$, was found to be in disagreement with the average literature value by a factor 1.4 . Based on a shell-model calculation from 1997 our experimental result corresponds to a pure *p*-shell configuration of the ^{11}Li neutron halo, in contradiction with other observations where a strong signature of *sd*-shell contribution is inferred. New experiments should carefully check the purity of the ^{11}Li beam when this branching ratio will be measured again. The α branching in the β decay of ^{11}Be was measured directly in the ISOLDE experiment, $I_{^{7}Li+\alpha}^{abs} = (3.47 \pm 0.12)\%$, and found to be in agreement with the present literature value. From the R-matrix analysis of the ^{7}Li + α energy spectrum a new $\frac{3}{2}^{+}$ state at 11.56 MeV in ^{11}B is found that interferes with the known state at 9.876 MeV in the β-delayed α emission. The relative feedings of the ^{7}Li(g.s.) + α (92.0(4)%) and ^{7}Li(478 keV) + α (8.0(4)%) channels do not confirm the literature values. The reduced widths for the two channels suggest a cluster-type configuration for the state at 9.876 MeV and might trigger theoretical studies concentrating on clustering in this mass region. The branching ratio for ^{8}Li + t channel in the ^{11}Li β decay could be measured in the TRIUMF experiment to be $2.59(27)\times10^{-4}$. This value is in agreement with the result that was obtained in the same experimental campaign using a time and position correlation technique that was also used to study the ^{9}Li + d channel. Unexpectedly this latter decay mode was found to be weaker than the triton emission channel and this result might contain interesting structure information about high-lying states in ^{11}Be.

Besides the β decays of the three nuclei described above, also the ^{9}Li and ^{8}Li decays were studied with the implantation technique using post-accelerated beams at TRIUMF. Furthermore, ^{12}N and ^{12}B beams at KVI in Groningen were implanted to study ^{12}C states above the triple α threshold, which is of importance in the field of nuclear structure as well as in the field of nuclear astrophysics [141–143]. The two α emission in the ^{8}B β decay was measured at the same facility using a fragmentation beam in order to compare the neutrino spectrum with the one measured directly from the sun to study the neutrino oscillations. The analysis of this experiment is ongoing.

The implantation technique with a thin highly pixilated detector can in principle be used in every decay involving charged-particle emission which opens the possibility to study a lot of physics cases with different interest. The exact knowledge of the number of implanted nuclei, the low energy threshold for the detection of decay events and the fact that only one detector is used, hereby

avoiding relative efficiency problems of different detectors, are the main advantages of this technique that can be fully exploited in future experiments. For example, the $^{12}C(\alpha,\gamma)^{16}O$ reaction rate that is important in the He-burning process in stellar evolution can be studied by measuring the β decay of ^{16}N, analogue to the experiments at KVI concentrating on states in ^{12}C. Also, channels that have been observed before in the β decay of ^{8}He and ^{14}Be can be remeasured trying to improve on the present knowledge of these neutron rich systems. At higher nuclear masses α decay and electron capture delayed fission can be studied with the technique presented in this work if appropriate electronic amplifications chains are constructed for the detection of both implantation and decay events.

In conclusion, this thesis provides accurate, calorimetric measurements of β-delayed charged-particle emission channels that give valuable information on the structure of light exotic nuclei and on the other hand open questions for future research.

Appendix A

R-matrix formalism

In Chapter 4 the charged-particle emission following the β decay of ^{11}Be is discussed. The experimental energy spectrum is analysed using the R-matrix theory. In this Appendix the framework for this analysis is built up and explained.

A.1 The collision matrix

The starting point in deriving the R-matrix cross sections and β-decay probabilities is the collision matrix given in [106] (VII 1.5). In matrix notation,

$$\mathbf{U} = \mathbf{\Omega W \Omega}, \tag{A.1}$$

where $\mathbf{U}$ and $\mathbf{W}$ are matrices with dimension equal to the number of scattering or decay channels, and $\mathbf{\Omega}$ is a vector with unit-modulus complex numbers as entries:

$$\Omega_c = e^{i(\omega_c - \phi_c)}, \tag{A.2}$$

where ω_c is the Coulomb phase shift and $-\phi_c$ is the hard-sphere scattering phase shift (the phase shift induced by an infinitely repulsive sphere of radius a_c). The $\mathbf{W}$-matrix is, from [106] (VII 1.6),

$$\mathbf{W} = \mathfrak{P}^{1/2}(\mathbf{1} - \mathbf{R}\mathbf{L}^0)^{-1}(\mathbf{1} - \mathbf{R}\mathfrak{L}^0)\mathfrak{P}^{-1/2} \tag{A.3}$$

$$= \mathbf{1} + \mathfrak{P}^{1/2}(\mathbf{1} - \mathbf{R}\mathbf{L}^0)^{-1}\mathbf{R}\mathfrak{P}^{1/2}\mathbf{w}. \tag{A.4}$$

The following definitions have been used (positive-energy channels):

$$\mathbf{L}^0 = \mathbf{L} - \mathbf{B}, \tag{A.5}$$

$$\mathfrak{L}^0 = \mathfrak{L} - \mathbf{B}, \tag{A.6}$$

$$\mathfrak{L}_c = L_c^*, \tag{A.7}$$

$$\mathfrak{P}_c = P_c, \tag{A.8}$$

$$w_c = 2i. \tag{A.9}$$

L_c is the logarithmic derivative of the wave function,

$$L_c = S_c + iP_c \tag{A.10}$$

with real and imaginary parts known as the shift function and penetrability respectively. B_c is the boundary condition on the logarithmic derivative. The **R**-matrix has components

$$R_{cc'} = \sum_{\lambda} \frac{\gamma_{\lambda c}\gamma_{\lambda c'}}{E_\lambda - E} \tag{A.11}$$

The components of **W** (equation A.3) are

$$W_{cc'} = P_c^{1/2} \sum_{c''} (\mathbf{1} - \mathbf{RL}^0)^{-1}_{cc''} (\delta_{c''c'} - R_{c''c'} L^{*0}_{c'}) P_{c'}^{-1/2}, \tag{A.12}$$

so in component form the collision matrix is

$$U_{cc'} = e^{i(w_c + w_{c'} - \phi_c - \phi_{c'})} P_c^{1/2} P_{c'}^{-1/2} \sum_{c''} (\mathbf{1} - \mathbf{RL}^0)^{-1}_{cc''} (\delta_{c''c'} - R_{c''c'} L^{*0}_{c'}). \tag{A.13}$$

Using the alternative form (A.4) you get

$$U_{cc'} = e^{i(w_c + w_{c'} - \phi_c - \phi_{c'})} \left(\delta_{cc'} + 2iP_c^{1/2} P_{c'}^{1/2} \sum_{c''} (\mathbf{1} - \mathbf{RL}^0)^{-1}_{cc''} R_{c''c'} \right). \tag{A.14}$$

A.1.1 Level-matrix form of the collision matrix

For systems with many channels, c, the problem of inverting the channel-matrix, $\mathbf{1} - \mathbf{RL}^0$, may be replaced by the inversion of a level-matrix, $\mathbf{A}^{-1}$, with the number of rows and columns equal to the number of levels. The level-matrix form of the collision matrix is, in component form:

$$U_{cc'} = e^{i(w_c + w_{c'} - \phi_c - \phi_{c'})} \left(\delta_{cc'} + 2iP_c^{1/2} P_{c'}^{1/2} \sum_{\lambda\lambda'} \gamma_{\lambda c}\gamma_{\lambda' c'} A_{\lambda\lambda'} \right) \tag{A.15}$$

A solution for $\mathbf{A}^{-1}$ can be found by assuming the equality of formulas (A.14) and (A.15):

$$A^{-1}_{\lambda\lambda'} = \delta_{\lambda\lambda'}(E_\lambda - E) - \sum_c \gamma_{\lambda c}\gamma_{\lambda' c}(S_c - B_c + iP_c) \tag{A.16}$$

A.2 Scattering cross section

The integrated scattering cross section for an incident particle of type α with spin s, and outgoing type α' and spin s', is given in [106] VIII (3.2a):

$$\sigma_{\alpha s,\alpha' s'} = \frac{\pi}{k_\alpha^2(2s+1)} \sum_{Jll'} (2J+1)|T^J_{\alpha' s' l',\alpha s l}|^2, \tag{A.17}$$

where T is defined below (2.3) in the same chapter,

$$T_{\alpha' s' l',\alpha s l} = e^{2i\omega_{\alpha' l'}}\delta_{\alpha' s' l',\alpha s l} - U^J_{\alpha' s' l',\alpha s l}. \tag{A.18}$$

To simplify the notation in the following, c denotes the channel $\alpha s l$ and superscript, J, is omitted. The essential part of the cross section is then:

$$\sigma_{cc'} \propto |e^{2i\omega_{c'}}\delta_{c'c} - U_{c'c}|^2. \tag{A.19}$$

The second form of $\mathbf{W}$ is used in the collision matrix, denoting the second term of $\mathbf{W}$ by $\mathfrak{W}$. Inserting this into the above,

$$\sigma_{cc'} \propto |e^{2i\omega_{c'}}\delta_{c'c} - \Omega_{c'}(\delta_{c'c} + \mathfrak{W}_{c'c})\Omega_c|^2 = |e^{2i\omega_{c'}}\delta_{c'c} - \Omega_{c'}\Omega_c\delta_{c'c} + \Omega_{c'}\Omega_c\mathfrak{W}_{c'c}|^2. \tag{A.20}$$

First, the cross section for $c \neq c'$ is considered:

$$\begin{aligned}\sigma_{cc'}(c \neq c') &\propto |\Omega_{c'}\Omega_c\mathfrak{W}_{c'c}|^2 = |\mathfrak{W}_{c'c}|^2 \\ &= |[\mathfrak{P}^{1/2}(\mathbf{1} - \mathbf{RL}^0)^{-1}\mathbf{R}\mathfrak{P}^{1/2}\mathbf{w}]_{c'c}|^2 \\ &= 4P_cP_{c'}|\sum_{c''}(\mathbf{1} - \mathbf{RL}^0)^{-1}_{c'c''}R_{c''c}|^2.\end{aligned} \tag{A.21}$$

The equivalent level-matrix form is

$$\sigma_{cc'}(c \neq c') \propto 4P_cP_{c'}|\sum_{\lambda\lambda'}\gamma_{\lambda c}\gamma_{\lambda' c'}A_{\lambda\lambda'}|^2. \tag{A.22}$$

For $c = c'$ the cross section is:

$$\begin{aligned}
\sigma_{cc} \propto & |e^{2i\omega_c} - \Omega_c^2 + \Omega_c^2 \mathfrak{W}_{cc}|^2 \\
= & |1 - e^{-2i\phi_c} + e^{-2i\phi_c} \mathfrak{W}_{cc}|^2 \\
= & (1 - e^{-2i\phi_c} + e^{-2i\phi_c} \mathfrak{W}_{cc})(1 - e^{2i\phi_c} + e^{2i\phi_c} \mathfrak{W}^*_{cc}) \\
= & 1 - e^{2i\phi_c} + e^{2i\phi_c} \mathfrak{W}^*_{cc} - e^{-2i\phi_c} + 1 - \mathfrak{W}^*_{cc} + e^{-2i\phi_c} \mathfrak{W}_{cc} - \mathfrak{W}_{cc} + |\mathfrak{W}_{cc}|^2 \\
= & 2 - e^{2i\phi_c} - e^{-2i\phi_c} + (e^{-2i\phi_c} - 1)\mathfrak{W}_{cc} + (e^{2i\phi_c} - 1)\mathfrak{W}^*_{cc} + |\mathfrak{W}_{cc}|^2 \\
= & 2(1 - \cos 2\phi_c) \\
& + 2i(e^{-2i\phi_c} - 1) P_c \sum_{c'} (\mathbf{1} - \mathbf{R}\mathbf{L}^0)^{-1}_{cc'} R_{c'c} \\
& - 2i(e^{2i\phi_c} - 1) P_c \sum_{c'} (\mathbf{1} - \mathbf{R}\mathfrak{L}^0)^{-1}_{cc'} R_{c'c} \\
& + 4P_c^2 |\sum_{c'} (\mathbf{1} - \mathbf{R}\mathbf{L}^0)^{-1}_{cc'} R_{c'c}|^2 .
\end{aligned} \tag{A.23}$$

This can be rewritten to

$$\begin{aligned}
\sigma_{cc} \propto & 4 \sin^2 \phi_c \\
& + 4P_c \left[\sin 2\phi_c \mathrm{Re} \left(\sum_{c'} \mathbf{1} - \mathbf{R}\mathbf{L}^0)^{-1}_{cc'} R_{c'c} \right) \right. \\
& \left. + \ (1 - \cos 2\phi_c) \mathrm{Im} \left(\sum_{c'} \mathbf{1} - \mathbf{R}\mathbf{L}^0)^{-1}_{cc'} R_{c'c} \right) \right] \\
& + 4P_c^2 |\sum_{c'} (\mathbf{1} - \mathbf{R}\mathbf{L}^0)^{-1}_{cc'} R_{c'c}|^2 .
\end{aligned} \tag{A.24}$$

The equivalent level-matrix form is

$$\begin{aligned}
\sigma_{cc} \propto & 4 \sin^2 \phi_c \\
& + 4P_c \left[\sin 2\phi_c \mathrm{Re} \left(\sum_{\lambda\lambda'} \gamma_{\lambda c} \gamma_{\lambda' c} A_{\lambda\lambda'} \right) \right. \\
& \left. + \ (1 - \cos 2\phi_c) \mathrm{Im} \left(\sum_{\lambda\lambda'} \gamma_{\lambda c} \gamma_{\lambda' c} A_{\lambda\lambda'} \right) \right] \\
& + 4P_c^2 |\sum_{\lambda\lambda'} \gamma_{\lambda c} \gamma_{\lambda' c} A_{\lambda\lambda'}|^2 .
\end{aligned} \tag{A.25}$$

For the single level case, this expression is equivalent to (1.14) in section XII of [106].

A.2.1 Single channel approximation

In the case of only one channel, the matrices in the cross section formula have only one element, and the following can be used:

$$\sum_{c''}(\mathbf{1}-\mathbf{RL}^0)^{-1}_{cc''}R_{c''c'}=\frac{\sum_\lambda \gamma_{\lambda c}\gamma_{\lambda c'}/(E_\lambda-E)}{1-(S_c-B_c+iP_c)\sum_\lambda \gamma^2_{\lambda c}/(E_\lambda-E)}. \tag{A.26}$$

A.2.2 Single level approximation

In the case of a single level, λ, the level-matrix cross sections can be simplified by substituting

$$\sum_{\lambda\lambda'}\gamma_{\lambda c}\gamma_{\lambda' c'}A_{\lambda\lambda'}=\frac{\gamma_{\lambda c}\gamma_{\lambda c'}}{E_\lambda-E-\sum_c \gamma^2_{\lambda c}(S_c-B_c+iP_c)}. \tag{A.27}$$

For only one channel and one level the channel-matrix and level-matrix expressions yield the same result:

$$\mathfrak{W}_{cc'}=2iP_c^{1/2}P_{c'}^{1/2}\frac{\gamma_{\lambda c}\gamma_{\lambda c'}}{E_\lambda-E-\gamma^2_{\lambda c}(S_c-B_c+iP_c)}. \tag{A.28}$$

The total resonant cross section for incident channel, c', in the single level approximation is

$$\sigma_{c'}\propto\frac{4P_cP_{c'}\gamma^2_{\lambda c'}\sum_c\gamma^2_{\lambda c}}{|E_\lambda-E-\sum_c\gamma^2_{\lambda c}(S_c-B_c+iP_c)|^2}. \tag{A.29}$$

Substituting $\Gamma_\lambda=\sum_c\Gamma_{\lambda c}=\sum_c 2P_c\gamma^2_{\lambda c}$ and $\Delta=-\sum_c\gamma^2_{\lambda c}(S_c-B_c)$.

$$\sigma_{c'}\propto\frac{\Gamma_{\lambda c'}\Gamma_\lambda}{|E_\lambda-E-\Delta-i\Gamma_\lambda/2|^2}=\frac{\Gamma_{\lambda c'}\Gamma_\lambda}{(E_\lambda-E+\Delta)^2+\Gamma^2_\lambda/4} \tag{A.30}$$

Δ is energy dependent through $S_c(E)$, and can be approximated by a Taylor expansion to first order, if $S_c(E)$ is linear over the resonance energy range.

$$\Delta(E)\approx\Delta(E_\lambda)+(E-E_\lambda)\left.\frac{\delta\Delta}{\delta E}\right|_{E=E_\lambda}=\Delta(E_\lambda)+(E_\lambda-E)\sum_c\gamma^2_{\lambda c}\left.\frac{\delta S_c}{\delta E}\right|_{E=E_\lambda} \tag{A.31}$$

Inserting this:

$$\begin{aligned}\sigma_{c'}&\propto\frac{\Gamma_{\lambda c'}\Gamma_\lambda}{((E_\lambda-E)(1+\sum_c\gamma^2_{\lambda c}\left.\frac{\delta S_c}{\delta E}\right|_{E=E_\lambda})+\Delta(E_\lambda))^2+\Gamma^2_\lambda/4}\\&=\frac{\Gamma^o_{\lambda c'}\Gamma^o_\lambda}{(E_\lambda-E+\Delta')^2+(\Gamma^o_\lambda)^2/4}\end{aligned} \tag{A.32}$$

This is the Breit-Wigner formula for a single resonance, where

$$E_r = E_\lambda + \Delta' = E_\lambda - \frac{\sum_c \gamma_{\lambda c}^2 (S_c(E_\lambda) - B_c)}{1 + \sum_c \gamma_{\lambda c}^2 \left.\frac{\delta S_c}{\delta E}\right|_{E=E_\lambda}} \tag{A.33}$$

is the resonance energy. For $B_c = S_c(E_\lambda)$, the R-matrix parameter E_λ is equal to the resonance energy. The observed width of the state is

$$\Gamma_\lambda^o = \frac{\sum_c 2P_c\gamma_{\lambda c}^2}{1 + \sum_c \gamma_{\lambda c}^2 \left.\frac{\delta S_c}{\delta E}\right|_{E=E_\lambda}}. \tag{A.34}$$

A.3 β decay

The formalism for scattering can be applied to β decay in a way analogous to the inclusion of photon channels in [106] (XIII 3). The level-matrix form of the collision matrix can be written as

$$U_{cc'}(c \neq c') = i\Omega_c\Omega_{c'} \sum_{\lambda\lambda'} A_{\lambda\lambda'}\Gamma_{\lambda c}^{1/2}\Gamma_{\lambda' c'}^{1/2}, \tag{A.35}$$

where $\Gamma_{\lambda c} = 2P_c\gamma_{\lambda c}^2$. According to [106] the collision matrix element for incoming channel, e, and outgoing photon channel, p, is

$$U_{cc'} = i\Omega_e\Omega_p \sum_{\lambda\lambda'} A_{\lambda\lambda'}\Gamma_{\lambda e}^{1/2}\Gamma_{\lambda' p}^{1/2}, \tag{A.36}$$

where Ω_p is the photon phase factor and $\Gamma_{\lambda p}$ the width amplitude. For β decay the corresponding substitution is

$$(\Omega_c\Gamma_{\lambda c}^{1/2})^2 = f_\beta g_{\lambda x}^2, \tag{A.37}$$

where $g_{\lambda x}$ is the β-strength parameter with $x = F$ or G corresponding to Fermi and Gamow-Teller transitions, and $f_\beta(Q - E)$ is the integrated Fermi function ([144] App. III)(see A.5.1). The cross section is thus replaced by a decay probability:

$$w_c(E) = C^2 f_\beta P_c \sum_{\mathrm{x=F,GT}} |\sum_{\lambda\lambda'} g_{\lambda x}\gamma_{\lambda' c}A_{\lambda\lambda'}|^2, \tag{A.38}$$

$$w(E) = \sum_c w_c(E), \tag{A.39}$$

where C^2 is a normalization constant chosen to satisfy

$$w = \int w(E)dE = \frac{\ln 2}{t_{1/2}} \tag{A.40}$$

From this equality the normalization constant is found:

$$C = \sqrt{\frac{\ln 2}{B\pi}}, \tag{A.41}$$

where $B = 6146(6)$ [110].

When the R-matrix formalism is needed to fit a part of a decay energy spectrum containing N number events and the half life to the energy region where the fit is performed is $t_{1/2}$, the following formula is used:

$$N_c(E) = C^2 \frac{N t_{1/2}}{\ln 2} f_\beta P_c \sum_{\mathrm{x=F,GT}} |\sum_{\lambda\lambda'} g_{\lambda x}\gamma_{\lambda' c} A_{\lambda\lambda'}|^2. \tag{A.42}$$

In this definition we used

$$N = \int N(E)dE, \tag{A.43}$$

where

$$N(E) = \frac{N t_{1/2}}{\ln 2} w(E) = \sum_c N_c(E). \tag{A.44}$$

The single level and single channel approximations are similar to the expressions for scattering. For a single channel:

$$w(E) = C^2 f_\beta P_c \sum_{\mathrm{x=F,GT}} \left| \frac{\sum_\lambda g_{\lambda x}\gamma_{\lambda c}/(E_\lambda - E)}{1 - (S_c - B_c + iP_c)\sum_\lambda \gamma^2_{\lambda c}/(E_\lambda - E)} \right|^2, \tag{A.45}$$

and for a single level:

$$w(E) = C^2 f_\beta \sum_{\mathrm{x=F,GT}} |g_{\lambda x}|^2 \frac{\sum_c P_c \gamma^2_{\lambda c}}{|E_\lambda - E - \sum_c \gamma^2_{\lambda c}(S_c - B_c + iP_c)|^2}. \tag{A.46}$$

A.3.1 β-decay matrix elements

The analogy to photon channels can also be used to derive expressions for the β-decay matrix elements, M_F and M_{GT}, for Fermi and Gamow-Teller transitions respectively. The following definition applies to photons

$$\Omega_p \Gamma^{1/2}_{\lambda p} = \left\{ (2\pi\rho)^{1/2} \int \psi_p^{(1)*} H' X_\lambda \right\}_{E_p = E}, \tag{A.47}$$

where H' is the photon creation operator and the integral is over the interaction volume. A similar expression is valid for β decay with H' replaced by the Fermi

or Gamow-Teller transition operator and $2\pi\rho$ replaced by f_β. The integral is proportional to the matrix element, but with a correction factor due to the fact that the wave functions are normalized to the internal region. According to [106] p. 352 any physical quantity depending upon the square of the wave function that is normalized in the internal region should be modified by the correction factor, $[1-(d\Delta/dE)]^{-1}$, with $\Delta = -\sum_c \gamma_{\lambda c}^2(S_c - B_c)$ evaluated in the resonance energy, to get the value corresponding to a "renormalized" wave function. The correction factor is a Taylor expansion to first order of the first term of the denominator in the single level approximation. This is only valid if the shift function is a linear funcion over the energy range of the level. For most cases this is a very reasonable assumption. The matrix element, calculated from R-matrix parameters, is therefore:

$$M_{\lambda x} = \frac{|g_{\lambda x}|}{\sqrt{1+\sum_c \gamma_{\lambda c}^2 (dS_c/dE)|_{E=E_\lambda}}}, \tag{A.48}$$

with $x = F$ or GT.

A.4 Alternative parametrization without boundary conditions

An alternative set of R-matrix parameters can be found, where the energies, $\tilde{E}_i$, reduced widths, $\tilde{\gamma}_{ic}^2$ and β strengths, $\tilde{g}_{ix}$ are the "observed" resonance parameters (equal to the standard R-matrix parameters for which $B_c = S_c(E_\lambda)$). The derivation will follow [107] and lead to an alternative formula for the level matrix.

First, the real and symmetric matrix $\mathcal{E}$ is defined:

$$\mathcal{E} = \mathbf{e} - \sum_c \gamma_c \gamma_c^T (S_c - B_c), \tag{A.49}$$

where $\mathbf{e}$ is a diagonal $N_\lambda \times N_\lambda$ matrix with $e_{\lambda\mu} = E_\lambda \delta_{\lambda\mu}$ and γ_c is the column-vector with entries $\gamma_{\lambda c}$. The eigenvalue equation for $\mathcal{E}$ is

$$\mathcal{E}\mathbf{a}_i = \tilde{E}_i \mathbf{a}_i. \tag{A.50}$$

The eigenvectors are normalized so that $\mathbf{a}_i^T \mathbf{a}_i = 1$. Note that for the single level case, $\mathcal{E}$ has only one entry, $\mathcal{E}_\lambda = E_\lambda - \sum_c \gamma_{\lambda c}^2 (S_c - B_c)$, which is the "observed" resonance energy. Generally, the eigenvalues, $\tilde{E}_i$, are invariant if the boundary conditions are changed, and if $B_c = S_c(E_\lambda)$, E_λ is an eigenvalue. The eigenvalues, $\tilde{E}_i$, therefore correspond to "observed" resonance energies. The corresponding reduced width amplitudes

$$\tilde{\gamma}_{ic} = \mathbf{a}_i^T \gamma_c \tag{A.51}$$

are also invariant under changes in B_c, and for $B_c = S_c(E_\lambda)$, $\tilde{\gamma}_{\lambda c} = \gamma_{\lambda c}$.

The collision matrix must be invariant when changing to alternative parameters, requiring:

$$\sum_{\lambda\lambda'} \gamma_{\lambda c}\gamma_{\lambda' c'} A_{\lambda\lambda'} = \gamma_c^T \mathbf{A}\gamma_{c'} = \tilde{\gamma}_c^T \tilde{\mathbf{A}}\tilde{\gamma}_{c'}. \tag{A.52}$$

Using the definition, $\tilde{\gamma}_c = \mathbf{a}^T\gamma_c$,

$$\mathbf{A} = \mathbf{a}\tilde{\mathbf{A}}\mathbf{a}^T \Leftrightarrow \tilde{\mathbf{A}} = \mathbf{a}^T\mathbf{A}^{-1}\mathbf{a}. \tag{A.53}$$

Inserting the matrix expression for $\mathbf{A}^{-1}$ this becomes,

$$\tilde{\mathbf{A}}^{-1} = \mathbf{a}^T\mathbf{e}\mathbf{a} - E\mathbf{a}^T\mathbf{a} - \sum_c \tilde{\gamma}_c\tilde{\gamma}_c^T(S_c - B_c + iP_c). \tag{A.54}$$

The matrices, $\mathbf{a}^T\mathbf{e}\mathbf{a}$ and $\mathbf{a}^T\mathbf{a}$, are derived in [107] by rewriting the eigenvalue equation (A.50). Inserting the results one obtains:

$$(\tilde{\mathbf{A}}^{-1})_{ij} = (\tilde{E}_i - E)\delta_{ij} - \sum_c \tilde{\gamma}_{ic}\tilde{\gamma}_{jc}(S_c + iP_c) \tag{A.55}$$
$$+ \sum_c \begin{cases} \tilde{\gamma}_{ic}^2 S_{ic}, & i = j \\ \tilde{\gamma}_{ic}\tilde{\gamma}_{jc}\frac{S_{ic}(E-\tilde{E}_j) - S_{jc}(E-\tilde{E}_i)}{\tilde{E}_i - \tilde{E}_j}, & i \neq j \end{cases}$$

In this formula S_{ic} denotes the shift function S_c evaluated at $\tilde{E}_i$.

A.5 Application in the β decay of ^{11}Be

In this work the R-matrix framework for β decay is applied in the analysis of the charged-particle emission in the β decay of ^{11}Be, see Chapter 4. The energy spectrum of the emitted ^{7}Li and α particles is fit with formula (A.42) using the alternative parametrization presented in A.4:

$$N_c(E) = C^2\frac{Nt_{1/2}}{\ln 2} f_\beta P_c \sum_{\mathrm{x=F,GT}} |\sum_{\lambda\lambda'} \tilde{g}_{\lambda x}\tilde{\gamma}_{\lambda' c}\tilde{A}_{\lambda\lambda'}|^2 \tag{A.56}$$

$$(\tilde{\mathbf{A}}^{-1})_{\lambda\lambda'} = (\tilde{E}_\lambda - E)\delta_{\lambda\lambda'} - \sum_c \tilde{\gamma}_{\lambda c}\tilde{\gamma}_{\lambda' c}(S_c + iP_c) \tag{A.57}$$
$$+ \sum_c \begin{cases} \tilde{\gamma}_{\lambda c}^2 S_{\lambda c}, & \lambda = \lambda' \\ \tilde{\gamma}_{\lambda c}\tilde{\gamma}_{\lambda' c}\frac{S_{\lambda c}(E-\tilde{E}_{\lambda'}) - S_{\lambda' c}(E-\tilde{E}_\lambda)}{\tilde{E}_\lambda - \tilde{E}_{\lambda'}}, & \lambda \neq \lambda' \end{cases}$$

The energies, $\tilde{E}_\lambda$, reduced widths, $\tilde{\gamma}_{\lambda c}^2$ and β strengths, $\tilde{g}_{\lambda x}$, are the free parameters in the fitting procedure. The advantage of this approach is that these

fit parameters are the physical observables. The observed widths, Γ_λ, of the states are (according to (A.34)) found by

$$\begin{aligned}\Gamma_\lambda &= \sum_c \Gamma_{\lambda c} \\ &= \frac{\sum_c 2P_c\tilde{\gamma}_{\lambda c}^2}{1+\sum_c \tilde{\gamma}_{\lambda c}^2 \left.\frac{\delta S_c}{\delta E}\right|_{E=\tilde{E}_\lambda}}. \end{aligned} \tag{A.58}$$

The fit results for the reduced widths, $\tilde{\gamma}_{\lambda c}^2$, can be compared to the Wigner (W) limit:

$$\begin{aligned}\tilde{\gamma}_{\lambda c,W}^2 &= \frac{\hbar^2}{\mu a_c^2} && \text{(A.59)} \\ &= 0.668 \text{ MeV}, \\ (\tilde{\gamma}_{\lambda c,W} &= 0.817 \text{ MeV}^{1/2}) && \text{(A.60)}\end{aligned}$$

where μ is the reduced mass and a_c the channel radius (see section A.5.2). This limit corresponds to a maximum overlap between the internal wave function (^{11}B state in this case) and the breakup channel (here ^{7}Li+α), i.e. maximum coupling to this channel.

A.5.1 Phase space

The phase space factor, $f_\beta(Q-E)$, that is implemented in the R-matrix formalism is calculated using the parametrization for allowed β decay presented in [60]:

$$f = Sf_{Z=0} \tag{A.61}$$

$$f_{Z=0} = \frac{1}{60}(2W_0^4 - 9W_0^2 - 8)p_0 + \frac{1}{4}W_0 \ln(W_0 + p_0) \tag{A.62}$$

$$\ln S = a_0 + a_1 \ln E_0 + a_2(\ln E_0)^2 + a_3(\ln E_0)^3, \tag{A.63}$$

where E_0 is the electron kinetic energy end point, $Q_\beta - E$, in keV, W_0 is the total electron energy end point in units m_e , $(E_0 + m_e)/m_e$, and $p_0 = (W_0^2$ - $1)^{1/2}$. The coefficients a_i are tabulated in [60] as function of the atomic number, Z, of the daughter nucleus and E_0.

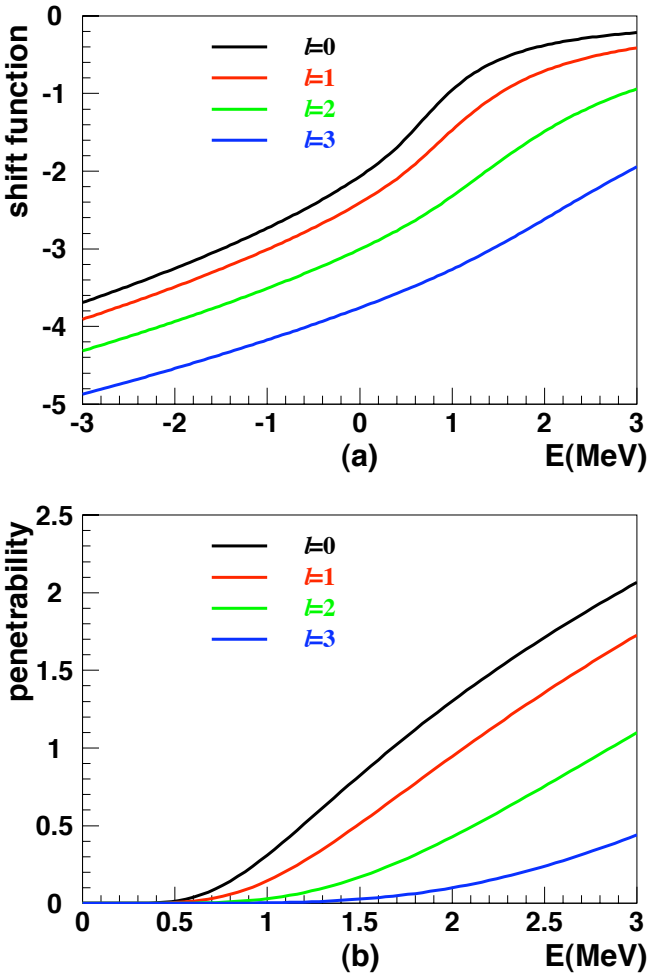

Figure A.1: (a) The shift function, calculated from A.64, is shown for different relative orbital momenta l for the ^{7}Li+α channel in the β decay of ^{11}Be as a function of their summed energy. (b) For the same emission channel as in (a) the penetrabilities are shown according to A.65

A.5.2 Shift function and penetrability

The shift function and penetrability are calculated as [106]:

$$S_c(\eta,\rho) = \begin{cases} \left[\rho\left(\frac{F_cF_c'+G_cG_c'}{|F_c^2|+|G_c^2|}\right)\right]_{r_c=a_c} & E>0 \\ \left[\rho\left(\frac{W_c'}{W_c}\right)\right]_{r_c=a_c} = \mathrm{Re}\left[i\rho_c\frac{(H_c^+)'}{(H_c^+)}\right]_{r_c=a_c} & E<0 \end{cases} \tag{A.64}$$

$$P_c(\eta,\rho) = \begin{cases} \left[\left(\frac{\rho}{|F_c^2|+|G_c^2|}\right)\right]_{r_c=a_c} & E>0 \\ 0 & E\leq 0 \end{cases} \tag{A.65}$$

η (Coulomb field parameter) and ρ (penetration factor) are defined as [106]:

$$\eta = \alpha Z_1 Z_2 \sqrt{\frac{\mu c^2}{2|E|}} \tag{A.66}$$

$$\rho = \sqrt{\frac{2\mu|E|}{\hbar^2}}a_c. \tag{A.67}$$

The Coulomb functions, $F_c(\eta_c,\rho_c)$ and $G_c(\eta_c,\rho_c)$, are positive energy solutions to the radial Schrödinger equation for the Coulomb interaction. For $E<0$ the negative energy solutions are used to calculate the shift function. One can choose to use either the real Whittaker function, W_c, as in [106], or the complex Hankel function, $H_c^+(i\rho_c) = G_c^+(i\rho_c) + iF_c^+(i\rho_c)$, (see [145] p. 366). The ratio $(H_c^+)'/H_c^+$ becomes imaginary because of the complex argument: $dH_c^+/d\rho_c = idH_c^+/d(i\rho_c) = i(H_c^+)'$. α is the fine structure constant, μ is the reduced mass, and a_c the channel radius $a_c = r_0(A_1^{1/3}+A_2^{1/3})$. In the analysis of the ^{11}Be β-delayed charged-particle emission r_0 was chosen to be 1.42fm. This results in a typical value for the channel radius $a_c = 4.96$fm ($A_1 = 4$ (α) and $A_2 = 7$ (^{7}Li)). The shift functions and penetrabilities for the ^{7}Li+α emission channel are shown in Figure A.1 for different relative orbital momenta l as a function of the summed ^{7}Li and α energies. In Chapter 4 it is shown that in the physics case of interest, only positive parity states in ^{11}B have to be taken into the fitting process. This limits the possibilities to only odd values for l. It can be seen from Figure A.1(b) that the penetrability for the $l=3$ emission channel is smaller than the one for $l=1$. In the region around the state at 9.876 MeV, which is shown in Chapter 4 to be responsible for the main contribution in the charged-particle energy spectrum, the penetrability for the $l=1$ emission channel is a factor 30 higher than the one for $l=3$. Therefore only $l=1$ contributions were taken into calculation as a good first approximation.

The Coulomb functions and complex Hankel functions are implemented in the CERNLIB program WCLBES [145] that can be invoked by the fitting program written in the programming language FORTRAN.

Bibliography

[1] B. Jonson. *Phys. Rep.* **389**, 1 (2004).

[2] H. Geissel, G. Münzenberg, and K. Riisager. *Annu. Rev. Nucl. Part. Sci.* **45**, 163 (1995).

[3] P. Van Duppen et al. *Nucl. Instrum. Methods B* **70**, 393 (1992).

[4] M. V. Zhukov, B. V. Danilin, D. V. Fedorov, J. M. Bang, I. J. Thompson, and J. S. Vaagen. *Phys. Rep.* **231**, 151 (1993).

[5] A. S. Jensen and M. V. Zhukov. *Nucl. Phys. A* **693**, 411 (2001).

[6] K. Riisager, A. S. Jensen, and P. Møller. *Nucl. Phys. A* **548**, 393 (1992).

[7] D. V. Fedorov, A. S. Jensen, and K. Riisager. *Phys. Lett. B* **312**, 1 (1993).

[8] D. V. Fedorov, A. S. Jensen, and K. Riisager. *Phys. Rev. C* **50**, 2372 (1994).

[9] I. Tanihata et al. *Phys. Lett. B* **160**, 380 (1985).

[10] I. Tanihata et al. *Phys. Rev. Lett.* **55**, 2676 (1985).

[11] A. Ozawa et al. *Nucl. Phys. A* **691**, 599 (2001).

[12] S. R. Neumaier et al. *Nucl. Phys. A* **712**, 247 (2002).

[13] P. Müller et al. *Phys. Rev. Lett.* **99**, 252501 (2007).

[14] R. Sánchez et al. *Phys. Rev. Lett.* **96**, 033002 (2006).

[15] W. Nörthershäuser et al. *Phys. Rev. Lett.* **102**, 062503 (2009).

[16] D. J. Millener, J. W. Olness, E. K. Warburton, and S. Hanna. *Phys. Rev. C* **28**, 497 (1983).

[17] S. Fortier et al. *Phys. Lett. B* **461**, 22 (1999).

[18] J. S. Winfield et al. *Nucl. Phys. A* **683**, 48 (2001).

[19] T. Aumann et al. *Phys. Rev. Lett.* **84**, 35 (2000).

[20] W. Geithner et al. *Phys. Rev. Lett.* **83**, 3792 (1999).

[21] D. Bazin et al. *Phys. Rev. C* **57**, 2156 (1998).

[22] D. Cortina-Gil et al. *Eur. Phys. J. A* **10**, 49 (2001).

[23] E. Sauvan et al. *Phys. Lett. B* **491**, 1 (2000).

[24] H. Simon et al. *Phys. Rev. Lett.* **83**, 496 (1999).

[25] I. J. Thompson and M. V. Zhukov. *Phys. Rev. C* **47**, 1904 (1994).

[26] T. Kobayashi, O. Yamakawa, K. Omata, K. Sugimoto, T. Shimoda, N. Takahashi, and I. Tanihata. *Phys. Rev. Lett.* **60**, 2599 (1988).

[27] N. A. Orr et al. *Phys. Rev. Lett.* **69**, 2050 (1992).

[28] I. Tanihata, T. Kobayashi, O. Yamakawa, S. Shimoura, K. Ekuni, K. Sugimoto, N. Takahashi, and T. Shimoda. *Phys. Lett. B* **206**, 592 (1988).

[29] J. Al-Khalili and J. A. Tostevin. *Phys. Rev. C* **54**, 1843 (1996).

[30] R. E. Azuma et al. *Phys. Lett. B* **96**, 31 (1980).

[31] B. Jonson and K. Riisager. *Nucl. Phys. A* **693**, 77 (2001).

[32] T. Nilsson, G. Nyman, and K. Riisager. *Hyperfine Interactions* **129**, 67 (2000).

[33] R. Ringle et al. *Phys. Lett. B* **675**, 170 (2009).

[34] M. Smith et al. *Phys. Rev. Lett.* **101**, 202501 (2008).

[35] E. Roeckl et al. *Phys. Rev. C* **10**, 1181 (1974).

[36] R. E. Azuma et al. *Phys. Rev. Lett.* **43**, 1652 (1979).

[37] M. Langevin et al. *Nucl. Phys. A* **366**, 449 (1981).

[38] M. Langevin et al. *Phys. Lett. B* **146**, 176 (1984).

[39] I. Mukha et al. *Phys. Lett. B* **367**, 65 (1996).

[40] K. Riisager et al. *Phys. Lett. B* **235**, 30 (1990).

[41] M. J. G. Borge et al. *Nucl. Phys. A* **560**, 664 (1993).

[42] D. Anthony et al. *Phys. Rev. C* **65**, 034310 (2002).

[43] D. Smirnov et al. *Nucl. Instrum. Methods Phys. Res. A* **547**, 480 (2005).

[44] J. Büscher et al. *Nucl. Instrum. Methods Phys. Res. B* **266**, 4652 (2008).

[45] R. Raabe et al. *Phys. Rev. Lett.* **101**, 212501 (2008).

[46] R. D. Page et al. *Phys. Rev. C* **49**, 3312 (1994).

[47] E. S. Paul et al. *Phys. Rev. C* **51**, 78 (1995).

[48] P. J. Sellin et al. *Nucl. Instr. and Meth. A* **311**, 217 (1992).

[49] www.micronsemiconductor.co.uk.

[50] www.mesytec.com/datasheets/MPR16.pdf.

[51] www.mesytec.com/datasheets/STM 16.pdf.

[52] www.wnt.gsi.de/daq.

[53] http://npsg.dl.ac.uk/MIDAS/.

[54] http://paw.web.cern.ch/paw/.

[55] W. R. Leo. *Techniques for Nuclear and Particle Physics Experiments*. Springer-Verlag, (1987).

[56] J. B. Marion and F. C. Young. *Nuclear Reaction Analysis - Graphs and Tables*. North-Holland Publishing Company - Amsterdam, (1968).

[57] A. T. Nelms. *Energy Loss and Range of Electrons and Positrons*. National Bureau of Standards Circular 577, (1956).

[58] S. Agostinelli et al. *Nucl. Instrum. Methods Phys. Res. A* **506**, 250 (2003).

[59] J. F. Ziegler, J. P. Biersack, and U. Littmark. *The Stopping and Range of Ions in Solids*. Pergamon Press, New York, (1985).

[60] D. H. Wilkinson and B. E. F. Macefield. *Nucl. Phys. A* **232**, 58 (1974).

[61] D. H. Wilkinson. *Nucl. Instrum. Methods Phys. Res. A* **275**, 378 (1989).

[62] D. H. Wilkinson. *Nucl. Instrum. Methods Phys. Res. A* **290**, 509 (1990).

[63] D. H. Wilkinson. *Nucl. Instrum. Methods Phys. Res. A* **365**, 497 (1995).

[64] P. Descouvemont and C. Leclercq-William. *J. Phys. G* **18**, L99 (1992).

[65] M. V. Zhukov, B. V. Danilin, L. V. Grigorenko, and N. B. Shul'gina. *Phys. Rev. C* **47**, 271 (1994).

[66] D. Baye, Y. Suzuki, and P. Descouvemont. *Prog. Theor. Phys.* **91**, 271 (1994).

[67] K. Varga, Y. Suzuki, and Y. Ohbayasi. *Phys. Rev. C* **50**, 189 (1994).

[68] A. Csótó and D. Baye. *Phys. Rev. C* **49**, 818 (1994).

[69] F. C. Barker. *Phys. Lett. B* **322**, 17 (1994).

[70] E. M. Tursunov, D. Baye, and P. Descouvemont. *Phys. Rev. C* **73**, 014303 (2006).

[71] Y. Ohbayasi and Y. Suzuki. *Phys. Lett. B* **346**, 223 (1995).

[72] M. V. Zhukov, B. V. Danilin, L. V. Grigorenko, and J. S. Vaagen. *Phys. Rev. C* **52**, 2461 (1995).

[73] D. Baye, E. M. Tursunov, and P. Descouvemont. *Phys. Rev. C* **74**, 064302 (2006).

[74] G. Ryckewaert, J. M. Colson, M. Gaelens, M. Loiselet, and N. Postiau. *Nucl. Phys. A* **701**, 323c (2005).

[75] D. H. Wilkinson and D. E. Alburger. *Phys. Rev.* **113**, 563 (1959).

[76] D. E. Alburger, C. Chasman, K. W. Jones, J. W. Olness, and R. A. Ristinen. *Phys. Rev.* **136**, B 916 (1964).

[77] J. P. Deutsch, L. Grenacs, J. Lehmann, P. Lipnik, and P. C. Macq. *Phys. Lett. B* **28**, 178 (1968).

[78] D. L. Auton. *Nucl. Phys. A* **157**, 305 (1970).

[79] I. Talmi and I. Unna. *Phys. Rev. Lett.* **4**, 469 (1960).

[80] Aa. Bohr and B. R. Mottelson. *Nuclear structure, vol II.* Benjamin, NY, (1975).

[81] M. J. Nurmia and R. W. Fink. *Phys. Rev. Lett.* **1**, 23 (1958).

[82] D. E. Alburger and G. A. P. Engelbertink. *Phys. Rev. C* **2**, 1594 (1970).

[83] G. Audi, A. H. Wapstra, and C. Thibault. *Nucl. Phys. A* **729**, 337 (2003).

[84] F. Ajzenberg-Selove. *Nucl. Phys. A* **506**, 1 (1990).

[85] D. E. Alburger and D. H. Wilkinson. *Phys. Rev. C* **3**, 1492 (1971).

[86] R. Y. Cusson. *Nucl. Phys.* **86**, 481 (1966).

[87] P. Paul, N. G. Puttaswamy, and D. Kohler. *Phys. Rev.* **164**, 1332 (1967).

[88] D. E. Alburger, D. J. Millener, and D. H. Wilkinson. *Phys. Rev. C* **23**, 473 (1981).

[89] D. J. Millener, D. E. Alburger, E. K. Warburton, and D. H. Wilkinson. *Phys. Rev. C* **26**, 1167 (1982).

[90] P. Bricault et al. *Proceedings of the 1995 Particle Accelerator Conference (IEEE Conference Proceedings, Dallas, TX, USA, 1995)*, p. 348.

[91] J. M. D'Auria, J. Thomson, M. Comyn, and in others. *Proceedings of the 14th International Conference on Electromagnetic Isotope Separators and Techniques Related to their Applications* , vol 204 (Nucl. Instrum. Methods Phys. Res. B, vol. 204, 2003).

[92] I. Mukha et al. *Nucl. Phys. A* **616**, 201c (1997).

[93] M. J. G. Borge et al. *Phys. Rev. C* **55**, R8 (1997).

[94] C. Détraz et al. *Le Journal de Physique - Lettres* **41**, 459 (1980).

[95] T. Björnstad et al. *Nucl. Phys. A* **359**, 1 (1981).

[96] D. J. Morrissey et al. *Nucl. Phys. A* **627**, 222 (1997).

[97] N. Aoi et al. *Nucl. Phys. A* **616**, 181c (1997).

[98] D. R. Tilley et al. *Nucl. Phys. A* **708**, 3 (2002).

[99] R. Raabe et al. *Phys. Rev. C* **80**, 054307 (2009).

[100] F. Sarazin et al. *Phys. Rev. C.* **70**, 031302(R) (2004).

[101] C. M. Mattoon et al. *Phys. Rev. C.* **80**, 034318 (2009).

[102] H. O. U. Fynbo et al. *Nucl. Phys. A* **736**, 39 (2004).

[103] H. O. U. Fynbo et al. *Nucl. Instrum. Methods Phys. Res. B* **207**, 275 (2003).

[104] F. Sarazin. Private communication.

[105] H. O. U. Fynbo. Private communication.

[106] A. M. Lane and R. G. Thomas. *Rev. Mod. Phys. 30* **30**, 257 (1958).

[107] C. R. Brune. *Phys. Rev. C* **66**, 044611 (2002).

[108] F. C. Barker and E. K. Warburton. *Nucl. Phys. A* **487**, 269 (1988).

[109] K. Heyde. *Basic Ideas And Concepts In Nuclear Physics, Third Edition : An Introductory Approach*. IoP Publishing, (2004).

[110] I. S. Towner and in J. C. Hardy. *The Nucleus as a Laboratory for Studying Symmetries and Fundamental Interactions* , edited by E. M. Henley and W. C. Haxton (World Scientific, Singapore, 1995).

[111] H. Abele et al. *Phys. Rev. Lett.* **88**, 211801 (2002).

[112] B. Zwieglinski et al. *Nucl. Phys. A* **389**, 301 (1982).

[113] V. N. Fedoseyev et al. *Hyp. Int.* **127**, 409 (2000).

[114] I. Tanihata et al. *Phys. Rev. Lett.* **100**, 192502 (2008).

[115] T. Suzuki and T. Otsuka. *Phys. Rev. C* **50**, R555 (1994).

[116] S. Cohen and D. Kurath. *Nucl. Phys* **73**, 1 (1965).

[117] N. Fukunishi T. Otsuka and H. Sagawa. *Phys. Rev. Lett.* **70**, 1385 (1993).

[118] D. J. Millener and D. Kurath. *Nucl. Phys. A* **255**, 315 (1975).

[119] B.A. Brown, A. Etchegoyen, and W. D. M. Rae. *OXBASH, The Oxford, Buenos Aires Michigan State Shell Model Program, MSU Cyclotron Laboratory Report No. 524, 1986* .

[120] T. Suzuki and T. Otsuka. *Phys. Rev. C* **56**, 847 (1997).

[121] M. J. G. Borge et al. *Nucl. Phys. A* **613**, 199 (1997).

[122] E. Arnold et al. *Phys. Lett. B* **281**, 16 (1992).

[123] C. W. Li and R. Sherr. *Phys. Rev.* **96**, 389 (1954).

[124] H. Bichsel and T. W. Bonner. *Phys. Rev.* **108**, 1025 (1957).

[125] J. P. Stoquert, N. Bendjaballah, H. Beaumevieille, C. Gérardin, and R. Seltz. *Le Journal de Physique* **40**, 813 (1979).

[126] D. E. Groce, J. H. McNally, and W. Whaling. *Bull. Am. Phys. Soc.* **8**, 486 (1963).

[127] S. Ahmed et al. *Phys. Rev. C* **69**, 024303 (2004).

[128] R. O. Lane, S. L. Hausladen, J. E. Monahan, A. J. Elwyn, F. P. Mooring, and A. Langsdorf Jr. *Phys. Rev. C* **4**, 380 (1971).

[129] S. L. Hausladen, C. E. Nelson, and R. O. Lane. *Nucl. Phys. A* **217**, 563 (1973).

[130] W. D. Teeters and D. Kurath. *Nucl. Phys. A* **275**, 61 (1977).

[131] T. T. S. Kuo. *Nucl. Phys. A* **103**, 71 (1967).

[132] T. Yamada. Private communication.

[133] W. von Oertzen. *Z. Phys. A* **357**, 355 (1997).

[134] M. Freer. *C. R. Physique* **4**, 475 (2003).

[135] N. I. Ashwood et al. *Phys. Lett. B* **580**, 129 (2004).

[136] N. Soić et al. *Nucl. Phys. A* **728**, 12 (2003).

[137] N. Soić et al. *Phys. Rev. C* **68**, 014321 (2003).

[138] M. Milin and W. von Oertzen. *Eur. Phys. J. A* **14**, 295 (2002).

[139] M. Madurga et al. *Nucl. Phys. A* **810**, 1 (2008).

[140] S. Shimoura et al. *Nucl. Phys. A* **616**, 208c (1997).

[141] S. Hyldegaard et al. *Int. Journal of Mod. Phys. E* **17**, 2182 (2008).

[142] S. Hyldegaard et al. *Phys. Lett. B* **678**, 459 (2009).

[143] S. Hyldegaard et al. *Phys. Rev. C* **81**, 024303 (2010).

[144] F. C. Barker. *Austr. J. Phys.* **22**, 239 (1969).

[145] I. J. Thompson and A. R. Barnett. *Comp. Phys. Comm.* **36**, 363 (1985).